



HAL
open science

Ultrasound image segmentation using local statistics with an adaptative scale selection

Qing Yang

► **To cite this version:**

Qing Yang. Ultrasound image segmentation using local statistics with an adaptative scale selection. Computer Science [cs]. Université de Technologie de Compiègne, 2013. English. NNT: 2013COMP2065 . tel-00869975

HAL Id: tel-00869975

<https://theses.hal.science/tel-00869975>

Submitted on 4 Oct 2013

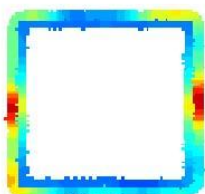
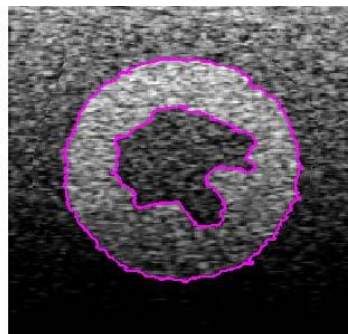
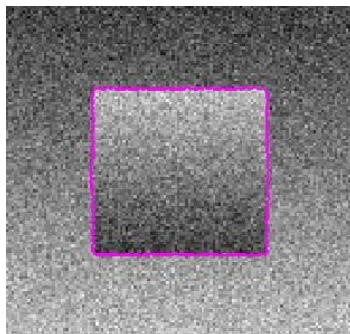
HAL is a multi-disciplinary open access archive for the deposit and dissemination of scientific research documents, whether they are published or not. The documents may come from teaching and research institutions in France or abroad, or from public or private research centers.

L'archive ouverte pluridisciplinaire **HAL**, est destinée au dépôt et à la diffusion de documents scientifiques de niveau recherche, publiés ou non, émanant des établissements d'enseignement et de recherche français ou étrangers, des laboratoires publics ou privés.

Par Qing YANG

Segmentation d'images ultrasonores basée sur des statistiques locales avec une sélection adaptative d'échelles

Thèse présentée
pour l'obtention du grade
de Docteur de l'UTC



Soutenue le 15 mars 2013

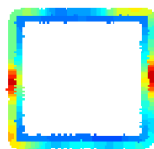
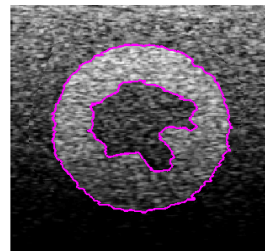
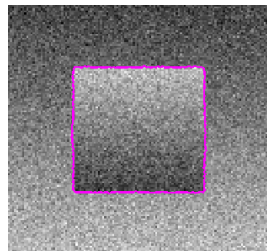
Spécialité : Technologies de l'Information et des Systèmes

D2065

par Qing Yang

***Segmentation d'images ultrasonores basée sur
des statistiques locales avec une sélection
adaptative d'échelles***

Thèse présentée
pour l'obtention du grade
de Docteur de l'UTC.



Soutenue le : 15 mars 2013
Spécialité Technologie de l'information et des
systèmes

Segmentation d'images ultrasonores basée sur des statistiques locales avec une sélection adaptative d'échelles

Thèse soutenue le 15 mars 2013 devant le jury composé :

| | | | |
|----|----------------|-------------------------|--------------------|
| M. | J.P. Cocquerez | Professeur d'Université | Président |
| M. | O. Basset | Professeur d'Université | Rapporteur |
| M. | J.M. Boucher | Professeur d'Université | Rapporteur |
| M. | A.O. Boudraa | Maître de conférences | Examineur |
| M. | V. Fremont | Maître de conférences | Examineur |
| M. | D. Boukerroui | Maître de conférences | Directeur de thèse |

À mes parents.

À Xiao.

Résumé

La segmentation d'images est un domaine important dans le traitement d'image et un grand nombre d'approches différentes ont été développées pendant ces dernières décennies. L'approche des contours actifs est une des plus populaires. Dans ce cadre, cette thèse vise à développer des algorithmes robustes, qui peuvent segmenter des images avec des inhomogénéités d'intensité. Nous nous concentrons sur l'étude des énergies externes basées région dans le cadre des ensembles de niveaux. Précisément, nous abordons la difficulté de choisir l'échelle de la fenêtre spatiale qui définit la localité.

Notre contribution principale est d'avoir proposer une échelle adaptative pour les méthodes de segmentation basées sur les statistiques locales. Nous utilisons l'approche d'Intersection des Intervalles de Confiance pour définir une échelle position-dépendante pour l'estimation des statistiques image. L'échelle est optimale dans le sens qu'elle donne le meilleur compromis entre le biais et la variance de l'Approximation polynomiale locale de l'image observée conditionnellement à la segmentation actuelle. De plus, pour le model de segmentation basé sur une interprétation Bayésienne avec deux noyaux locaux, nous suggérons de considérer leurs valeurs séparément. Notre proposition donne une segmentation plus lisse avec moins de délocalisations que la méthode originale.

Des expériences comparatives de notre proposition à d'autres méthodes de segmentation basées sur des statistiques locales sont effectuées. Les résultats quantitatifs réalisés sur des images ultrasonores de simulation, montrent que la méthode proposée est plus robuste au phénomène d'atténuation. Des expériences sur des images réelles montrent également l'utilité de notre approche.

Mots Clés : segmentation d'image, contours actifs, statistiques région locale, ensembles de niveaux, Intersection des Intervalles de Confiance, images ultrasonores

Abstract

Image segmentation is an important research area in image processing and a large number of different approaches have been developed over the last few decades. The active contour approach is one of the most popular among them. Within this framework, this thesis aims at developing robust algorithms, which can segment images with intensity inhomogeneities. We focus on the study of region-based external energies within the level set framework. We study the use of local image statistics for the design of external energies. Precisely, we address the difficulty of choosing the scale of the spatial window that defines locality.

Our main contribution is to propose an adaptive scale for local region-based segmentation methods. We use the Intersection of Confidence Intervals approach to define this pixel-dependent scale for the estimation of local image statistics. The scale is optimal in the sense that it gives the best trade-off between the bias and the variance of a Local Polynomial Approximation of the observed image conditional on the current segmentation. Additionally, for the segmentation model based on a Bayesian interpretation with two local kernels, we suggest to consider their values separately. Our proposition gives a smoother segmentation with less mis-localisations than the original method.

Comparative experiments of our method to other local region-based segmentation methods are carried out. The quantitative results, on simulated ultrasound B-mode images, show that the proposed scale selection strategy gives a robust solution to the intensity inhomogeneity artifact of this imaging modality. More general experiments on real images also demonstrate the usefulness of our approach.

Keywords : image segmentation, active contours, local region statistics, level set method, Intersection of Confidence Intervals, ultrasound images

Acknowledgements

Foremost, I would like to express my sincere gratitude to Dr. Djamel Boukerroui for supervising my PhD study and research. His guidance gave me much inspiration, and influenced the content of this work. I am so grateful to his continuous encouragements and advices during these years. In particular, I want to thank him for providing me numerous support in all stages of writing this thesis. I had received promptly detailed reviews, comments and corrections of my dissertation despite the amount of work at his end.

I would also like to thank those who served as my jury members : Prof. Olivier Basset, Prof. Jean-Marc Boucher, Prof. Jean-Pierre Cocquerez, Dr. Abdel-Ouahab Boudraa and Dr. Vincent Frement. Their time and energy are gratefully acknowledged. I want to appreciate very much for their detailed reviews, insightful comments, and inspired questions.

My sincere thanks also goes to Prof. Alison Noble (BioMedIA Laboratory, University of Oxford) for providing the helpful input.

I gratefully acknowledge the CSC (China Scholarship Council) for the financial support throughout these three and half years.

I would like to thank all administrative staff and colleagues of Heudiasyc, whose friendships and encouragements have made my experience at the University of Technology of Compiègne a memorable one. Much respect to Prof. Jean-FranLerallut for offering me the opportunity to do a PhD in France. I also want to thank my dear friends, Jiqiong Qiu, Julien Moras, Violaine Antoine, Aurore Lomet, Rym Nesrine Guibadj, Taha Arbaoui, Racha Elhajj, Xuqu Hu, Xuan Zhang, Jianquan Luo, Bin Li etc. The help received from them both personally and professionally is immense.

Last, but not least, I am grateful to my beloved parents and my boyfriend for always supporting me in what I was doing. This dissertation is dedicated to them.

Table des matières

| | |
|--|-------------|
| Résumé | vii |
| Abstract | ix |
| Acknowledgements | xi |
| Contents | xiii |
| List of tables | xvii |
| List of figures | xix |
| 1 Introduction | 1 |
| 1.1 Image segmentation | 2 |
| 1.2 Active contour models | 4 |
| 1.2.1 Parametric active contours | 5 |
| 1.2.2 Geometric active contours | 6 |
| 1.3 Region-based external energies | 7 |
| 1.4 Organisation of the dissertation | 8 |
| 2 Active contour models | 11 |
| 2.1 Introduction | 12 |
| 2.2 The snake model | 12 |
| 2.3 Geodesic snakes | 14 |
| 2.4 Implicit active contours | 15 |
| 2.4.1 Level set methods | 15 |
| 2.4.2 Curve evolution | 16 |
| 2.4.3 Numerical implementation | 18 |
| 2.4.4 Advantages and disadvantages | 19 |
| 2.5 Region-based external energies | 20 |
| 2.5.1 Mumford-Shah model | 21 |

| | | |
|----------|---|-----------|
| 2.5.2 | Segmentation as Bayesian inference | 21 |
| 2.5.3 | Parametric models | 23 |
| 2.5.4 | Non-parametric models | 30 |
| 2.6 | Conclusion | 33 |
| 3 | Local region-based methods | 35 |
| 3.1 | Introduction | 36 |
| 3.2 | Brox and Cremers model | 39 |
| 3.3 | Local intensity fitting model | 43 |
| 3.4 | Local intensity fitting with bias correction | 45 |
| 3.5 | General framework for region-based methods | 48 |
| 3.5.1 | Lankton and Tannenbaum model | 48 |
| 3.5.2 | Localised Bayesian interpretation | 49 |
| 3.6 | Conclusion | 51 |
| 4 | Optimal spatial adaptation for local region-based segmentation | 53 |
| 4.1 | Introduction | 54 |
| 4.2 | Denoising methods | 55 |
| 4.3 | Combination of global and local image statistics | 58 |
| 4.3.1 | A MAP-MRF framework | 58 |
| 4.3.2 | Local and global intensity fitting energy | 59 |
| 4.3.3 | Non-local active contours | 59 |
| 4.4 | Local region-based methods with adaptive scales | 60 |
| 4.4.1 | Piovano-Papadopoulo scale selection strategy | 60 |
| 4.4.2 | LPA-ICI rule | 62 |
| 4.4.3 | Proposed segmentation algorithm | 71 |
| 4.5 | Conclusion | 78 |
| 5 | Ultrasound image segmentation | 79 |
| 5.1 | Introduction | 80 |
| 5.2 | State of the art on ultrasound image segmentation | 81 |
| 5.2.1 | Statistics of speckle | 81 |
| 5.2.2 | Prior information | 82 |
| 5.3 | Justification of our approach | 84 |
| 5.4 | Experiments and discussion | 85 |
| 5.4.1 | Simulated ultrasound images | 86 |

| | | |
|----------|---|------------|
| 5.4.2 | Echocardiographic images | 95 |
| 5.4.3 | CT images | 96 |
| 5.5 | Conclusion | 96 |
| 6 | Conclusions | 101 |
| 6.1 | Conclusions | 101 |
| 6.2 | Future works | 102 |
| 6.3 | Publications | 104 |
| A | Minimisation of local region-based BC energy | 105 |
| A.1 | Gâteaux derivative | 105 |
| A.2 | Gâteaux derivative of the BC model's energy functional | 105 |
| B | Maximum likelihood segmentation with a Rayleigh distribution | 109 |
| C | Noise estimation methods | 111 |
| | Bibliographie | 115 |

List of tables

| | | |
|-----|---|-----|
| 2.1 | Common exponential families studied in [111]. See [202] for more examples. . . | 28 |
| 2.2 | Speed expressions of the examples of exponential distributions shown in Table 2.1, when minimising the anti log-likelihood associated energy with the ML parameters estimation [111]. | 29 |
| 3.1 | Region-based Segmentation Methods. $a \in \mathbf{R}^+$ | 49 |
| 4.1 | 2D polynomials ψ for the order $m \in \{0, 1, 2, 3\}$ | 63 |
| 5.1 | Statistics of the DSC errors and the MAD measures obtained on 60 simulated ultrasound images with 3 different initialisations. | 93 |
| C.1 | The values of real standard deviations and the estimated ones for the noisy images shown in Fig. C.1. | 112 |

List of figures

| | |
|---|----|
| 2.1 Segmentation example using snake model [51]. From left to right : input image with the initial contour, Gaussian-smoothed input image, the final segmentation. | 14 |
| 2.2 An example of an image with an active contour (left) and its implicit representation by a signed distance function (right). The contour C is shown in both images by the red curve. | 16 |
| 2.3 Natural change of topology in the curve evolution when it is represented implicitly by a level set function. The top row shows the curve evolution, and the bottom row shows the associated level set function. The initial contour is the one shown in Fig. 2.2. | 20 |
| 2.4 Segmentation example of a noisy image with global region-based methods. From the left to right : the noisy image and initialisation ; segmentation result using the CV model after 500 iterations ; result obtained by the Gaussian model. The image foreground and the background have the same mean but different variances. The red circle is the initial contour, and the magenta curve represents the final segmentation. Hereafter and unless otherwise specified, all the subsequent results use these two colours to label the initial and final contour. | 25 |
| 3.1 Examples of images with intensity inhomogeneities. | 36 |
| 3.2 Segmentation examples of synthetic images with inhomogeneities using global region-based methods | 37 |
| 3.3 Graphical representation of local region. The locality of point $\mathbf{x} \in C$ is defined by the interior of the blue circle. All points within this neighbourhood are classified as local interiors $\mathcal{O}(\mathbf{x}) \cap \Omega_i$ and local exteriors $\mathcal{O}(\mathbf{x}) \cap \Omega_o$ | 38 |
| 3.4 Influence of σ_p , the scale of the spatial kernel, on the terms $(I^2F_4 + IF_5 + F_6)$ in Eq. (3.6). We illustrate here the additional term of the seep function at the initial contours shown in Fig. 3.2. Note that they become important when σ_p decreases. | 40 |

| | | |
|-----|---|----|
| 3.5 | Segmentation examples with the local BC model. The figure illustrates the importance of the choice of an appropriate size for the local kernel. For ini. 1, the optimal scale should be between $\sigma_p = 14$ and 7; while for ini. 2, none of these scales led to an acceptable result. | 41 |
| 3.6 | Segmentation examples with the Gaussian fitting model Eq. (3.11). The figure illustrates the importance of the choices of kernel's sizes when $\sigma_e = \sigma_p$. The best scales are 2 for ini. 1 and 4 for ini. 2. Even these best results have mis-localisation problems at sharp corners. | 44 |
| 3.7 | Demonstration of a priori probability. For the marked points $\mathbf{x}_1, \mathbf{x}_2, \mathbf{x}_3$ along the contour C , the two partitions for \mathbf{x}_2 do not have equal probability. | 45 |
| 3.8 | Influence of the scale of the local kernel and the initialisation on the segmentation method using bias correction. From top to bottom : segmentation results and corresponding bias field estimations. $\nu = 650$ | 47 |
| 3.9 | Segmentation results of Eq. (3.21) when $\sigma_e = 1$. From left to right, the kernel size σ_p changes for the estimation of local region statistics. The above results are to be compared to Fig. 3.6 | 50 |
| 4.1 | Examples of ideal starshaped neighbourhoods [66]. From left to right : true image, illustration of ideal spatial neighbourhoods used for denoising at four different pixel locations. | 57 |
| 4.2 | Examples of optimal neighbourhoods obtained by the LPA-ICI rule using sectorial kernels [66]. Any two different sectors overlap only in the central point. Notice that the shape and the size of estimated windows are well adapted to image content at different pixel locations. This anisotropic kernel ensures the LPA-ICI filter to average only i.i.d. observations. | 57 |
| 4.3 | Image denoising example using the NLM and the anisotropic LPA-ICI. From left to right : the noisy image with SNR=14dB, the NLM and the anisotropic LPA-ICI denoising results. For the NLM, $\sigma_s = 2$, the similarity window $\tau = 5$, and $\sigma_I^2 = 0.9 \hat{\sigma}^2$, where $\hat{\sigma}^2$ is the estimated noise variance from the observed image. For the anisotropic LPA-ICI, the optimal scale is chosen from the set $\mathbf{h} = [3, 6, 9, 15, 21, 33]$, the parameter Γ controls the trade-off between bias and variance is 1.05, and the directional resolution is 8. | 58 |

| | | |
|------|--|----|
| 4.4 | Influence of the threshold ξ on the scale selection strategy proposed by Piovano and Papadopoulo. Top row : initial (red) and final (magenta) contour for three values of ξ . Bottom row : estimated sizes of the local kernels $\hat{h}(\mathbf{x})$, where \mathbf{x} are within a narrow band. The colourbar indicates the values of $\hat{h}(\mathbf{x})$. Image size is 128×128 , and $\mathbf{h} = [12, 14, 16, 18, 20, 22, 24, 27, 30, 33, 36, 40, 44, 48, 53, 58, 64, 70, 77, 84, 92, 100]$ | 61 |
| 4.5 | The kernels g_h of the smoothing filters in Eq. (4.15). From left to right, g_h are designed with a symmetric rectangular window and a Gaussian window (w_h) of the orders $m = 0$ (blue continues lines) and $m = 2$ (red dotted lines). Notice that the increase of m reduces the bandwidth of these low-pass filters. | 64 |
| 4.6 | The contribution of bias $\overline{m}_{\hat{J}_h}^2$ and variance $\overline{\sigma}_{\hat{J}_h}^2$ to the mean-square risk $r_{\hat{J}_h}$. The ideal scale h^* corresponds to the minimal $r_{\hat{J}_h}$ | 66 |
| 4.7 | Illustration of the idea and implementation of the ICI rule. Left image : the confidence intervals $Q_i = [L_i, U_i]$ are labelled by thick vertical lines. Right image : the successive intersections, marked by thick vertical lines, are decreasing with the increasing h_i | 67 |
| 4.8 | 1D denoising example using the LPA-ICI rule. From top to bottom : the noisy observation ; the noise free signal (red dotted line) and the LPA estimation (blue continuous line) of the order $m = 1$ with the symmetric Gaussian window, while the RMSE = 9.073 ; the corresponding adaptive window sizes \hat{h} obtained by the ICI rule for $\Gamma = 1$. The set of local windows size is $\mathbf{h} = [1, 2, \dots, 100]$ | 69 |
| 4.9 | 1D LPA-ICI denoising using higher order $m = 2$. The LPA estimations use symmetric Gaussian window. The RMSE is 8.6956. $\Gamma = 1$, $\mathbf{h} = [1, 2, \dots, 100]$. | 70 |
| 4.10 | 1D denoising using the anisotropic LPA-ICI approach. From top to bottom : adaptive windows sizes obtained respectively by the right and left Gaussian kernels, and the fused denoising result. $m = 1$, $\Gamma = 1$, $\mathbf{h} = [1, 2, \dots, 100]$, RMSE = 5.8462. | 70 |
| 4.11 | Demonstration of kernel sizes selection. Four pairs of points P_1, \dots, P_4 are studied. For each pair, one point locates inside and the other is outside of C (marked by green + and blue • respectively). The circle centred at each labelled point represents the size of local kernel. Left : scale estimations obtained by the LPA-ICI rule. Right : scale estimations after the maximum filtering operation. | 71 |

| | | |
|------|---|----|
| 4.12 | Segmentation example of images with inhomogeneities using the proposed method. From left to right : noise free images with initialisations, noise degraded images with segmentation results and the estimated kernel sizes for the final contour. The size of three images is 128×128 , and the local optimal scales are selected from the same \mathbf{h} used in Fig. 4.4. | 74 |
| 4.13 | Influence of the noise level on the estimation of local scales. Top : noisy image with SNR = 32dB, 8dB and 4dB. Point ‘1’ and ‘3’ (green +) belong to the foreground, and point ‘2’ and ‘4’ (red o) belong to the background. Bottom : the plot shows the estimated kernel sizes versus the image SNR values. The error bars are drawn from 20 repeated experiments when $\Gamma = 2.2$. The numbers ‘1’, ‘2’, ‘3’, ‘4’ on the left side of each curve represent the point number shown in the top image. Image size is 128×128 , and \mathbf{h} is the same set used in Fig. 4.12. | 75 |
| 4.14 | Influence of Γ on the estimation of local scales. The plot shows the estimation kernel size versus the Γ values. The error bars are drawn from 20 repeated experiments. Each curve represents the estimated kernel sizes for a point shown in Fig. 4.13. Left : SNR=16dB. Right : SNR=4dB. \mathbf{h} is the same set used in Fig. 4.12. | 76 |
| 4.15 | Comparison of the behaviour of two scale selection strategies. Top two rows : Piovano’s model [163], $\varepsilon = 0.5$. Bottom two rows : the proposed one [209], $\Gamma = 2.5$. From left to right : the curve evolution from the initial contour to the final contour with the corresponding estimated \hat{h} . Image size 128×128 , \mathbf{h} is the same set used in Fig. 4.12. | 77 |
| 5.1 | Segmentation results of the BC model (method (a)) on simulated ultrasound images with 3 different initialisations. From left to right column : images ‘PH1_45dB’, ‘PH2_35dB’ and ‘PH2_ATT_60dB’. Here, ‘45dB’ means a range of 45dB is used in log envelope compression. ‘Att’ means with images with attenuation simulation. $\nu = 2$ | 87 |
| 5.2 | Segmentation results of the local Gaussian fitting model (method (b)). From left to right column : images with 3 different initialisations used in Fig. 5.1. $\nu = 2$ | 88 |
| 5.3 | Segmentation results of method (c) . From left to right column : images with 3 different initialisations used in Fig. 5.1. $\sigma_e = 1$, $\nu = 2$ | 89 |

| | | |
|------|---|-----|
| 5.4 | Segmentation results of the local intensity fitting energy with bias correction algorithm (method (d)). From left to right column : images with 3 different initialisations used in Fig. 5.1. $\nu = 650$ | 90 |
| 5.5 | Segmentation results of the local region-based methods with adaptive scales (method (e) and (f)). From left to right column : images with 3 different initialisations used in Fig. 5.1. Top : Piovano and Papadopoulos's method, $\xi = 1$; bottom : our proposed method, $\Gamma = 2.5$. $\nu = 2$ | 91 |
| 5.6 | Behaviour of the automatic scale selection algorithms for method (e) and (f) . From left to right : the evolution of the segmentation and its corresponding local scales. The top two rows : Piovano and Papadopoulos's method, $\xi = 1$; bottom two rows : our approach, $\Gamma = 2.5$. $\nu = 2$ | 92 |
| 5.7 | Segmentation of a synthetic image by the intensity fitting model with bias correction (method (d)). The top row : segmentation results using $\sigma_p \in \{20, 12, 6\}$. Bottom row : the estimated bias filed corresponding to the above results. Image size 128×128 , $\nu = 650$. See figures 4.4 and 4.12 for the results obtained by method (e) and (f) | 94 |
| 5.8 | Segmentation of echocardiographic images using local region-based segmentation methods. Top three rows : the BC model, $\nu = 2$. Bottom two rows : the intensity fitting model with bias correction. Image size 208×208 , $\nu = 650$. 98 | |
| 5.9 | Segmentation of echocardiographic images using local region-based segmentation methods with scale selection strategies. Top : Piovano and Papadopoulos's model, $\xi = 0.5$; bottom : our approach, $\Gamma = 2.5$ | 99 |
| 5.10 | Segmentation examples of liver in 2D scans. The top two rows : the BC model with $\sigma_p = 10$ after 200 iterations and $\sigma_p = 5$ after 400 iterations. The bottom two rows : the Piovano and Papadopoulos's method ($\xi = 0.5$) and the proposed method ($\Gamma = 1.5$) after 200 iterations. Image size is 256×256 . $\nu = 2$. 100 | |
| C.1 | Original images and their noisy observations. Top two rows : noise free images and observations at four levels of an additive Gaussian noise with standard derivations $\sigma = \{2, 15, 25, 35\}$; bottom two rows : Rayleigh noise with $\sigma = \{4.63, 13.86, 23.03, 32.74\}$ | 113 |

Notations and Symbols

We tried to use, as much as possible, well-known notational symbology. Nevertheless, we declare some of them here below :

| | |
|-------------------------------|--|
| Ω | : Image domain, usually an open subset of \mathbb{R}^2 |
| $\{\Omega_r\}_{r=1}^N$ | : Subsets of Ω , where $\bigcup_{r=1}^N \Omega_r = \Omega$ and $\Omega_a \cap \Omega_b = \emptyset$ for $a \neq b$ |
| r | : Label of subregions. For two phase problems, $r = \{i, o\}$ |
| E | : Energy function to be minimised (or maximised) in image segmentation |
| E_D | : Data-driven term, external energy |
| E_R | : Regularisation term, internal energy |
| I | : Given image, observed image intensity |
| \mathbf{x} | : Point in Ω . For 2D image, the coordinate $\mathbf{x} = (x, y)^T$ |
| $I(\mathbf{x})$ | : Image intensity of pixel \mathbf{x} |
| ∇f | : Gradient of function f |
| $\nabla^2 f = \Delta f$ | : Laplacian of function f |
| $ \cdot $ | : Euclidean norm of a vector |
| C | : Curve in image domain |
| C_0 | : Initial contour, $C_0 = C(t = 0)$ |
| $C(s)$ | : Parametric Curve, $s \in [0, 1]$ is the normalised arc length |
| \vec{N} | : Unit inward normal of a curve |
| κ | : Mean curvature of a curve |
| ϕ | : Level set function |
| $H(\cdot)$ | : Heaviside function |
| $\delta(\cdot)$ | : Dirac function |
| $\mu(\mathbf{x})$ | : Piecewise smooth approximation of a given point |
| λ, ν | : Constant weighting parameters of regularisation terms |
| G_σ | : Gaussian kernel with a standard deviation σ |
| A_r | : Area of region Ω_r |
| μ_r, σ_r | : Mean intensity value and standard deviation of region Ω_r |
| $p(\cdot)$ | : Probability density function |
| $\boldsymbol{\eta}$ | : k -dimensional real parameter vector for exponential family |
| $\ddot{A}(\boldsymbol{\eta})$ | : Hessian matrix of A with $\ddot{A}(\mathbf{x}) = \frac{\partial^2 A}{\partial \boldsymbol{\eta}_1 \partial \boldsymbol{\eta}_2}$ |
| K_ρ | : Tonal kernel due to the Parzen estimator |
| $B(\cdot, \cdot)$ | : Bhattacharyya coefficient measures between two probability density functions |
| K | : Local kernel, usually a Gaussian one |
| h | : Radius of local kernel |

| | | |
|---|---|---|
| σ_p | : | Standard deviation of local kernel, used in estimation of local image statistics |
| σ_e | : | Standard deviation of local kernel, used in curve evolution |
| $\mathcal{O}(\mathbf{x})$ | : | Local region defined on point \mathbf{x} |
| $\mu_r(\mathbf{x}), \sigma_r(\mathbf{x})$ | : | Local mean intensity value and local standard deviation in region $\Omega_r \cap \mathcal{O}(\mathbf{x})$ |
| * | : | Convolution |
| J | : | Original noise free image |
| b | : | Bias field |
| n | : | Additive noise |
| \mathbf{h} | : | Finite set of ordered scale values |
| ξ | : | Threshold in the Piovano and Papadopoulo scale selection strategy |
| $r_{\hat{J}}$ | : | Mean-square risk of the approximation \hat{J} |
| g | : | filters built for the Local Polynomials Approximation |
| Γ | : | Threshold in the Intersection of Confidence Intervals rule |
| Q | : | Confidence intervals |
| \S | : | Section or subsection |

Abbreviations

| | |
|--------|--|
| $2D$ | : Two-Dimensional |
| PDE | : Partial Differential Equation |
| GAC | : Geodesic Active Contour |
| MS | : Mumford-Shah |
| MAP | : Maximum A Posteriori |
| pdf | : probability density functions |
| MRF | : Markov Random Fields |
| CV | : Chan-Vese |
| SNR | : Signal-to-Noise Ratio |
| MLE | : Maximum Likelihood Estimation |
| KLD | : Kullback-Leibler Divergence |
| i.i.d. | : independent identically distributed |
| BC | : Brox and Cremers |
| MSE | : Mean Square Error |
| LT | : Lankton and Tannenbaum |
| NLM | : Non-Local Means |
| LPA | : Local Polynomials Approximation |
| ICI | : Intersection of Confidence Intervals |
| RMSE | : Root Mean Square Error |
| DSC | : Dice Similarity Coefficient |
| MAD | : Mean Average Distance |

Introduction

Chapter summary

This chapter presents the work context of this thesis. First, we recall several basic concepts of image segmentation as well as some classical segmentation methods. In the field of variational segmentation approaches, the development of parametric and geometric active contour models will be briefly presented. Then, we focus on studying the latter with popular region-based external energies. Recently, local region statistics has been used in active contours, in order to segment images with intensity inhomogeneities. After the analysis of these existing techniques, ideas of combining global and local image statistics are addressed. And finally, we will put forward the structure of this dissertation.

Contents

| | |
|---|----------|
| 1.1 Image segmentation | 2 |
| 1.2 Active contour models | 4 |
| 1.2.1 Parametric active contours | 5 |
| 1.2.2 Geometric active contours | 6 |
| 1.3 Region-based external energies | 7 |
| 1.4 Organisation of the dissertation | 8 |

1.1 Image segmentation

Segmentation is one of the important problems in image processing. It aims at finding appropriate image characteristics, such as grey level, colour, texture, motion or prior knowledge, in order to distinguish objects of interest from the background or from other objects at the same time. More specifically, image segmentation can be formally described as :

Definition 1.1. *Let Ω be an image domain. Image segmentation refers to the process of partitioning Ω into disjoint subsets $\{\Omega_r\}$, $r = 1, \dots, N$, which satisfy [88] :*

1. $\bigcup_{r=1}^N \Omega_r = \Omega$;
2. $\Omega_a \cap \Omega_b = \emptyset$, $\forall a \neq b$;
3. $P(\Omega_r) = \text{true}$, $\forall r$;
4. $P(\Omega_a \cap \Omega_b) = \text{false}$, $\forall a \neq b$.

$P(\cdot)$ is a logical predicate defined on groups of connected pixels.

After segmentation, an observed image is converted to a more meaningful partition. Therefore, segmentation is considered as building a connection between low level information and objects, and in this sense it is closely related to the issue of object recognition in computer visions.

Image segmentation is usually considered as an initial and vital step to further image analysing and understanding in various application domains. For example, segmentation is used to classify earth surface images acquired by satellite into roads, forests, houses and so on [16] ; in diagnostic imaging, segmentation helps to automate or facilitate the delineation of anatomical structures [162, 146] ; motion and spatio-temporal segmentation techniques are developed for moving objects [219]. Segmentation can also be used in content-based image retrieval [116], machine recognition of faces [221] and identifying fingerprints [128]. Generally speaking, the detection, extraction and analysis of objects of interest are inseparable from image segmentation. Image segmentation has been extensively researched, and the literature can be classified mainly based on image information on two major categories, namely edge-based methods and region-based methods [69, 153, 185, 78, 7]¹.

Edge-based methods : Edge-based segmentation methods, also known as edge detection, are somehow similar to the visual process of human, which is first attracted by the fast changing area of a scene and by the intersection of different objects. The

1. The survey of this entire field is beyond the scope of this work. The proposed classification does not include hybrid techniques, most of which are based on the integration of edges and region-based methods [44, 80, 160, 84, 7, 187].

position of an edge, in other words, the location of discontinuities in the geometry, is mathematically given by an extreme of the first-order derivative of the image intensity function. Unfortunately, taking image derivatives leads to accentuate high frequencies, and hence amplifies noise. It is therefore prudent to smooth the image with a low-pass filter prior to compute the gradient. Considering the response of edge detectors should be independent of orientation, an isotropic smoothing filter is desirable. The Gaussian filter is mostly used, while alternative ones are proposed by a number of literature [36, 54, 68, 224, 155]. As an alternative approach to find the maxima in the gradient magnitude, edges can be detected by looking for zero crossings of the second-order derivatives, for example using the Laplacian of Gaussian or the Difference of Gaussians [129]. Haralick's facet model also uses this detection mechanism [83]. It is also important to note that a more general formalism of features detection of any type of discontinuity (not only step edges) exists in the literature. Such model has been widely studied after the publication of the local energy model [137]. It postulates that the discontinuities can be defined and classified by using their local phase. This observation led to the development of a number of detection algorithms based on the local phase information (see eg. [64, 65, 108, 79, 21, 201, 53]).

Classical edge-based segmentation methods, however, cannot guarantee to have continuous and closed boundaries. Additionally, a fundamental property of edges operators is that they are defined with respect to certain spatial sizes. Therefore, to deal with noisy and physically corrupted data is usually a limitation of single scale methods. To figure out these difficulties, common solutions may include for instance, scale selection and blur estimation algorithms [204, 125, 60, 149], statistical models based detection [107], linear scale space methods [124] and non-linear diffusion techniques that preserve edges [161, 198, 199].

Region-based methods : Region-based segmentation methods concentrate on grouping image pixels based on a similarity measure of image features, rather than on detecting isolated points or discontinuities of image intensities. Most of these methods are statistical in nature. The simplest possible technique to segment a grey level image is histogram thresholding [78]. However, this algorithm, even with a globally optimised threshold, is rarely sufficient as soon as the object of interest contains different grey level values or if the background is not uniform.

Formally, histogram thresholding belongs to a larger class of region-based segmentation methods called classification methods. They are based on the estimation of

a density function of the observed image data or of a set of attributes (texture features for example) calculated from the observed image. This set of methods can also be classified based on the assumed probability density function, parametric or non-parametric, on the classification algorithm or whether prior is used to learn the classes. This class of methods is also called mode finding techniques and includes popular methods such as the k -means [126, 85], mixture Models and Expectation-Minimisation methods (see eg.[17]) and Mean shift methods [70, 43].

An alternative to mode finding techniques, splitting algorithms [147] recursively divide an image into small pieces by region-based statistics, and region merging-growing algorithms [29, 41, 3] amalgamate pixels and regions in a hierarchical way. Accordingly, it is possible to combine both splitting and merging in a medium-grain segmentation [88, 160], which partitions an image into connected subregions and groups neighbour parts sharing certain features. Recent contributions in this class of methods make also use of edge cues and generally exploit the image lattice as a graph [187].

Region- and edge-based segmentation techniques rely on two different but complementary concepts. Schematically, region methods are less sensitive to noise and can model complex textures. Edge features are generally robust to low intensity inhomogeneities and have superior localisation properties. They are however very sensitive to image contrast and fail on images with a low signal to noise ratio or textured images. These observations have led to the development of new classes of methods that intrinsically integrates both region- and edge-based information. For instance, the introduction of active contour in segmentation has overcome many limitations of traditional methods. The following section will briefly review their theories and developments.

1.2 Active contour models

The original formulation of active contour models, first proposed in the late 80s [96, 189], is a mechanism to bring a certain degree of prior knowledge to bear on low-level image interpretation [136, 177, 150]. These active contour models define a simple closed curve $C \subset \Omega$, and attempt to minimise an energy function associated to this current C as a sum of internal and external energies. Internal energies model the prior on the desirable solution in terms of smoothness, length, shapes and so on. External energies are image-driven, which are supposed to be minimal when the regions inside and outside of C are statistically homogeneous. There exist two main families of external energies : edge-based

and region-based. The latter relies on statistical modelling of the given image intensity. It has been observed that region-based external energies outperform edge-based ones in most application domains. This is the case for example in medical applications.

A natural and common way to solve the minimisation problem is the use of a gradient decent algorithm. Variational tools are generally utilised and the minimisation leads to solve a Partial Differential Equation (PDE) iteratively. Although global optimisations have been introduced recently [26, 214], the evolution of the active contour stops generally at a local minimum of the energy function. Hence, initialisations and the design of energies with few local minima or convex energies have always been a concern. According to different representations of C , there are two main categories within the family of active contour models : parametric and geometric.

1.2.1 Parametric active contours

Parametric active contour models use an explicit description of the curve C during its deformation. Originally introduced by Kass et al. [96], the snake model allows to move the curve by the influence of the internal and the external energies. The internal ones constrain the regularisation of snakes ; while the external ones, traditionally based on the gradient magnitude of a Gaussian smoothed version of the observed image, push the snake toward salient image features. The snake model has the advantage of obtaining closed segmentation curve, and also benefits from efficient algorithms in searching for a minimal energy state.

However, the snake model has several disadvantages because its external energy is basically an edge detector :

1. The capture range of the external force is small because the external force decreases rapidly at image positions far from the edges of objects of interest.
2. The external energy is sensitive to noise, which can lead to an undesirable local minimum.

Thus, it is necessary to place the initial contour close to the real boundaries. It is important to highlight that the choice of the sampling rule in space of the curve affects the performance of parametric active contours. A re-sampling step is necessary throughout the curve evolution process. Other limitations of parametric models include their inability to support topological changes and the increase of implementation difficulties to their generalisation to higher dimensions. To solve these problems, many alternative parametric methods have been proposed [203, 131, 38, 18].

A large number of researchers have studied the problem of sensitivity to the initial contour [46, 37, 127, 131, 208]. Among them, Cohen [46] introduced a Balloon force in the external energy, which inflates or deflates the contour in order to prevent the contour being stuck at a local minima. This technique extends the external force to a much larger range over the image domain, and consequently the initial contour needs no longer to be very close to the desired solution. Xu and Prince [208] proposed the Gradient Vector Flow in order to make the information of the image gradient non-local. This method allows the image gradient to diffuse. Thus, the active contour is able to segment non-convex objects. Recent methods have also the ability to capture concavities and include the Charged-Particle Model [91], the Charged Active Contour based on Electrostatics [211] and the Vector Field Convolution (VFC) [117].

Regarding the second drawback of snakes, the combination of edge-based and region-based external energies has been proposed by [168, 222]. Zhu and Yuille [222] presented a region competition method in a Bayesian framework which minimises a Minimum Description Length (MDL) criterion. As an alternative to the variational approach, Dynamic Programming minimisation strategies have also been applied. These techniques avoid the estimation of higher order derivatives and improve the numerical stability of the algorithm [6, 46, 203, 47, 168, 131, 222, 208, 75].

1.2.2 Geometric active contours

Geometric models implicitly represent the curve propagation as the zero level sets of a high-dimensional function. They allow for automatic topology changes, such as merging and splitting. The implicit formulation of snakes is introduced by Caselles et al. [37] and Malladi et al. [127]. These models are built on the curve evolution theory [174, 4, 103, 104] and level set methods [151, 177]. This implies that the evolution is independent of the parameterisation of the curve. The evolution speed of the curve is a function of the curvature and the image characteristics such as the gradient. Curvature acts as an internal force to regularise the contour. Oppositely, the data-driven external force makes the curve stop on the desired boundaries.

The authors in [38, 212] prove that the minimisation of the internal energy is equivalent to the minimal length of the contour in a Riemannian space. Niessen et al. [143] compared different level set methods in [127, 38, 212], and introduced a new geodesic active contour model to segment multiple objects. The method of Cohen and Kimmel [45] allows to find the path, which is a global minimum energy between two points. The methods described in the articles [51, 115, 42, 169, 191, 28, 52, 173] are examples of using shape prior knowledge

in the context of level sets active contours.

The main disadvantage of geometric active contour models is their high computational costs, due to the evolution and the re-initialisation of a high-dimensional surface. In order to accelerate these calculations, various techniques have been proposed [2, 199, 184, 150, 121, 114, 26, 182]. The narrow band method [2] updates the level set function, ϕ , in a small neighbourhood of interest around C instead of the whole image domain. Splitting Operators [199, 105, 158], whose basic idea is to decompose a multi-dimensional problem into one-dimensional cases, are very efficient methods as large time step can be used. In order to avoid solving the Euler-Lagrange equation of the underlying variational problem, Song and Chan [184] calculate the energy directly and check if the energy decreases when a point changes label from inside to outside or vice versa. In order avoid the re-initialisation procedure, Li et al. [121, 118] have introduced an internal energy, which maintains the level sets close to a signed distance function. The Alternating Direction Explicit [114] method can be easily parallelised, and is also unconditionally stable, thereby it allows fast convergence. In order to avoid local minima of the energy function, an unification of segmentation and denoising into a global minimisation framework has been presented in [26]. Shi and Karl [182] have proposed a two-cycle algorithm to approximate level-set-based curve evolution without the need of solving partial differential equations. A very recent approach studied the representation of the level set function using radial basis functions (RBFs) [72, 207, 13]. Therefore these are parametric representations of the level set function but are still implicit representations of the contour. The main advantage is to the transform the initial PDE problem to an Ordinary Differential Equation (ODE) problem, which is easier to solve.

1.3 Region-based external energies

The use of region-based external energies in active contour methods, mostly within the level set framework, led to a considerable improvement in efficiency and robustness. For instance, the Chan and Vese model [40] considers an image's background and foreground as constant intensities represented by their mean values. This one of the simplest region energies that assumes that original image is piecewise constant. The mean separation method of Yezzi et al. [213] relies on the assumption that the object of interests should have maximally different intensities from the background. It is important to highlight that this model does not make such a strong assumption as a piecewise constant image as in [40]. More complex statistical models can also be used within this framework. A straightforward

approach is to define the external energy as minimisation the log likelihood of the observed image intensities within each region. Examples for the Gaussian distribution [170], the Rayleigh distribution [175] and general models such as the exponential family [113] exist. Non-parametric region-based energies have also been proposed [102, 171, 133], which allow to model complex intensity distributions of observed images.

These region-based active contours, however, fail to segment images with strong intensity inhomogeneities, which is almost unavoidable in real data. Indeed, when the object of interests cannot be easily distinguished in terms of global image statistics, region-based external energies may lead to erroneous segmentations. To overcome this problem, some work has been recently carried out in utilising local image statistics within the level set paradigm [32, 109, 120, 196]. The idea is to use local image statistics for the estimation of the image model parameters along the contour (inside and outside). The locality is defined generally by an isotropic window of a given scale. It has been shown that localised segmentation methods have the ability to capture the boundaries of inhomogeneous objects.

Such techniques, however, are found to be less robust to noise than global ones. Also, they could be sensitive to initialisations if the size of locality is not appropriate. Indeed, if the window size is small, the information might be insufficient to locally evolve C ; a bigger window, however, might cause a bias estimation of local model parameters and make the segmentation algorithm lose its local advantages. Therefore, it brings out several problems that need to be addressed, such as :

1. Can global and local image statistics be combined in one model ?
2. Is it possible to define a pixel-dependent local scale while estimating image statistics ?

These two questions are extremely important when local image statistics are utilised in image segmentation. There has been an increasing number of literature which uses local region-based external energies in level set methods, since their first introduction in 2007. However, to our knowledge, hardly any of these works analysed the importance of choosing appropriate local scales.

1.4 Organisation of the dissertation

In this thesis, we aim at studying segmentation methods for images with intensity inhomogeneities. To solve this challenging problem, we begin by the review of some typical region-based segmentation techniques, and particularly the ones considering local image

information. We will then focus on discussing the open questions that arose in the previous section. Finally, we will propose new methods that address these difficulties.

The remaining parts of the thesis are organized as follows :

Chapter 2 will introduce the state of the art on segmentation methods using parametric and geometric active contours. We will highlight the latter, and concentrate on region-based external energies within the level set framework, which are the basis for the succeeding chapters.

In Chapter 3, we will present and discuss recently proposed local region-based segmentation methods. General formulations for region-based segmentation models are explained, with the principles of using local image statistics to form the data energy term. For the algorithm based on a Bayesian interpretation with two local kernels, we suggest to consider their values separately.

In Chapter 4, we propose within the level set framework a segmentation method based on local image region statistics. Inspired by recent development by the image denoising community, we use the Intersection of Confidence Intervals approach to define a pixel-dependent local scale for the estimation of image statistics. The obtained scale is based on estimated optimal scales, in the sense of the mean-square error of a Local Polynomials Approximation (LPA) of the observed image conditional on the current segmentation. In other words, the scale is optimal in the sense that it gives the best trade-off between the bias and the variance of the LPA of the local image patches (inside and outside) along the contour.

Chapter 5 will first review the methodology of ultrasound image segmentation. We will give some segmentation results on simulated and real ultrasound images. Quantitative evaluations of these tests are also presented, in order to demonstrate the improvement on robustness and accuracy of the proposed segmentation method.

Finally, conclusions of the present work will be summarized in the last chapter. We discuss a number of limitations of the proposed methods and point out directions of ongoing and future work.

Active contour models

Chapter summary

This chapter gives a brief review of some state of the art on image segmentation using active contour models. First, we will present the basic idea of active contour models and introduce a general energy function to be optimised. Then, two well-known categories of active contour models, namely parametric and geometric, will be described. In this context, we study several typical segmentation methods, especially geometric ones. Within this framework, different image statistics and noise models are discussed in order to build region-based external energies.

Contents

| | |
|---|-----------|
| 2.1 Introduction | 12 |
| 2.2 The snake model | 12 |
| 2.3 Geodesic snakes | 14 |
| 2.4 Implicit active contours | 15 |
| 2.4.1 Level set methods | 15 |
| 2.4.2 Curve evolution | 16 |
| 2.4.3 Numerical implementation | 18 |
| 2.4.4 Advantages and disadvantages | 19 |
| 2.5 Region-based external energies | 20 |
| 2.5.1 Mumford-Shah model | 21 |
| 2.5.2 Segmentation as Bayesian inference | 21 |
| 2.5.3 Parametric models | 23 |
| 2.5.4 Non-parametric models | 30 |
| 2.6 Conclusion | 33 |

2.1 Introduction

Classical image segmentation methods use mainly low level image features. They cannot account for prior knowledge to get a desirable solution. Due to this lack of constraints, their performances highly depend on image quality. Active contour models [18] can help to overcome these difficulties. Their basic idea is to minimise an energy E that evolves a two-dimensional (2D) curve towards image features. It is a powerful mechanism to bring a certain degree of prior knowledge to low-level image interpretation. The general active contour model is described as :

$$E(C) = \oint (E_D(C) + E_R(C)) dC , \quad (2.1)$$

where the curve C is a set of boundaries that separates different image components. The external energy E_D , also called fidelity term, is data-driven ; the internal energy E_R models the regularisation of C . By minimising the above energy function, the propagation of C is driven by both external and internal forces. This model can use some high level information and can ensure the smoothness of C .

According to the representation of the curve C , active contour models are classified into two main types : parametric and geometric. Parametric active contours directly describe the curve C , which allows a real-time implementation ; and geometric ones use an implicit representation, which can naturally deal with topological changes of C . Even though these two methods have different forms in describing their image-driven and regularisation forces, they follow similar principles in curve evolution. In this chapter, we will briefly review both with some typical examples.

2.2 The snake model

The snake model proposed by Kass et al. [96] is the first active contour model. It uses a parametric representation of the curve :

$$C(s) = (\mathbf{x}(s)) : s \in [0, 1] \rightarrow \Omega ,$$

where $\mathbf{x} \in \mathbb{R}^2$ is the coordinate of the contour C , and s is the normalised arc length. The snake model deforms this continuous and elastic curve to fit the nearest salient image characteristics. For any observed image $I : \Omega \rightarrow \mathbb{R}$, the evolution of C is given by the minimisation of the following energy function :

$$E_{\text{snake}}(C) = \int_0^1 \underbrace{\frac{1}{2} \left(\alpha(s) \left| \frac{\partial C(s)}{\partial s} \right|^2 + \beta(s) \left| \frac{\partial^2 C(s)}{\partial s^2} \right|^2 \right)}_{E_R} \underbrace{- |\nabla I(C(s))|^2}_{E_D} ds , \quad (2.2)$$

where $\frac{\partial C(s)}{\partial s}$ and $\frac{\partial^2 C(s)}{\partial s^2}$ denote the derivatives with respect to the curve parameter, $\alpha(s)$ and $\beta(s)$ are non-negative parameters, and ∇ represents the spatial gradient operator.

The first two terms here correspond to the internal energy in Eq. (2.1), which constraints the geometry of C . More specifically, the first-order differential measures the rate of changes in the length of C ; the second-order one is a rigidity term that makes the snake maintain its original smoothness and shape. Their importance are adjusted by the weights $\alpha(s)$ and $\beta(s)$ respectively. In the absence of other constraints, the internal energy of snakes simply makes C collapse to a point. The external energy term of the snake model is an edge term. It is used to control external attraction forces which drive C towards desired edges.

The segmentation problem now turns to find a parametric curve that minimises both internal and external energies defined in Eq. (2.2), which can be solved by the Euler-Lagrange equation as follows :

$$\frac{dE_{\text{snake}}}{dC} = -\frac{\partial}{\partial s} \left(\alpha(s) \frac{\partial C(s)}{\partial s} \right) + \frac{\partial^2}{\partial s^2} \left(\beta(s) \frac{\partial^2 C(s)}{\partial s^2} \right) - \nabla |\nabla I(C(s))|^2 = 0 . \quad (2.3)$$

This partial differential equation (PDE) expresses the balance of internal forces (first two terms) and external forces (last term), when the contour rests at equilibrium. Under these two forces, C can be attracted to the boundary of the targeted object. For simplicity, $\alpha(s)$ and $\beta(s)$ are usually assumed to be constants. Suppose an artificial time t and a initial contour C_0 , the motion function to minimise the snake energy Eq. (2.2) by iterative gradient descent is given by :

$$\begin{aligned} \frac{\partial C(s, t)}{\partial t} &= -\frac{dE_{\text{snake}}}{dC} \\ &= \alpha \frac{\partial^2 C(s)}{\partial s^2} - \beta \frac{\partial^4 C(s)}{\partial s^4} + \nabla |\nabla I(C(s))|^2 . \end{aligned} \quad (2.4)$$

$$C(s, 0) = C_0 .$$

The snake model can guarantee a smooth and continuous segmentation contour, but there still exists several limitations. The initial contour C_0 should be located in the vicinity of the real boundary; otherwise, snakes may converge to a wrong result. Indeed, the external energy term in Eq. (2.4) is basically an edge detector, therefore its value is relatively large around the image boundaries and smaller in uniform regions. As illustrated in Fig. 2.1, the input image is a uniform grey square on a uniform white background. In order to create a sufficiently large basin of attraction, the input image is first Gaussian-smoothed as shown in the middle of Fig. 2.1. Due to this procedure, the edge gradient

is noticeable at a larger range. However, this smoothing process will lead to an over-smoothed biased segmentation, for instance without sharp corners and fine details, as illustrated on the example given in the right of Fig. 2.1.

Balloon force

As we have mentioned earlier in the last chapter, several methods have been proposed to improve the performance of the snake model. One popular and simple solution consists on the addition of a new internal energy term to Eq. (2.2), in order to make the model behave like an inflatable balloon [46] :

$$E_{\text{Ballons}}(C) = \gamma \int_{\Omega_i} dx , \quad (2.5)$$

where Ω_i represents the region inside of the closed curve C . The balloon force either shrinks ($\gamma > 0$) or expands ($\gamma < 0$) the contour C constantly. Therefore, we need to know in advance whether the initial contour is located inside or outside of the object of interest. Moreover, the magnitude of γ can lead to a biased segmentation, which, in practice, can be minimised by decreasing the magnitude of γ during the curve evolution.

2.3 Geodesic snakes

The original snake model Eq. (2.2) can be generalised by replacing its external energy $-|\nabla I|^2$ with a family of edge detectors $g(|\nabla I|)^2$ [38]. Let $g : [0, +\infty[\rightarrow \mathbb{R}^+$ be a strictly decreasing function, which satisfies $\lim_{s \rightarrow \infty} g(s) = 0$. Assume the rigidity term here is not particularly important ($\beta = 0$). A smooth curve can also be obtained only with the first internal term. Therefore, the energy function of the geodesic active contour (GAC) model

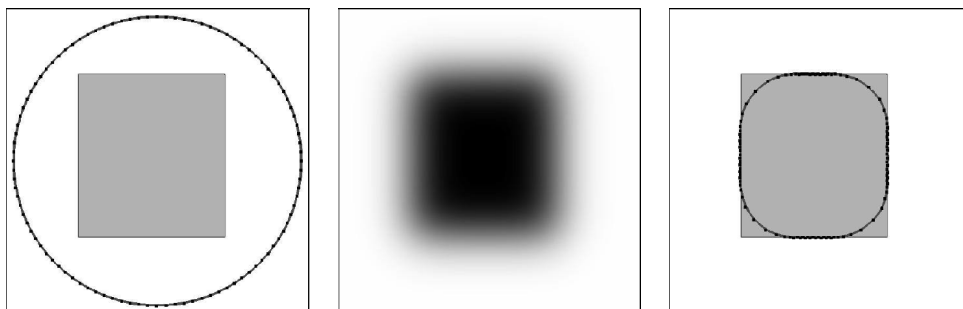


Figure 2.1 – Segmentation example using snake model [51]. From left to right : input image with the initial contour, Gaussian-smoothed input image, the final segmentation.

is formed as [38] :

$$E_{\text{GAC}}(C) = \alpha \int_0^1 \left| \frac{\partial C(s)}{\partial s} \right|^2 ds + \int_0^1 g(|\nabla I(C(s))|)^2 ds , \quad (2.6)$$

Caselles et al. also proved in [38] that by applying the Maupertuis' principle of least action, the minimisation of the above energy is equivalent to :

$$\min \int_0^1 g(|\nabla I(C(s))|) \left| \frac{\partial C(s)}{\partial s} \right| ds . \quad (2.7)$$

This can be considered as searching a geodesic curve, for instance a curve of minimal distance path between given points, in a Riemannian space. The infinitesimal contour length dC or $\left| \frac{\partial C(s)}{\partial s} \right| ds$ is weighted by the edge detector $g(\cdot)$. Using calculus of variations the Euler-Lagrange equation for the minimisation of Eq. (2.7) is given by :

$$\frac{\partial C(s, t)}{\partial t} = g(|\nabla I|) \kappa \vec{N} - (\nabla g \cdot \vec{N}) \vec{N} , \quad (2.8)$$

where κ is the Euclidean curvature of C , and \vec{N} denotes the unit inward normal. The first term of the right hand side of this equation is a curve shortening flow, which smooths C by means of decreasing its total length. Commonly, the first term can be extended by replacing κ with $\kappa + \gamma$, so that a shrinking or an expansion force, similar to the balloon force, is included. The second term works in a neighbourhood, satisfying $\nabla g \neq 0$, which provides an attraction to drive C towards the large image gradient. Hence, the function g does not need to be zero to stop the evolution of the snake. Since geodesic snakes also use an edge-based external energy, their performances also depend on the initial contour.

2.4 Implicit active contours

2.4.1 Level set methods

Parametric active contour models track the evolution curve explicitly, which are good at capturing fine and irregular details. They are topologically rigid, meaning that no contour splitting and merging is possible. Furthermore, if the shape of the curve varies dramatically, re-parameterisations may also be required during the evolution. To overcome these limitations, an implicit representation for such closed contours, the level set method, has been proposed by Osher and Sethian [151]. Level sets are mathematical tools to represent the front propagation. They track the curves as the zero crossing level of a higher-dimensional characteristic function, which can handle topological changes of evolving interfaces and can avoid the issues of contour parameterisations. Since their

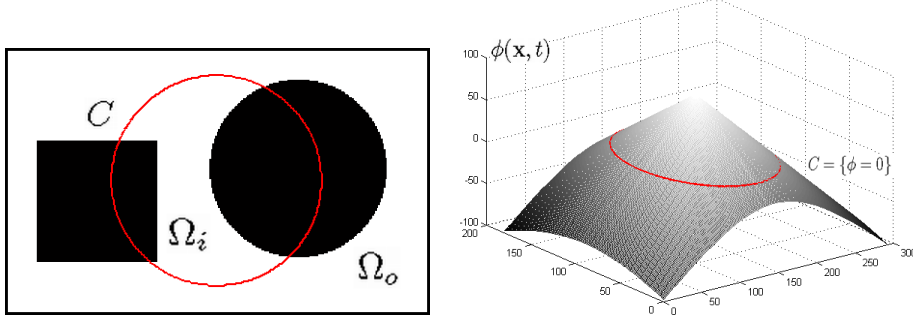


Figure 2.2 – An example of an image with an active contour (left) and its implicit representation by a signed distance function (right). The contour C is shown in both images by the red curve.

first application to edge-based segmentation algorithms, level set methods have been extensively studied and have become a popularly used general framework for image segmentation [127, 38, 177, 150].

Suppose a simple closed curve $C(s, t)$ is contained in an open region Ω . The propagation speed of C along the normal \vec{N} has the form of :

$$\begin{cases} \frac{\partial C(s, t)}{\partial t} = F(\kappa) \cdot \vec{N} \\ C(s, t = 0) = C_0 \end{cases}, \quad (2.9)$$

where F is the speed function which may depend on the curvature κ . In order to track this moving front implicitly, the level set function $\phi(\mathbf{x}, t)$, $\mathbf{x} \in \Omega$ is introduced to describe this problem.

$$\phi(\mathbf{x}, t) = \begin{cases} d(\mathbf{x}, C(s, t)) & \mathbf{x} \in \Omega_i \\ 0 & \mathbf{x} \in C(s, t) \\ -d(\mathbf{x}, C(s, t)) & \mathbf{x} \in \Omega_o \end{cases}, \quad (2.10)$$

where d is a distance function, which measures the distance from a point \mathbf{x} to C at time t ; Ω_i and Ω_o are the inside and the outside regions separated by the curve C .

For example in Fig. 2.2, the input grey level image has two objects, and the curve at time t is given by a red circle. The corresponding signed distance function and the implicit representation of C are illustrated in the right side of the same figure. The zero level set is represented by $C(s, t) = \{\mathbf{x} | \phi(\mathbf{x}, t) = 0\}$. $\phi < 0$ and $\phi > 0$ divide the image into an inside and an outside of C respectively.

2.4.2 Curve evolution

Given the PDE that commands the deformation of the curve, one can derive the corresponding PDE with the level set function. By applying the chain rule to the expression

of the zero level set in Eq. (2.10), i.e. $\phi(C, t) = 0$, we get :

$$\frac{\partial \phi}{\partial C} \cdot \frac{\partial C}{\partial t} + \frac{\partial \phi}{\partial t} = 0 .$$

Combining the above formula with Eq. (2.9), it can be rewritten as :

$$\begin{aligned} \nabla \phi \cdot F(\kappa) \cdot \vec{N} + \frac{\partial \phi}{\partial t} &= 0 , \quad \text{where } \vec{N} = -\frac{\nabla \phi}{|\nabla \phi|} , \\ \implies -F(\kappa) \cdot |\nabla \phi| + \frac{\partial \phi}{\partial t} &= 0 . \end{aligned}$$

This is a Hamilton-Jacobi type of equation, and $\nabla \phi$ is the normal to C . Thus, the motion of C is represented by the evolution of the zero level set, which satisfies the following PDE :

$$\begin{aligned} \frac{\partial \phi}{\partial t} &= F(\kappa) \cdot |\nabla \phi| , \quad (2.11) \\ \phi(\mathbf{x}, t = 0) &= d(\mathbf{x}, C_0) = \phi_0 . \end{aligned}$$

Solving numerically the above PDE has been extensively studied [152]. Cares must be taken when choosing the appropriate finite difference schemes for the approximation of the derivatives of ϕ . Consequently, Sethian and Strain [178] have proposed to decompose the speed function $F(\kappa)$ into two terms :

$$F(\kappa) = F_0 + F_1(\kappa) , \quad (2.12)$$

where F_0 is a constant speed term (an advection term), thus an upwind discretisation scheme should be used; F_1 depends on geometric properties of the curve C via the curvature κ , hence it can be approximated by a central difference scheme.

Malladi et al. [127] have proposed to modulate the above speed function with a data term, which is used to constrain the evolution of the curve C to stop at desired image feature. Specifically, they proposed the use of one of the following edge stopping functions :

$$g_I = \frac{1}{1 + |\nabla I_\sigma|} \quad \text{or} \quad g_I = e^{-|\nabla I - \sigma|} ,$$

where I_σ denotes a Gaussian smoothed version of the observed image. The value of g_I is close to unity in homogeneous regions, and it drops to zero at high gradient image locations. The image-based term g_I is meaningful only on the curve C , i.e. at zero level of ϕ . The level set evolution equation however applies for the entire image domain Ω . Consequently, g_I is extended to other level of ϕ , and $\widehat{g}_I(\mathbf{x})$ is defined equal to value of g_I on the closest point to \mathbf{x} on the zero level set. The motion function Eq. (2.11) then becomes as follows [127] :

$$\frac{\partial \phi}{\partial t} = \widehat{g}_I(F_0 + F_1(\kappa))|\nabla \phi| .$$

2.4.3 Numerical implementation

Lets take the geodesic snakes as an example. Using the tools presented in the previous section, the evolution equation Eq. (2.8) can be expressed within the Level set paradigm. When adding also a balloon force, the contour evolution can be implicitly represented by the following equation :

$$\frac{\partial \phi}{\partial t} = \underbrace{g \operatorname{div} \left(\frac{\nabla \phi}{|\nabla \phi|} \right)}_{F_1(\kappa)} |\nabla \phi| + \underbrace{[(\nabla g \cdot \nabla \phi) + \gamma g]}_{F_0} |\nabla \phi| . \quad (2.13)$$

As mentioned in § 2.3, the first term of this function moves the curve in the direction of its curvature under the influence of the modulation function $g(I)$, and acts as a curve smoothing term ; the second term encourages the curve to migrate towards minima of $g(I)$. We also highlight here that, the balloon force is also modulated by the edge stopping function.

We will denote the discrete version of $\phi((i\Delta x, i\Delta y), n\Delta t)$ by $\phi_{i,j}^n$, where Δt is the time step and Δx and Δy are the spatial grid sizes. It is natural and hence common in the image processing community to use a uniform spatial grid (i.e. $\Delta x = \Delta y = 1$).

Right side : Considering the right side of Eq. 2.13 :

1. The first term is approximated as :

$$g \operatorname{div} \left(\frac{\nabla \phi}{|\nabla \phi|} \right) |\nabla \phi| = g \frac{\phi_{ii}\phi_i^2 - 2\phi_i\phi_j\phi_{ij} + \phi_{jj}\phi_j^2}{\phi_i^2 + \phi_j^2 + \varepsilon} , \quad (2.14)$$

where ε is a small positive constant, in order to avoid numerical instabilities. The first and second derivatives of $\phi(\mathbf{x})$ are approximated by a central difference scheme as follow :

$$\begin{aligned} \phi_i &\approx \frac{1}{2}(\phi_{i+1,j} - \phi_{i-1,j}) , & \phi_j &\approx \frac{1}{2}(\phi_{i,j+1} - \phi_{i,j-1}) , \\ \phi_{ii} &\approx (\phi_{i+1,j} - 2\phi_{i,j} + \phi_{i-1,j}) , & \phi_{jj} &\approx (\phi_{i,j+1} - 2\phi_{i,j} + \phi_{i,j-1}) , \\ \phi_{ij} &\approx \begin{cases} 2\phi_{i,j} + \phi_{i-1,j} + \phi_{i+1,j} + \phi_{i,j-1} + \phi_{i,j+1} - \phi_{i-1,j+1} - \phi_{i+1,j-1}, & \text{if } \phi_i\phi_j \geq 0 \\ 2\phi_{i,j} - \phi_{i-1,j} - \phi_{j+1,i} - \phi_{i,j-1} - \phi_{i,j+1} + \phi_{i-1,i-1} + \phi_{i+1,j+1}, & \text{otherwise} \end{cases} . \end{aligned}$$

2. An upwind scheme is used for the discretisation of the second term :

$$\begin{aligned} (\nabla g \cdot \nabla \phi) |\nabla \phi| &= \max(g_i, 0) \underbrace{(\phi_{i+1,j} - \phi_{i,j})}_{D_i^+ \phi_{i,j}} + \min(g_i, 0) \underbrace{(\phi_{i,j} - \phi_{i-1,j})}_{D_i^- \phi_{i,j}} \\ &+ \max(g_j, 0) \underbrace{(\phi_{i,j+1} - \phi_{i,j})}_{D_j^+ \phi_{i,j}} + \min(g_j, 0) \underbrace{(\phi_{i,j} - \phi_{i,j-1})}_{D_j^- \phi_{i,j}} . \quad (2.15) \end{aligned}$$

3. Similarly, the above strategy is also applied for the approximation of $|\nabla\phi|$ at the point (x_i, y_j) . If $\gamma g \geq 0$

$$|\nabla^+\phi|_{i,j} = \left[\max(D_i^-\phi_{i,j}, 0)^2 + \min(D_i^+\phi_{i,j}, 0)^2 + \max(D_j^-\phi_{i,j}, 0)^2 + \min(D_j^+\phi_{i,j}, 0)^2 \right]^{1/2} ;$$

otherwise

$$|\nabla^-\phi|_{i,j} = \left[\min(D_i^-\phi_{i,j}, 0)^2 + \max(D_i^+\phi_{i,j}, 0)^2 + \min(D_j^-\phi_{i,j}, 0)^2 + \max(D_j^+\phi_{i,j}, 0)^2 \right]^{1/2} .$$

Therefore, the third term is approximated by :

$$\gamma g |\nabla\phi| = \max(\gamma g, 0) |\nabla^+\phi|_{i,j} + \min(\gamma g, 0) |\nabla^-\phi|_{i,j} . \quad (2.16)$$

Left side : The left side of Eq. (2.13) can be discretized by using a forward difference scheme for the time variable :

$$\frac{\partial\phi}{\partial t} = \frac{\phi_{i,j}^{n+1} - \phi_{i,j}^n}{\Delta t} , \quad (2.17)$$

Full scheme : Finally, combining the above two, a numerical implementation of Eq. (2.13) is obtained :

$$\begin{aligned} \phi_{i,j}^{n+1} = & \phi_{i,j}^n + \Delta t \left(g^n \frac{\phi_{ii}^n (\phi_j^n)^2 - 2\phi_i^n \phi_j^n \phi_{ij}^n + \phi_{jj}^n (\phi_i^n)^2}{(\phi_i^n)^2 + (\phi_j^n)^2 + \varepsilon} \right. \\ & + \left[\max(g_i^n, 0) D_i^+ \phi_{i,j}^n + \min(g_i^n, 0) D_i^- \phi_{i,j}^n + \max(g_j^n, 0) D_j^+ \phi_{i,j}^n + \min(g_j^n, 0) D_j^- \phi_{i,j}^n \right] \\ & \left. + \max(\gamma g^n, 0) |\nabla^+\phi|_{i,j}^n + \min(\gamma g^n, 0) |\nabla^-\phi|_{i,j}^n \right) . \end{aligned} \quad (2.18)$$

Remark : During the contour evolution, it is essential to periodically re-initialise the function ϕ , so that it remains a signed distance function. This numerical implementation can be easily extended to higher dimensions. Further details can be found in [151, 152].

2.4.4 Advantages and disadvantages

Major advantages of geometric active contour models are briefly summarized :

1. The curve evolution Eq. (2.11) always remains a function as long as $F(\cdot)$ is smooth. Therefore, topological changes, such as breaking, merging or forming sharp corners, are allowed. An illustrative example is show in Fig. 2.3.
2. Finite difference approximations can be used to estimate these spatial and temporal derivatives, because the level set function remains always differentiable.

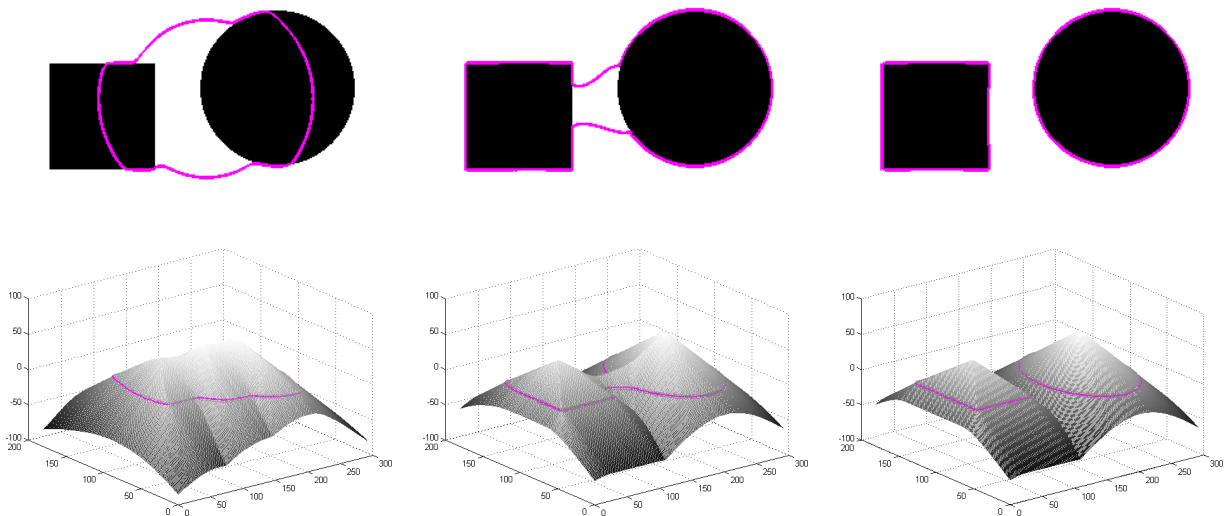


Figure 2.3 – Natural change of topology in the curve evolution when it is represented implicitly by a level set function. The top row shows the curve evolution, and the bottom row shows the associated level set function. The initial contour is the one shown in Fig. 2.2.

3. Geometric characteristics of the curve may be easily computed with the level set function. For example, the unit inward normal to the curve and its curvature are estimated by :

$$\vec{N} = -\frac{\nabla\phi}{|\nabla\phi|} , \quad \kappa = \nabla \cdot \vec{N} = -\nabla \cdot \frac{\nabla\phi}{|\nabla\phi|} .$$

4. The level set function can be easily generalised to higher dimensions. Furthermore, its basic form remains almost the same.

Level set methods also present some disadvantages. One main inconvenient is their large computational costs associated with embedding C into the higher-dimensional function ϕ . However, as we have already mentioned in § 1.2.2, many efficient algorithms have been proposed to speed up its calculation.

2.5 Region-based external energies

As discussed in § 2.2, the edge-based external energy for active contour models is sensitive to initialisation and is known to be less robust to noise. To overcome these problems, region-based external energies, used to model intensity statistics and homogeneity requirements, have been developed in the framework of geometric active contour models. One of the first works on using region-based energies within the level set framework was proposed by Paragios and Deriche [157, 156]. Since then, region-based energies have

become very popular in this context. In the following section, we are going to review some important contributions related to our work. As discussed in § 2.2, the edge-based external energy for active contour models is sensitive to initialisation and are known to be less robust to noise. To overcome these problems, region-based external energies, used to model intensity statistics and homogeneity requirements, have been developed in the framework of geometric active contour models. One of the first works on using region-based energies within the level set framework was by Paragios and Deriche [157, 156]. Since then, region-based energies became very popular in this context. In the following section, we are going to review important contributions related to our work.

2.5.1 Mumford-Shah model

The Mumford-Shah (MS) model [139] was proposed to integrate image denoising with image segmentation. It searches for a piecewise smooth approximation μ and a minimal contour C for the purpose of separating a given image I into non-overlapping regions. This idea can be expressed by the minimisation of :

$$E_{\text{MS}(\mu,C)} = \int_{\Omega} |I - \mu|^2 d\mathbf{x} + \lambda \int_{\Omega-C} |\nabla\mu|^2 d\mathbf{x} + \nu|C| \quad , \quad (2.19)$$

where $\lambda \geq 0$ and $\nu \geq 0$ are constant weights. The first term corresponds to the fidelity term of the general active contour model in Eq. (2.1), as it ensures μ to be similar to I in the L_2 -sense; the second term controls the smoothness of the solution μ , but permits discontinuities across C ; the last term provides the regularisation on the length of C .

The minimisation of the above function is a very difficult problem. Some of the earliest attempts are based on so-called coarse to fine method [19], which minimises E_{MS} by gradually decreasing a continuation parameter, while each level serves as an initialisation for the next level. Ambrosio and Tortorelli have presented a similar technique, by solving a sequence of simpler elliptic variational problems [5]. Recently, a primal-dual projection algorithm has proved the convergence for a convex relaxation of MS functional [165]. Within the level set framework, solutions to simplified versions have been proposed by Tsai et al. [192] and Chan-Vese [193]. The last two works are motivated mainly in solving the segmentation problem.

2.5.2 Segmentation as Bayesian inference

Region-based image segmentation can also be examined under the Bayes' rule. It states that a posterior distribution $p(\mathbf{a}|\mathbf{b})$ over the unknowns \mathbf{a} given the measurements

\mathbf{b} can be obtained by multiplying the likelihood $p(\mathbf{b}|\mathbf{a})$ by the prior distribution $p(\mathbf{a})$. The segmentation can then be obtained in the Bayesian sense by the minimisation of a risk function. Different risk functions lead to different estimators [122]. The maximum a posteriori (MAP) estimator is probably the most popular. Traditionally, Markov random fields (MRF) are used to model the prior distribution [73], and the segmentation problem is solved as a classification problem. Stochastic and deterministic minimisation methods exist [122]. Here, we will be reviewing how this modelling can be used within the level set framework.

Image segmentation can be considered as seeking for an optimal partition, given by the curve C that maximises,

$$p(C|I) = \frac{p(I|C)p(C)}{p(I)} . \quad (2.20)$$

The denominator $p(I)$ is a normalising constant, which is independent of C and usually can be neglected. $p(I|C)$ is a fidelity term, defined by the observed statistics of the current partition. $p(C)$ models our prior knowledge about the desired solution in terms of size, shape or motion, and it acts as a regularisation term on the contour C . For example, a prior constraint on the length of the curve C is commonly modelled as :

$$p(C) = \exp(-\nu|C|) . \quad (2.21)$$

The conditional probability $p(I|C)$, is a likelihood term. It is generally assumed that the observed image intensities at points $\mathbf{x} \in \Omega$ are independent observations of random variables. It is also assumed that they are identically distributed within each of the N regions, obtained by the partition C . Thereby, $p(I|C)$ can be factorized as follows :

$$p(I|C) = \prod_{\mathbf{x} \in \Omega} p(I(\mathbf{x})|C, \mathbf{x})^{d\mathbf{x}} = \prod_r \prod_{\mathbf{x} \in \Omega_r} p(I(\mathbf{x})|\mathbf{x} \in \Omega_r)^{d\mathbf{x}} , \quad (2.22)$$

where $d\mathbf{x}$ is an infinitesimal bin size. The probability density function (pdf) $p(I(\mathbf{x})|\mathbf{x} \in \Omega_r)$ denotes the probability of observed $I(\mathbf{x})$ when Ω_r is a region of interest. The maximisation of the posteriori probability in Eq. (2.20) is equivalent to the minimisation of the anti log-likelihood, which can be rewritten as :

$$E = \underbrace{\sum_r \int_{\Omega_r} -\log p(I(\mathbf{x})|\mathbf{x} \in \Omega_r) d\mathbf{x}}_{\text{anti log-likelihood}} + \underbrace{\nu|C|}_{\text{extra constraint}} . \quad (2.23)$$

The above energy is the basis of many region-based segmentation methods. For instance, if the weight λ of the MS functional in Eq. (2.19) increases, the smoothing constraint

becomes more important. Therefore, when $\lambda \rightarrow \infty$, the approximation μ is no longer a function but collapses into a single value for each separated region. Accordingly, embedding a Gaussian distribution with a fixed standard deviation into Eq. (2.23) can be seen as a simplified version of Eq. (2.19), known as the cartoon limit.

The pdf $p(I(\mathbf{x})|\mathbf{x} \in \Omega_r)$ can be estimated with parametric or non-parametric methods. In the parametric case, such as the Chan-Vese (CV) model [40], the pdf family is assumed to be known. Therefore, one or more parameters should be estimated in order to well model the characteristic of each region in the image. On the other hand, the non-parametric case does not require the image regions to have a particular type of probability distribution. The underlying distribution is estimated from the given image, for example by the Parzen windows technique [183]. In the rest of this chapter, we will consider only a two phase image segmentation problem for both parametric and non-parametric algorithms.

2.5.3 Parametric models

2.5.3.1 The Chan & Vese model

Suppose the noise model of the observed image is additive and follows a Gaussian distribution with zero mean and a variance σ^2 . The conditional probability is as follow :

$$p(I|\Omega_r) = \frac{1}{\sqrt{2\pi}\sigma} \exp\left(-\frac{(I(\mathbf{x}) - \mu_r)^2}{2\sigma^2}\right) ,$$

where μ_r represents the mean value of image intensities inside of the region Ω_r . In the particular case of a binary segmentation, $r = \{i, o\}$, and up to a multiplicative factor and an additive constant term, Eq. (2.23) becomes the formula of the CV model [40], whose external energy function is given by :

$$E_{CV} = \int_{\Omega} (I(\mathbf{x}) - \mu_i)^2 H(\phi(\mathbf{x})) d\mathbf{x} + \int_{\Omega} (I(\mathbf{x}) - \mu_o)^2 H(-\phi(\mathbf{x})) d\mathbf{x} , \quad (2.24)$$

where $H(\cdot)$ is the Heaviside function, and it is defined as :

$$H(\phi) = \begin{cases} 1, & \phi \geq 0 \\ 0, & \phi < 0 \end{cases} .$$

The two constants μ_i and μ_o , are obtained by the minimisation of E_{CV} with respect to the μ_r ² :

$$\hat{\mu}_i = \frac{\int_{\Omega} H(\phi(\mathbf{x})) I(\mathbf{x}) d\mathbf{x}}{A_i} , \quad \hat{\mu}_o = \frac{\int_{\Omega} H(-\phi(\mathbf{x})) I(\mathbf{x}) d\mathbf{x}}{A_o} , \quad (2.25)$$

2. These actually correspond to maximum likelihood estimates.

where A_i is the area of the inside region $\Omega_i : A_i = \int_{\Omega} H(\phi(\mathbf{x})) d\mathbf{x}$, and A_o is the area of the outside region $\Omega_o : A_o = \int_{\Omega} [1 - H(\phi(\mathbf{x}))] d\mathbf{x}$. Keeping μ_i and μ_o fixed and minimising Eq. (2.24) with respect to ϕ , the associated Euler-Lagrange equation for ϕ has been deduced [40]. Parameterizing the descent direction by a time $t \geq 0$, the level set function $\phi(\mathbf{x}, t)$ moves according to :

$$\begin{aligned} \frac{\partial \phi}{\partial t} &= - \frac{\partial E_{\text{CV}}(\phi)}{\partial \phi} \\ &= \delta(\phi) [(I - \widehat{\mu}_o)^2 - (I - \widehat{\mu}_i)^2] , \end{aligned} \quad (2.26)$$

where $\delta(\cdot)$ is the Dirac function. The optimisation of E_{CV} finds its minimum energy when the interior and exterior are respectively best approximated by their means $\widehat{\mu}_i$ and $\widehat{\mu}_o$. Therefore, the CV model is a binary and piecewise constant model.

Remark : In practice a regularised approximation of the Heaviside function is needed. Two popular approximations exist in the literature :

1. The first approximation of the Heaviside function is given [220] :

$$H_{1,\varepsilon}(\phi) = \begin{cases} 0, & \phi < -\varepsilon \\ \frac{1}{2} \left[1 + \frac{\phi}{\varepsilon} + \frac{1}{\pi} \sin\left(\frac{\phi\pi}{\varepsilon}\right) \right] & |\phi| \leq \varepsilon \\ 1, & \phi > \varepsilon \end{cases} , \quad (2.27)$$

which corresponds to the following Dirac function :

$$\delta_{1,\varepsilon}(\phi) = \begin{cases} 0, & |\phi| > \varepsilon \\ \frac{1}{2\varepsilon} \left[1 + \cos\left(\frac{\phi\pi}{\varepsilon}\right) \right] & |\phi| \leq \varepsilon \end{cases} . \quad (2.28)$$

2. The second one, first appeared in [40],

$$H_{2,\varepsilon}(\phi) = \frac{1}{2} \left(1 + \frac{2}{\pi} \arctan\left(\frac{\phi}{\varepsilon}\right) \right) , \quad (2.29)$$

$$\delta_{2,\varepsilon}(\phi) = \frac{1}{\pi} \frac{\varepsilon}{\phi^2 + \varepsilon^2} . \quad (2.30)$$

As $\varepsilon \rightarrow 0$, both $H_{1,\varepsilon}(\phi)$ and $H_{2,\varepsilon}(\phi)$ converge to $H(\phi)$. A difference is that $\delta_{1,\varepsilon}(\phi)$ is defined on the small interval $[-\varepsilon, \varepsilon]$, while $\delta_{2,\varepsilon}(\phi)$ is non zero everywhere. Therefore, in the latter all the level set of ϕ have the potential to be important [152]. When all the levels are updated, not limited in a narrow band, new segmentation region can appear. The re-initialisation to the distance function is not considered to be a good idea [152]. Doing so, the model has tendency to converge to better optimums, but requires more computational effort.

2.5.3.2 The Gaussian Model

Rousson and Deriche [172] supposed that the noise model follows a Gaussian distribution with different variances inside and outside of the contour C . Therefore, the conditional probability of the observed image follows :

$$p(I|\Omega_r) = \frac{1}{\sqrt{2\pi}\sigma_r} \exp\left(-\frac{1}{2} \frac{(I(\mathbf{x}) - \mu_r)^2}{\sigma_r^2}\right) ,$$

which leads to the following external energy function :

$$E_D = \int_{\Omega} H(\phi(\mathbf{x})) \left[\frac{(I(\mathbf{x}) - \mu_i)^2}{2\sigma_i^2} + \frac{1}{2} \log(2\pi\sigma_i^2) \right] d\mathbf{x} + \int_{\Omega} H(-\phi(\mathbf{x})) \left[\frac{(I(\mathbf{x}) - \mu_o)^2}{2\sigma_o^2} + \frac{1}{2} \log(2\pi\sigma_o^2) \right] d\mathbf{x} , \quad (2.31)$$

where the estimates of the means $\hat{\mu}_i$ and $\hat{\mu}_o$ are given in Eq. (2.25). The two variances can be estimated by :

$$\hat{\sigma}_i^2 = \frac{\int_{\Omega} H(\phi(\mathbf{x})) I^2(\mathbf{x}) d\mathbf{x}}{A_i} - \hat{\mu}_i^2 , \quad \hat{\sigma}_o^2 = \frac{\int_{\Omega} H(-\phi(\mathbf{x})) I^2(\mathbf{x}) d\mathbf{x}}{A_o} - \hat{\mu}_o^2 . \quad (2.32)$$

Similar to the CV model, the associated level set flow of Eq. (2.31) is expressed as :

$$\frac{\partial \phi}{\partial t} = \delta(\phi) \left[\log \frac{\hat{\sigma}_o^2}{\hat{\sigma}_i^2} + \frac{(I - \hat{\mu}_o)^2}{\hat{\sigma}_o^2} - \frac{(I - \hat{\mu}_i)^2}{\hat{\sigma}_i^2} \right] . \quad (2.33)$$

Notice that one immediate advantage of the above Gaussian model versus the CV model Eq. (2.24) is the possibility to distinguish regions which have similar mean values but differ by their variances.

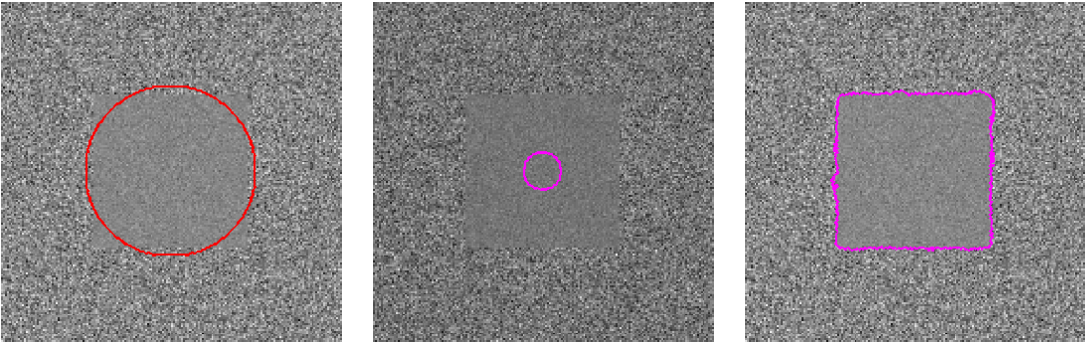


Figure 2.4 – Segmentation example of a noisy image with global region-based methods. From the left to right : the noisy image and initialisation ; segmentation result using the CV model after 500 iterations ; result obtained by the Gaussian model. The image foreground and the background have the same mean but different variances. The red circle is the initial contour, and the magenta curve represents the final segmentation. Hereafter and unless otherwise specified, all the subsequent results use these two colours to label the initial and final contour.

Figure 2.4 shows a segmentation example obtained by the CV model and the Gaussian model. The input image is corrupted by an additive Gaussian noise with two different variances. As expected, the CV model fails to segmented this image. Indeed, as the two regions have very similar mean values, the region-based gradient flow is zero, and the contour C shrinks by the curvature driven regularisation force.

2.5.3.3 The Rayleigh Model

The Rayleigh distribution have been extensively used to model scattering phenomena. For example, Backscattering is the origin of the speckle noise, which characterizes ultrasound imaging with a granular appearance. The speckle is a multiplicative noise, strongly correlated and more importantly, with non-Gaussian statistics. For this reason, several probability density functions were used to model image grey levels statistics in medical echography [141]. Namely the Rayleigh model holds when the speckle noise is fully developed [35, 195]. Such model has been used for the first time, within the levels set framework, by Sarti et al. [175]. The Rayleigh probability distribution function is defined by :

$$p(I|\Omega_r) = \frac{I(\mathbf{x})}{\theta_r^2} \exp\left(-\frac{I(\mathbf{x})^2}{2\theta_r^2}\right) .$$

Then, according to Eq. (2.23), its likelihood is given by :

$$\begin{aligned} l = & \int_{\Omega_i} \log I(\mathbf{x}) d\mathbf{x} - \int_{\Omega_i} I^2(\mathbf{x})/(2\theta_i^2) d\mathbf{x} - A_i \log(\theta_i^2) \\ & + \int_{\Omega_o} \log I(\mathbf{x}) d\mathbf{x} - \int_{\Omega_o} I^2(\mathbf{x})/(2\theta_o^2) d\mathbf{x} - A_o \log(\theta_o^2) . \end{aligned} \quad (2.34)$$

The maximum likelihood estimation (MLE) of the parameters θ_i and θ_o are the values that maximise l . They are obtained by equating to zero the first derivative with respect to θ_i^2 and θ_o^2 :

$$\begin{aligned} \frac{\partial l}{\partial \theta_i^2} &= \int_{\Omega_i} I^2(\mathbf{x})/(2\theta_i^4) d\mathbf{x} - A_i/\theta_i^2 = 0 , \\ \frac{\partial l}{\partial \theta_o^2} &= \int_{\Omega_o} I^2(\mathbf{x})/(2\theta_o^4) d\mathbf{x} - A_o/\theta_o^2 = 0 . \end{aligned}$$

Then the estimation for these parameters are given by :

$$\hat{\theta}_i^2 = \frac{\int_{\Omega} H(\phi(\mathbf{x})) I^2(\mathbf{x}) d\mathbf{x}}{2A_i} , \quad \hat{\theta}_o^2 = \frac{\int_{\Omega} H(-\phi(\mathbf{x})) I^2(\mathbf{x}) d\mathbf{x}}{2A_o} . \quad (2.35)$$

Substitute the estimated parameters $\widehat{\theta}_i^2$ and $\widehat{\theta}_o^2$ back in Eq. (2.34), the likelihood is rewritten as :

$$l = \int_{\Omega} \log I(\mathbf{x}) d\mathbf{x} - (A_i + A_o)(1 - \log 2) - A_i \log \left(\frac{1}{A_i} \int_{\Omega} I(\mathbf{x})^2 H(\phi) d\mathbf{x} \right) - A_o \log \left(\frac{1}{A_o} \int_{\Omega} I(\mathbf{x})^2 H(-\phi) d\mathbf{x} \right) . \quad (2.36)$$

All the terms independent on the partition can be omitted. Consequently, the maximisation of this likelihood can be addressed as the gradient flow with respect to ϕ [175]

$$\begin{aligned} \frac{\partial \phi}{\partial t} = \delta(\phi) & \left[\log \left(\frac{\int_{\Omega} I^2 H(\phi) d\mathbf{x}}{A_i} \right) + \frac{A_i I^2 - \int_{\Omega} I^2 H(\phi) d\mathbf{x}}{\int_{\Omega} I^2 H(\phi) d\mathbf{x}} \right. \\ & \left. - \log \left(\frac{\int_{\Omega} I^2 H(-\phi) d\mathbf{x}}{A_o} \right) - \frac{A_o I^2 - \int_{\Omega} I^2 H(-\phi) d\mathbf{x}}{\int_{\Omega} I^2 H(-\phi) d\mathbf{x}} \right] . \end{aligned} \quad (2.37)$$

More details about this derivation using the Gâteaux derivative are given in Appendix B.

2.5.3.4 The Exponential family

The multi-parameter exponential family is naturally indexed by a k -dimensional real parameter vector $\boldsymbol{\eta}(\boldsymbol{\theta})$ and a k -dimensional natural statistic vector $\mathbf{T}(y)$. It is formally defined as follows (see eg. [202, 111]) :

Definition 2.1. *The family of distributions of a Random Variable $\{p_{\boldsymbol{\eta}}(y) : \boldsymbol{\eta} \in \Theta \subseteq \mathbb{R}^k\}$, is said a k -parameter canonical exponential family, if there exists real-valued functions :*

- $\boldsymbol{\eta}(\boldsymbol{\theta}) = [\eta_1, \dots, \eta_k]^T : \mathbb{R}^k \rightarrow \mathbb{R}$
- $h : \mathbb{R} \rightarrow \mathbb{R}$
- $A : \Theta \rightarrow \mathbb{R}$
- $\mathbf{T} = [T_1, \dots, T_k]^T : \mathbb{R}^k \rightarrow \mathbb{R}$

such that the pdf $p_{\boldsymbol{\eta}}(y)$ may be written as :

$$p_{\boldsymbol{\eta}}(y) = h(y) \exp [\langle \boldsymbol{\eta}(\boldsymbol{\theta}), \mathbf{T}(y) \rangle - A(\boldsymbol{\eta})] , \quad (2.38)$$

where $\langle \cdot, \cdot \rangle$ represents the scalar product in \mathbb{R}^k . The term \mathbf{T} is called the natural sufficient statistic, $\boldsymbol{\eta}$ is the natural parameter vector and the natural parameter space is defined as $\Theta = \{\boldsymbol{\eta} \in \mathbb{R}^k; -\infty < A(\boldsymbol{\eta}) < \infty\}$ with $A(\boldsymbol{\eta}) = \log \int h(y) \exp [\langle \boldsymbol{\eta}(\boldsymbol{\theta}), \mathbf{T}(y) \rangle] dy$.

In the context region-based active contours, Lecellier et al. [111] have recently proposed that the distribution of image features belongs to some exponential families in Eq. (2.38). Thereby, exponential families can cover most noise models encountered in

acquired images, including the previous discussed Gaussian and Rayleigh cases. Table 2.1 provides a synthetic description of some common distributions of exponential families with its parameters $\boldsymbol{\theta}$ and associated functions. Take for example the normal distribution,

$$\begin{aligned} p(I|\mu, \sigma) &= \frac{1}{\sigma\sqrt{2\pi}} \exp\left(-\frac{1}{2} \frac{(I - \mu)^2}{\sigma^2}\right) \\ &= \exp\left(-\frac{1}{2} \log(2\pi\sigma^2) - \frac{I^2}{2\sigma^2} + \frac{\mu I}{\sigma^2} - \frac{\mu^2}{2\sigma^2}\right), \end{aligned}$$

which corresponds to :

$$\begin{aligned} h &= 1, \quad \boldsymbol{\theta} = [\mu, \sigma^2]^T, \quad T(I) = [I, I^2]^T, \quad \boldsymbol{\eta} = \left[\frac{\mu}{\sigma^2}, -\frac{1}{2\sigma^2}\right]^T, \\ A(\boldsymbol{\eta}) &= \frac{1}{2} \left(\frac{\mu^2}{2\sigma^2} + \log(2\pi\sigma^2)\right) = -\frac{1}{2} \left(\frac{\eta_1^2}{2\eta_2} + \log \frac{-\eta_2}{\pi}\right). \end{aligned}$$

There exists different methods to estimate the parameters $\boldsymbol{\eta}$, and the ML estimation is usually preferred when it exists in a close form.

Using the shape derivative tools developed in [92, 10], Lecellier et al. [111] derived general expression for the speed function for the exponential family. When the ML is used for the estimation of the model parameters for the minimisation of the anti log-likelihood in Eq. (2.23), the curve evolution in the direction of ϕ is given by [111] :

$$\frac{\partial E_D}{\partial \phi} = \int_C \left[\log \left(p(y(\mathbf{x})), \hat{\boldsymbol{\eta}}(\Omega) \right) \right] (\phi \cdot \vec{N}) d\mathbf{a}(\mathbf{x}), \quad (2.39)$$

where $d\mathbf{a}(\mathbf{x})$ is the line element. For the common members of exponential families in Table 2.1, their evolution speeds are summarized in Table 2.2. It is important to highlight that Lecellier et al. also showed that, complicated additive terms appear in the evolution speed when the model parameters are estimated by using an alternative method, like the moment method.

| Distribution | $\boldsymbol{\theta}^T$ | $\boldsymbol{\eta}(\boldsymbol{\theta})^T$ | $\mathbf{T}(y)^T$ | $A(\boldsymbol{\eta})$ | Θ |
|--------------|-------------------------|--|-------------------|---|---------------------------------------|
| Normal | (μ, σ^2) | $(\frac{\mu}{\sigma^2}, -\frac{1}{2\sigma^2})$ | (y, y^2) | $-\frac{1}{2} \left(\frac{\eta_1^2}{2\eta_2} + \log \frac{-\eta_2}{\pi} \right)$ | $\mathbb{R} \times] - \infty, 0[$ |
| Gamma | (λ, p) | $(-\lambda, p - 1)$ | $(y, \log y)$ | $-(\eta_2 + 1) \log(-\eta_1) + \log \Gamma(\eta_2 + 1)$ | $] - \infty, 0[\times] 1, +\infty[$ |
| Poisson | μ | $\log \mu$ | y | e^η | \mathbb{R} |
| Exponential | λ | $-\lambda$ | y | $-\log(-\eta)$ | $] - \infty, 0[$ |
| Rayleigh | θ^2 | $-\frac{1}{2\theta^2}$ | y^2 | $-\log(-2\eta)$ | $] - \infty, 0[$ |

Table 2.1 – Common exponential families studied in [111]. See [202] for more examples.

| Distribution | Estimated Parameters | Speed Expressions |
|--------------|----------------------|---|
| Normal | (μ, σ) | $\log \sigma_i + \frac{(I-\mu_i)^2}{2\sigma_i^2} - \log \sigma_o - \frac{(I-\mu_o)^2}{2\sigma_o^2}$ |
| Gamma | (λ, p) | $\log(\Gamma(p_i)\lambda_i^{p_i}) + \frac{I}{\lambda_i} - p_i \log(I)$ $-\log(\Gamma(p_o)\lambda_o^{p_o}) - \frac{I}{\lambda_o} + p_o \log(I)$ |
| Poisson | μ | $-I \log(\mu_i) + \mu_i + \log(\mu_o) + \mu_o$ |
| Exponential | λ | $-\log(\lambda_i) + \lambda_i I + \log(\lambda_o) - \lambda_o I$ |
| Rayleigh | θ^2 | $\frac{I^2}{2\theta_i^2} - \log\left(\frac{I}{\theta_i^2}\right) - \frac{I^2}{2\theta_o^2} + \log\left(\frac{I}{\theta_o^2}\right)$ |

Table 2.2 – Speed expressions of the examples of exponential distributions shown in Table 2.1, when minimising the anti log-likelihood associated energy with the ML parameters estimation [111]. For simplicity, here we use μ to represent its estimator $\hat{\mu}$.

In addition, image-driven energy for region-based segmentation can be modelled as the maximisation of relative entropy, for instance the Kullback-Leibler divergence (KLD), between the pdfs of image intensities in Ω_i and Ω_o :

$$E_D = \int \left(p_i(\mathbf{x}, \boldsymbol{\eta}_i) \log \frac{p_i(\mathbf{x}, \boldsymbol{\eta}_i)}{p_o(\mathbf{x}, \boldsymbol{\eta}_o)} \right) d\mathbf{x} . \quad (2.40)$$

This KLD-based segmentation searches for the configuration that maximises the log-likelihood of the data under their actual model p_i , while minimising the plausibility of the same data under p_o . Therefore, the KLD acts as a region competition criterion. Using the MLE for these parameters $\boldsymbol{\eta}_i$ and $\boldsymbol{\eta}_o$, the evolution speed obtained by the Eulerian derivative of the above energy is given by [111] :

$$\frac{\partial E_D}{\partial \phi} = - \left\langle \nabla_\phi \overline{\mathbf{T}(y)}_i, \hat{\boldsymbol{\eta}}_i - \hat{\boldsymbol{\eta}}_o \right\rangle + \left\langle \nabla_\phi \overline{\mathbf{T}(y)}_o, \frac{\nabla A(\hat{\boldsymbol{\eta}}_o) - \nabla A(\hat{\boldsymbol{\eta}}_i)}{A(\ddot{\boldsymbol{\eta}}_o)} \right\rangle , \quad (2.41)$$

where $\overline{\mathbf{T}(y)}$ is the mean of $\mathbf{T}(y)$, and \ddot{A} is the Hessian matrix of A calculated as $\ddot{A}(\mathbf{x}) = \frac{\partial^2 A}{\partial \boldsymbol{\eta}_1 \partial \boldsymbol{\eta}_2}$.

The use of this parametrisation of the exponential family appears to be a flexible tool. The work of Lecellier et al. [111] can be used to solve difficult segmentation problems which involves various noise models in the external energy. The reader is referred to [111, 112] for further details.

2.5.3.5 Maximal discrepancy methods

The means separation algorithm, proposed by Yezzi et al. [213], relies on the assumption that foreground and background regions should have maximally different mean

intensities. It uses the distance between μ_i and μ_o to measure how well the curve C has separated the foreground from the background. Mathematically, the data energy term is given by :

$$E_D = -\frac{1}{2}(\mu_i - \mu_o)^2 . \quad (2.42)$$

The mean values are approximated by their ML estimates given in Eq. (2.25). Then, the gradient flow of E_D can be expressed by :

$$\frac{\partial \phi}{\partial t} = (\hat{\mu}_i - \hat{\mu}_o) \left(\frac{I - \hat{\mu}_i}{A_i} + \frac{I - \hat{\mu}_o}{A_o} \right) |\nabla \phi| . \quad (2.43)$$

There is no restriction on how well the regions are modelled by $\hat{\mu}_i$ and $\hat{\mu}_o$. In other words, the above model do not assume a piecewise constant image model as the CV model. Eq. (2.42) can be further generalised by using other statistics. For instance when the image to segment has regions with identical means but different variances, we can use the following alternative energy functional [213] :

$$E_D = -\frac{1}{2}(\sigma_i^2 - \sigma_o^2)^2 . \quad (2.44)$$

Similarly, the evolution of this variances separation algorithm via the gradient flow is :

$$\frac{\partial \phi}{\partial t} = (\hat{\sigma}_i^2 - \hat{\sigma}_o^2) \left[\frac{(I - \hat{\mu}_i)^2 - \hat{\sigma}_i^2}{A_i} + \frac{(I - \hat{\mu}_o)^2 - \hat{\sigma}_o^2}{A_o} \right] |\nabla \phi| . \quad (2.45)$$

Although the underling assumption on the image model are less restrictive for the above two energies, in comparison to the CV model, they have not yet attracted more attention.

2.5.4 Non-parametric models

In the non-parametric region-based segmentation, the chosen image characteristics, commonly pixel intensities, are assumed to be independent identically distributed in each region. The foreground and background are distinct in the sense that they have different pdfs of the observed image intensities over the sub-domains Ω_i and Ω_o :

$$\{I(\mathbf{x})|\mathbf{x} \in \Omega_i\} \sim p_i , \quad \{I(\mathbf{x})|\mathbf{x} \in \Omega_o\} \sim p_o .$$

Given a level set function ϕ , non-parametric approaches define a kernel-based estimation of the above pdfs :

$$p_r(z|\phi(\mathbf{x})) = \frac{\int_{\Omega_r} K_\rho(z - I(\mathbf{x})) d\mathbf{x}}{A_r} , \quad r = \{i, o\} , \quad (2.46)$$

where $K_\rho(\cdot)$ is a tonal kernel which should satisfy the following properties :

- $K_\rho(-a) = K_\rho(a)$;
- $K_\rho(a) \geq K_\rho(b)$, if $|a| < |b|$. $\lim_{|a| \rightarrow \infty} K_\rho(a) = 0$;
- $\int K_\rho(\mathbf{x}) d\mathbf{x} = 1$.

One typical choice of $K_\rho(\cdot)$ is the normalised Gaussian kernel. Based on the above defined estimator of the pdfs, several data energies derived from information theory have been derived in the literature to solve a segmentation problem.

The core idea is to maximise the discrepancy between the distributions inside and outside of the current segmentation [67, 102, 133, 11]. In other words, it assumes the optimal contour should minimise the mutual information between these subsets. A number of measures can be used to define the distance between distributions [50]. For example, the Bhattacharyya distance between two probability densities is defined as $-\log B$, where B is the Bhattacharyya coefficient that measures the amount of overlap, given by :

$$B(p_i, p_o) = \int_z \sqrt{p_i(z|\phi(\mathbf{x})) p_o(z|\phi(\mathbf{x}))} dz , \quad (2.47)$$

where p_i and p_o are estimated by Eq. (2.46). The values of $B(p_i, p_o)$ are always confined within the interval $[0, 1]$, where 0 indicates no overlap and 1 means a perfect match. The rest of this subsection will give two examples of the non-parametric active contour models using the Bhattacharyya coefficient.

2.5.4.1 Histogram separation method

In the histogram separation active contour, the optimal segmentation is achieved when the Bhattacharyya distance between the pdfs is the maximum, which equivalent to minimise the corresponding Bhattacharyya coefficient described in Eq. (2.47). Therefore, the data-driven energy functional is defined as $E_D = B(p_i, p_o)$ in [133]. In order to contrive a numerical scheme to minimise this external energy, its first variation with respect to ϕ should be computed :

$$\frac{\partial E_D}{\partial \phi(\mathbf{x})} = \frac{1}{2} \int_z \left(\frac{\partial p_i(z|\phi(\mathbf{x}))}{\partial \phi(\mathbf{x})} \sqrt{\frac{p_o(z|\phi(\mathbf{x}))}{p_i(z|\phi(\mathbf{x}))}} + \frac{\partial p_o(z|\phi(\mathbf{x}))}{\partial \phi(\mathbf{x})} \sqrt{\frac{p_i(z|\phi(\mathbf{x}))}{p_o(z|\phi(\mathbf{x}))}} \right) dz , \quad (2.48)$$

$$\text{where } \frac{\partial p_r(z|\phi(\mathbf{x}))}{\partial \phi(\mathbf{x})} = \delta(\phi(\mathbf{x})) \left(\frac{p_r(z|\phi(\mathbf{x})) - K_\rho(z - I(\mathbf{x}))}{A_r} \right) . \quad (2.49)$$

Accordingly, by combination of the above two equations, the gradient flow of the level set function that minimises the above external energy is given by [133] :

$$\begin{aligned} \frac{\partial \phi}{\partial t} &= -\frac{\partial E_D}{\partial \phi} , \\ &= \frac{1}{2} \delta(\phi(\mathbf{x})) \left[B(p_i, p_o)(A_o^{-1} - A_i^{-1}) + \int K_\rho(z - I(\mathbf{x})) L(z|\phi(\mathbf{x})) dz \right] , \end{aligned} \quad (2.50)$$

$$\text{where } L(z|\phi(\mathbf{x})) = \frac{1}{A_i} \sqrt{\frac{p_o(z|\phi(\mathbf{x}))}{p_i(z|\phi(\mathbf{x}))}} - \frac{1}{A_o} \sqrt{\frac{p_i(z|\phi(\mathbf{x}))}{p_o(z|\phi(\mathbf{x}))}} .$$

The first term in the above speed function is independent of the spatial position \mathbf{x} , and it results in increasing or decreasing the mean value of ϕ by a constant amount. The second term can be viewed as a smoothed version of $L(z|\phi(\mathbf{x}))$, which is defined as the difference between the square roots of the likelihood ratios p_i/p_o and p_o/p_i weighted by their corresponding areas.

2.5.4.2 Statistical overlap with a prior

An equivalent idea, as the histogram separation methods, has been used to introduce prior information on the pdf(s) of the object(s) of interest. An interesting example was proposed by Ayed et al. [11], who introduced a statistical overlap constraint. This constraint imposes that the desired segmentation is optimal when the region's pdf has an overlap statistically similar to learned prior. Suppose the pdf of Ω_i is characterized by a known model $M_i(z)$. Ayed et al. considered to measure the overlap between the sample pdf outside the curve and the model distribution of the object (inside) using the Bhattacharyya coefficient $B(M_i(z), p_o(z|\phi(\mathbf{x})))$. Then Ayed et al. have proposed to evaluate the conformity of B to a learned Gaussian model :

$$E_D = \sqrt{-\log \mathcal{N}(B(M_i, p_o), \mu_B, \sigma_B^2)} . \quad (2.51)$$

Notice that μ_B and σ_B here are not the statistics of certain sub-regions. They are learned from a set of relevant training images. In the particular case of $\mu_B = 0$, the overlap between M_i and p_o should be minimal. Distributions other than the Gaussian model can be employed to model $B(M_i(z), p_o(z|\phi(\mathbf{x})))$.

The minimisation of E_D with respect to ϕ is given by the following PDE [11] :

$$\frac{\partial E_D}{\partial \phi} = -\frac{B(M_i, p_o) - \mu_B}{2\sigma_B^2 E_D} \frac{\partial B(M_i, p_o)}{\partial \phi} , \quad (2.52)$$

$$\text{where } \frac{\partial B(M_i, p_o)}{\partial C} = \frac{1}{2} \sqrt{\frac{M_i}{p_o}} \frac{\partial p_o}{\partial \phi} . \quad (2.53)$$

By embedding Eq. (2.49) into the above equations, the curve evolution is given by the following gradient flow [11] :

$$\frac{\partial \phi}{\partial t} = \delta(\phi(\mathbf{x})) \underbrace{\frac{B - \mu_B}{2\sigma_B^2 E_D}}_{\text{oc}} \underbrace{\frac{1}{2A_o} \left(\int K_\rho(z - I(C)) \sqrt{M_i/p_o} dz - B \right)}_{\text{flow optimising B}}, \quad (2.54)$$

where we have denoted by ‘oc’ the overlap constraint speed coefficient. The learned mean μ_B decides the sign of the overlap constraint influence, which keeps B close to its most likely value μ_B . For example, if the overlap B is superior to μ_B , this coefficient is negative and leads to a curve evolution which decreases B . The learned variance σ_B^2 affects the weight of this overlap constraint. A small σ_B means that μ_B is a reliable estimation, such that it gives a higher weight to the overlap constraint and less importance to the other functional terms (not shown here) and vice-versa.

2.6 Conclusion

In this chapter, after a brief introduction of the principle of classical active contour models, we have introduced geometric active contours and their implicit representation using the levels set tool. We focused on the latter, since they can naturally handle topological changes and can be easily generalised to higher dimension. Then, within this framework, we introduced typical region-based external energies, parametric and non-parametric, that are commonly used in segmentation nowadays.

It is well known that active contours driven by region-data terms are quite robust to initialisations. We have also seen that region-based tools offer a larger choice to model the statistical nature of the observed image intensities. It is important, however, to highlight that they are build on the assumption that each region should be statistically homogeneous. In other words, that the random observed intensities within a region are identically distributed and follow a certain pdf. Therefore, the performances of parametric models can be severely affected when the assumed model is not correct ; or when the identically distributed assumption does not hold. In the next chapter, we will further concentrate on parametric region-based segmentation algorithms, and particularly on the ones based on local image statistics.

Local region-based methods

Chapter summary

This chapter studies the principles of using local region statistics to build the image-driven energy for active contour models. Several typical local region-based segmentation methods will be presented and analysed. Finally, we will introduce two general paradigms for region-based external energies, which can include most existing global and local models as special cases.

Contents

| | |
|---|-----------|
| 3.1 Introduction | 36 |
| 3.2 Brox and Cremers model | 39 |
| 3.3 Local intensity fitting model | 43 |
| 3.4 Local intensity fitting with bias correction | 45 |
| 3.5 General framework for region-based methods | 48 |
| 3.5.1 Lankton and Tannenbaum model | 48 |
| 3.5.2 Localised Bayesian interpretation | 49 |
| 3.6 Conclusion | 51 |

3.1 Introduction

Region-based external energies in active contours exhibit a considerable improvement in image segmentation than edge-based ones [52]. Indeed, they are known to be more robust and efficient in handling image noise and weak boundaries. The first generation of region-based methods are global models. They are bound by a homogeneity assumption, roughly speaking a constant intensity is required, for each object in the image. This assumption, however, does not generally hold for ultrasound images, where inhomogeneities are generally inevitable. Figure 3.1 demonstrates some images with inhomogeneous characteristics. In these cases, the object to be segmented cannot be distinguished appropriately in terms of global image statistics. Therefore, active contours driven by global region-based forces lead inevitably to erroneous segmentation.

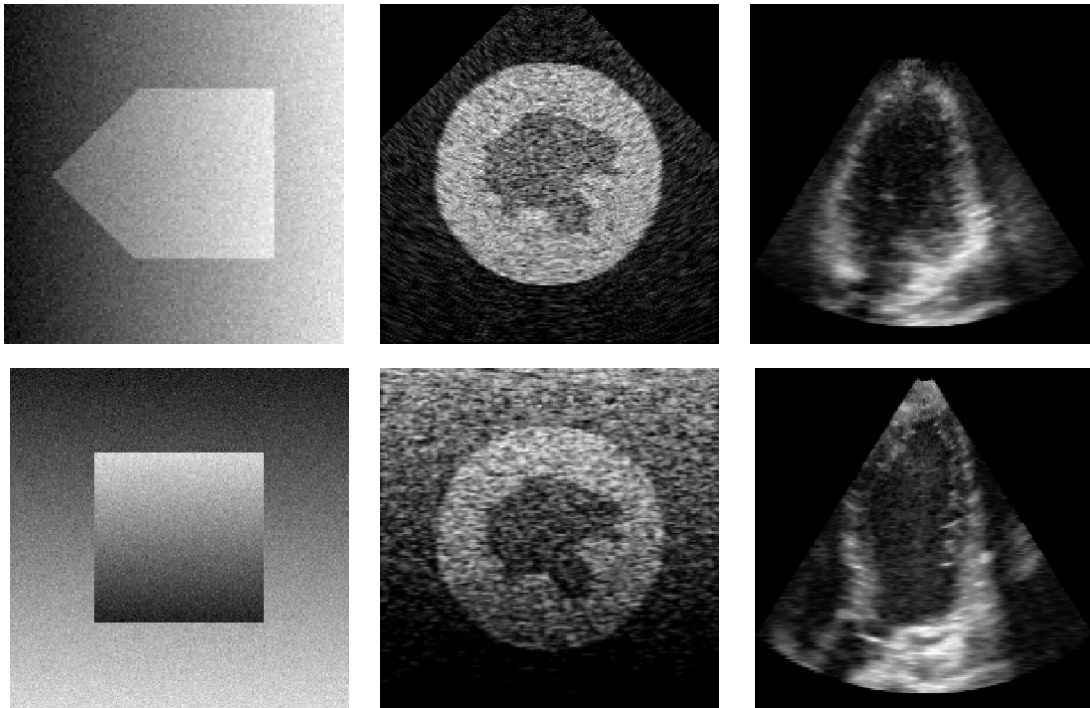


Figure 3.1 – Examples of images with intensity inhomogeneities. From left to right : synthetic images corrupted by gradual intensity changes and by an additive Gaussian noise ; realistic ultrasound simulations³ ; echocardiographic images with the presence of attenuation, shadows and signal dropout⁴.

3. See § 5.4.1 for these simulations.

4. We would like to thank Professor Alison Noble (BioMedIA Laboratory, University of Oxford) for providing the real ultrasound data.

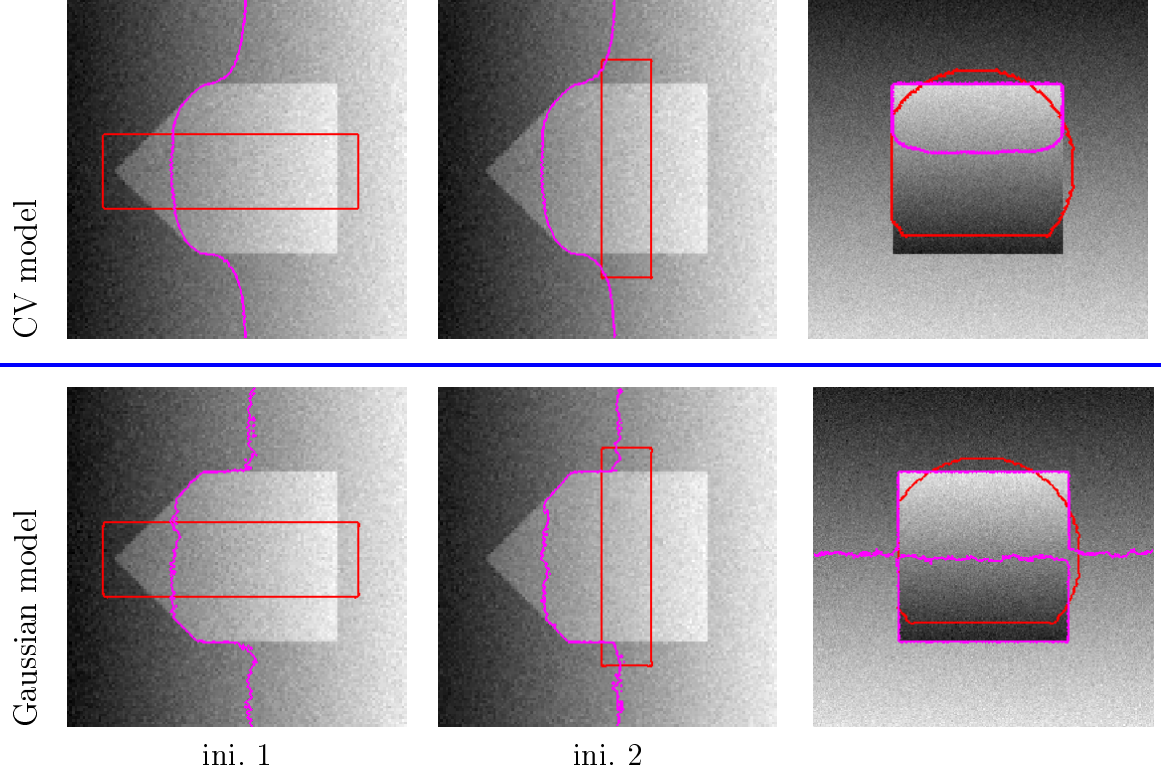


Figure 3.2 – Segmentation examples of synthetic images with inhomogeneities using global region-based methods⁵. Two initialisations are tested for the first image. Top : results of the CV model; bottom : the Gaussian model.

In order to support our claim and to show the limitations of global models, we tested the CV model Eq. (2.24) and the Gaussian model Eq. (2.31) on two synthetic images shown in Fig. 3.1. Their results are shown in Fig. 3.2. Analysing segmentations of the first image, we notice that similar partitions are obtained even with different initialisations for both models. These results are in favour of supporting that region-based methods are robust to initialisation, but also demonstrating that global external energies are not appropriate for images with strong intensity inhomogeneities.

In order to accurately segment these inhomogeneous objects, some work, utilising local image statistics within the level set framework, has been recently carried out. For these methods, an appropriate spatial window K should be introduced in order to define the locality. Suppose \mathbf{x} and \mathbf{y} to be two distinct points in image domain Ω . The local region can be defined, for example, by the following kernel [109] :

$$K(\mathbf{x}, \mathbf{y}) = \begin{cases} 1 & \|\mathbf{x} - \mathbf{y}\| < h \\ 0 & \text{otherwise} \end{cases} . \quad (3.1)$$

⁵. Unless otherwise specified, the experiments in this chapter use the length term $\nu|C|$ as the internal energy, and use the same weight $\nu = 1$.

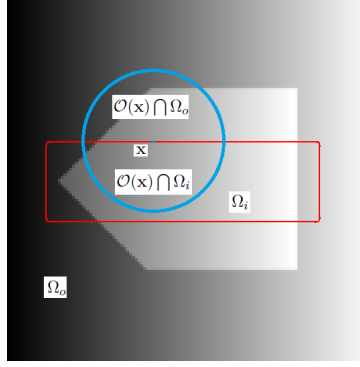


Figure 3.3 – Graphical representation of local region. The locality of point $\mathbf{x} \in C$ is defined by the interior of the blue circle. All points within this neighbourhood are classified as local interiors $\mathcal{O}(\mathbf{x}) \cap \Omega_i$ and local exteriors $\mathcal{O}(\mathbf{x}) \cap \Omega_o$.

A Gaussian kernel with a scaling parameter σ_p is often chosen to defined this locality, and for efficiency reasons, it can be truncated outside the interval $h = 3\sigma_p$ [120, 32] :

$$K(\mathbf{x}, \mathbf{y}) = \begin{cases} \exp\left(-\frac{(\mathbf{x}-\mathbf{y})^2}{2\sigma_p^2}\right) & \|\mathbf{x} - \mathbf{y}\| < h \\ 0 & \text{otherwise} \end{cases} . \quad (3.2)$$

It is not necessary to normalise the above function, because this will be done implicitly in later procedures.

In the following, the local region, at a given point \mathbf{x} along the curve C , will be denoted by $\mathcal{O}(\mathbf{x}) = \{\mathbf{y} : \|\mathbf{x} - \mathbf{y}\| < h\}$. It is represented by the area inside of the blue circle shown in Fig. 3.3. Then, the local neighbourhood of \mathbf{x} is divided into a local interior and exterior by the curve C , as a result of the intersections between $\mathcal{O}(\mathbf{x})$ and Ω_r with $r = \{i, o\}$. Thereby, global image statistics, such as μ_r and σ_r , become local and pixel-dependent : $\mu_r(\mathbf{x})$ and $\sigma_r(\mathbf{x})$. Similar to the ML estimates given previously in Eq. (2.25) and Eq. (2.32) for the global models, estimation of these local image statistics can be achieve by :

$$\hat{\mu}_r(\mathbf{x}) = \frac{\int_{\Omega_r} K(\mathbf{x} - \zeta) I(\zeta) d\zeta}{\int_{\Omega_r} K(\mathbf{x} - \zeta) d\zeta} , \quad (3.3)$$

$$\hat{\sigma}_r^2(\mathbf{x}) = \frac{\int_{\Omega_r} K(\mathbf{x} - \zeta) |I(\zeta) - \hat{\mu}_r(\mathbf{x})|^2 d\zeta}{\int_{\Omega_r} K(\mathbf{x} - \zeta) d\zeta} . \quad (3.4)$$

The above formulas can be seen as normalised convolutions of image features with the kernel $K(\cdot)$.

In this chapter, we will focus on analysing some important contributions on local region-based segmentation methods. We will start with the work of Brox and Cremers [31, 32]. The authors derived a straightforward local Gaussian model from an interpretation of

the piecewise smooth MS functional. We then review Li's and colleagues' contributions. Data fitting energies, namely a binary fitting and a Gaussian fitting, to locally approximate the observed image intensities have been proposed in [120, 196]. Based on a local intensity clustering property, a segmentation method with a bias field correction is introduced in [119]. We will also consider the region-based framework proposed by Lankton and Tannenbaum [109], which allows to reformulate a given global external energy in a local way. Finally, we conclude the data-driven energies by a general Bayesian interpretation with two local kernels.

3.2 Brox and Cremers model

The idea of incorporating local region statistics in a variational framework begins with the work of Brox and Cremers [31]. They have derived the Euler-Lagrange equation of a local Gaussian model. The data fidelity term of Brox and Cremers's (BC) model is expressed by [31, 32] :

$$E_{\text{BC}} = \sum_r \int_{\Omega} H_r(\phi) \left[\frac{(I(\mathbf{x}) - \mu_r(\mathbf{x}))^2}{2\sigma_r^2(\mathbf{x})} + \frac{1}{2} \log(\sigma_r^2(\mathbf{x})) \right] d\mathbf{x} , \quad (3.5)$$

where the Heaviside function $H_r(\phi)$ defines the region Ω_r . The data-driven energy of a point \mathbf{x} is characterized by its local mean $\mu_r(\mathbf{x})$ and local variance $\sigma_r^2(\mathbf{x})$.

The exact shape gradient of E_{BC} with respect of the contour can be computed by the Gâteaux derivative, where the usual implementation is a coordinate descent. For simplicity, the minimisation of the external energy for one region Ω_i can be expressed by [31] :

$$\frac{\partial E_{\text{BC}}(\Omega_i)}{\partial \phi} = \delta(\phi(\mathbf{x})) \left[\frac{(I(\mathbf{x}) - \widehat{\mu}_i(\mathbf{x}))^2}{2\widehat{\sigma}_i^2(\mathbf{x})} + \log \widehat{\sigma}_i(\mathbf{x}) - \frac{1}{2} (I^2(\mathbf{x})F_4(\mathbf{x}) + I(\mathbf{x})F_5(\mathbf{x}) + F_6(\mathbf{x})) \right] , \quad (3.6)$$

with the following abbreviations :

$$\begin{aligned} F_1(\mathbf{x}) &= (K * H_i(\phi))(\mathbf{x}) , \\ F_2(\mathbf{x}) &= [K * (H_i(\phi)I)](\mathbf{x}) \quad \rightarrow \quad \widehat{\mu}_i(\mathbf{x}) = \frac{F_2(\mathbf{x})}{F_1(\mathbf{x})} , \\ F_3(\mathbf{x}) &= [K * (H_i(\phi)I^2)](\mathbf{x}) \quad \rightarrow \quad \widehat{\sigma}_i^2(\mathbf{x}) = \frac{F_3(\mathbf{x})}{F_1(\mathbf{x})} - \widehat{\mu}_i^2(\mathbf{x}) , \end{aligned}$$

$$\begin{aligned}
F_4(\mathbf{x}) &= \left[\bar{K} * \frac{H_i(\phi)(I - \hat{\mu}_i)^2 - \hat{\sigma}_i^2}{\hat{\sigma}_i^4 F_1} \right] (\mathbf{x}) , \\
F_5(\mathbf{x}) &= \left\{ \bar{K} * \frac{H_i(\phi) [2I\hat{\sigma}_i^2 - 2\hat{\mu}_i(I - \mu_i)^2]}{\sigma_r^4 F_1} \right\} (\mathbf{x}) , \\
F_6(\mathbf{x}) &= \left\{ \bar{K} * \frac{H_i(\phi) \left[\hat{\sigma}_i^2 \left(\frac{F_3}{F_1} - 2I\hat{\mu}_r \right) - (I - \hat{\mu}_i)^2 (\hat{\sigma}_i^2 - \hat{\mu}_i^2) \right]}{\hat{\sigma}_i^4 F_1} \right\} (\mathbf{x}) .
\end{aligned}$$

Here, \bar{K} is the mirrored kernel of K and $*$ is a convolution operation. The estimation of $\mu_r(\mathbf{x})$ and $\sigma_r(\mathbf{x})$ in Eq. (3.3)(3.4) now are function of F_1, F_2, F_3 . More details on the derivation of the above shape gradient equations can be found in Appendix A.2 and [31].

In order to define the locality, the BC model uses an isotropic Gaussian kernel with a standard deviation σ_p . This choice of local kernel leads to a fast implementation using recursive filtering. This has the advantage of a computational complexity that is independent from the choice of the scale of the local spatial kernel. Notice that, the convolutions F_1, F_2, F_3 are already needed when we use the coordinate descent. The remaining terms F_4, F_5, F_6 take into account the dependency of the means and standard deviations on ϕ . Figure 3.4 demonstrates that, normally, these additional terms are important only when

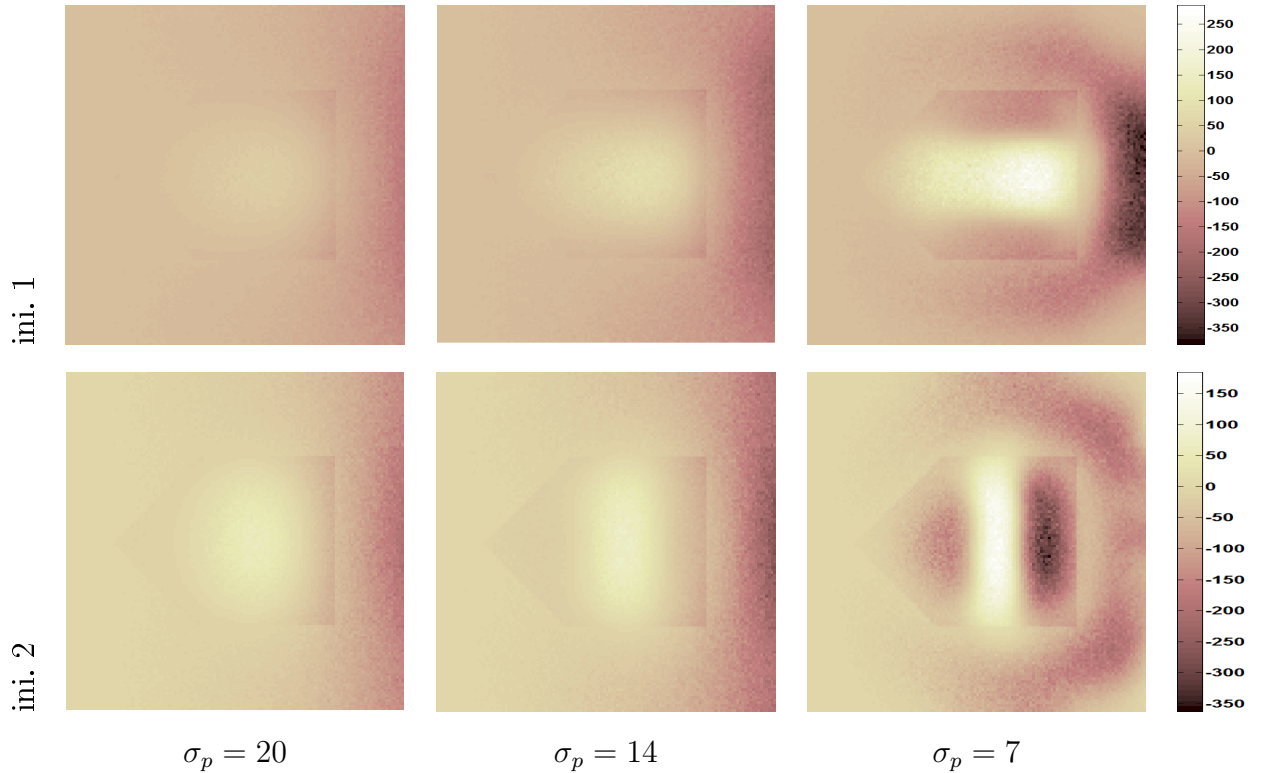


Figure 3.4 – Influence of σ_p , the scale of the spatial kernel, on the terms $(I^2 F_4 + I F_5 + F_6)$ in Eq. (3.6). We illustrate here the additional term of the seep function at the initial contours shown in Fig. 3.2. Note that they become important when σ_p decreases.

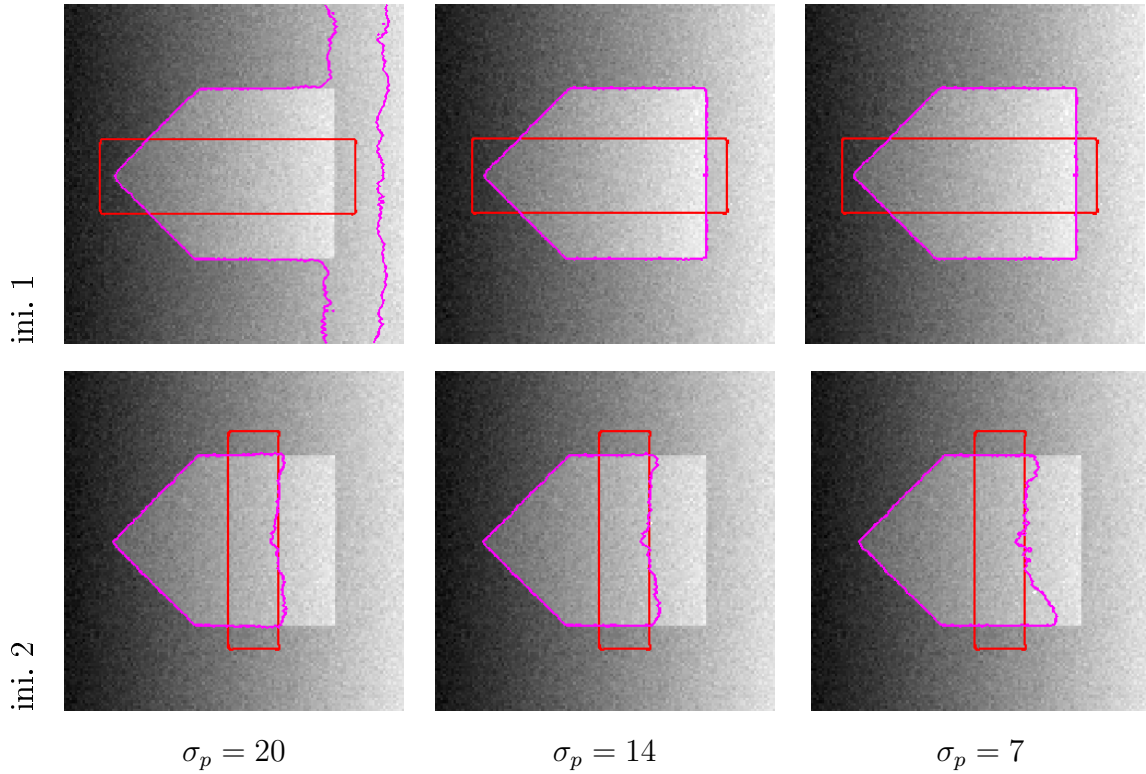


Figure 3.5 – Segmentation examples with the local BC model. The figure illustrates the importance of the choice of an appropriate size for the local kernel. For ini. 1, the optimal scale should be between $\sigma_p = 14$ and 7; while for ini. 2, none of these scales led to an acceptable result.

the local scale σ_p is small, and they could be ignored in the evolution function.

As exhibited in Fig. 3.5, we use the BC model to segment the same test image for the global models in Fig. 3.2. Three different scales are examined here, aiming at studying the influence of the kernel scale σ_p in this local method. As expected, the BC model is more appropriate for the segmentation of images with inhomogeneities than global ones. For the first initialisation, two of the three results, obtained with the smaller kernel sizes, are much better than the global ones. Also notice that if an appropriate scale is chosen, here between $\sigma_p = 14$ and 7 for the first initialisation, the BC model is able to distinguish the parts with a very low contrast between the background and the foreground. For the second row in Fig. 3.2, however, all three scales are unable to lead to a good result. Therefore, Figure 3.5 suggests that the segmentation achieved by the BC model is rather sensitive to initialisations and to the choice of the size of the local kernel.

Remarks :

1. According to [142] the outcomes of some linear filters are exact minimisers of certain energy functional with an infinite sum of penalised terms of arbitrarily high order.

For a spatial position $\mathbf{x} = (x, y)^T$, Brox and Cremers [32] have proposed that the convolution result for estimating local image statistics in Eq. (3.3) equals to finding the minimisation of the following energy function :

$$E(\mu_r) = \int_{\Omega_r} \left[(I(\mathbf{x}) - \mu_r(\mathbf{x}))^2 + \sum_{k=1}^{\infty} \frac{\lambda^k}{k!} \sum_{k_1+k_2=k} \left(\frac{\partial^k \mu_r(\mathbf{x})}{\partial x^{k_1} \partial y^{k_2}} \right)^2 \right] d\mathbf{x} . \quad (3.7)$$

Neglecting all penalised terms of order $k > 1$, the energy with some boundary constraints, for example the regularisation on the length of C , can be written as :

$$\begin{aligned} E &= \sum_r E(\mu_r) + \nu|C| , \\ &\approx \sum_r \int_{\Omega_r} [(I(\mathbf{x}) - \mu_r(\mathbf{x}))^2 + \lambda|\nabla\mu_r(\mathbf{x})|^2] d\mathbf{x} + \nu|C| , \end{aligned} \quad (3.8)$$

which corresponds exactly to the MS functional given in Eq. (2.19). The main effect of ignoring the higher order terms is that, the local mean function $\mu_r(\mathbf{x})$ in Eq. (3.8) is less smooth than the exact minimiser of Eq. (3.7). This impact can be further reduced by choosing a slightly larger weight λ for the first-order approximated energy Eq. (3.7) than the one used in the regularisation term containing the infinite sum of penalisations in Eq. (3.8) [32] .

2. The Bayesian model given in Eq. (2.23) can be directly generalised to local cases. For example, by substituting the conditional probability $p(I|C) \sim \mathcal{N}(\mu_r(\mathbf{x}), \sigma_r^2(\mathbf{x}))$ with a local Gaussian probability density, we obtain the local version of the Gaussian model and CV model expressed by :

$$\begin{aligned} E &= \sum_r \int_{\Omega_r} \left[\frac{(I(\mathbf{x}) - \mu_r(\mathbf{x}))^2}{2\sigma_r^2(\mathbf{x})} + \frac{1}{2} \log(\sigma_r^2(\mathbf{x})) \right] d\mathbf{x} + \nu|C| \\ E &= \sum_r \int_{\Omega_r} (I(\mathbf{x}) - \mu_r(\mathbf{x}))^2 d\mathbf{x} + \nu|C| + \text{const} , \quad \text{for } \sigma_r^2 = 0.5 . \end{aligned}$$

Consequently, this Bayesian a-posteriori maximisation based on local Gaussian model is exactly the BC model in Eq. (3.5).

3. Brox and Cremers [31] have also proposed a general solution for non-parametric local models in Eq. (2.23), whose Gâteaux derivative is as follows :

$$\begin{aligned} \frac{\partial E(\phi)}{\partial \phi} &= \delta(\phi(\mathbf{x})) \log p(I(\mathbf{x}), \mathbf{x}) \\ &+ \delta(\phi(\mathbf{x})) \int_{\Omega} \frac{K(\mathbf{y} - \mathbf{x}) H_r(\phi(\mathbf{y})) (K_{\rho}(I(\mathbf{y}) - I(\mathbf{x})) - p(I(\mathbf{y}), \mathbf{y}))}{p(I(\mathbf{y}), \mathbf{y}) \int_{\Omega} K(\mathbf{y} - \mathbf{z}) H_r(\phi(\mathbf{z})) d\mathbf{z}} d\mathbf{y} . \end{aligned}$$

Notice here the locality K with the scale σ_p is different from the tonal kernel in the Parzen estimator $K_\rho(\cdot)$. By using estimated intensity histograms, this evolution function can be implemented through convolutions, which are similar to the parametric external model shown in Eq. (3.6).

3.3 Local intensity fitting model

Li et al. [120] have proposed a local data fitting energy for the purpose of handling intensity inhomogeneity. For a given point $\mathbf{x} \in \Omega$, its fitting function locally approximates the image intensity [120] :

$$E_{\text{fit}}(\mathbf{x}) = \sum_r \int_{\Omega_r} K_{\sigma_e}(\mathbf{x} - \mathbf{y}) |I(\mathbf{y}) - \mu_r(\mathbf{x})|^2 d\mathbf{y} , \quad (3.9)$$

where the local kernel K_{σ_e} satisfies Eq. (3.2). Due to the contribution of this assigned coefficient K_{σ_e} , intensities $I(\mathbf{y})$ are effectively involved in the above energy within a local region $\mathcal{O}(\mathbf{x})$. Therefore, $E_{\text{fit}}(\mathbf{x})$ can be seen as a weighted mean square error (MSE) of the approximation of the image intensities for each region Ω_r .

In order to obtain the segmentation, $E_{\text{fit}}(\mathbf{x})$ is minimised for all pixels \mathbf{x} in the whole image domain Ω . Hence, the external energy using this intensity model is defined as the following double integral functional [120] :

$$E_{\text{Li}} = \int_{\Omega} E_{\text{fit}}(\mathbf{x}) d\mathbf{x} = \int_{\Omega} \left(\sum_r \int_{\Omega_r} K_{\sigma_e}(\mathbf{x} - \mathbf{y}) |I(\mathbf{y}) - \mu_r(\mathbf{x})|^2 d\mathbf{y} \right) d\mathbf{x} . \quad (3.10)$$

For a binary segmentation, the above function corresponds to the global fitting energy in the CV model. Wang et al. [196] have extended Eq. (3.10) by taking the local variances into account. Therefore

$$E_{\text{Wang}} = \int_{\Omega} \left\{ \sum_r \int_{\Omega_r} K_{\sigma_e}(\mathbf{x} - \mathbf{y}) \left[\frac{|I(\mathbf{y}) - \mu_r(\mathbf{x})|^2}{2\sigma_r^2(\mathbf{x})} + \frac{1}{2} \log(\sigma_r^2(\mathbf{x})) \right] d\mathbf{y} \right\} d\mathbf{x} \quad (3.11)$$

is used to fit the local Gaussian distribution. By minimising the above energy with respect to $\mu_r(\mathbf{x})$ and $\sigma_r(\mathbf{x})$, we obtain the same estimation of local model parameters given in Eqs. (3.3) and (3.4), with $\sigma_e = \sigma_p$. Within the level set framework, minimisation of Eq. (3.11) can be achieved by the following gradient descent equation [196] :

$$\frac{\partial E_{\text{Wang}}(\phi)}{\partial t} = - \sum_r \delta(\phi) \int_{\Omega_r} K_{\sigma_e}(\mathbf{y} - \mathbf{x}) \left[\frac{(I(\mathbf{x}) - \hat{\mu}_r(\mathbf{y}))^2}{2\hat{\sigma}_r^2(\mathbf{y})} + \log(\hat{\sigma}_r(\mathbf{y})) \right] d\mathbf{y} . \quad (3.12)$$

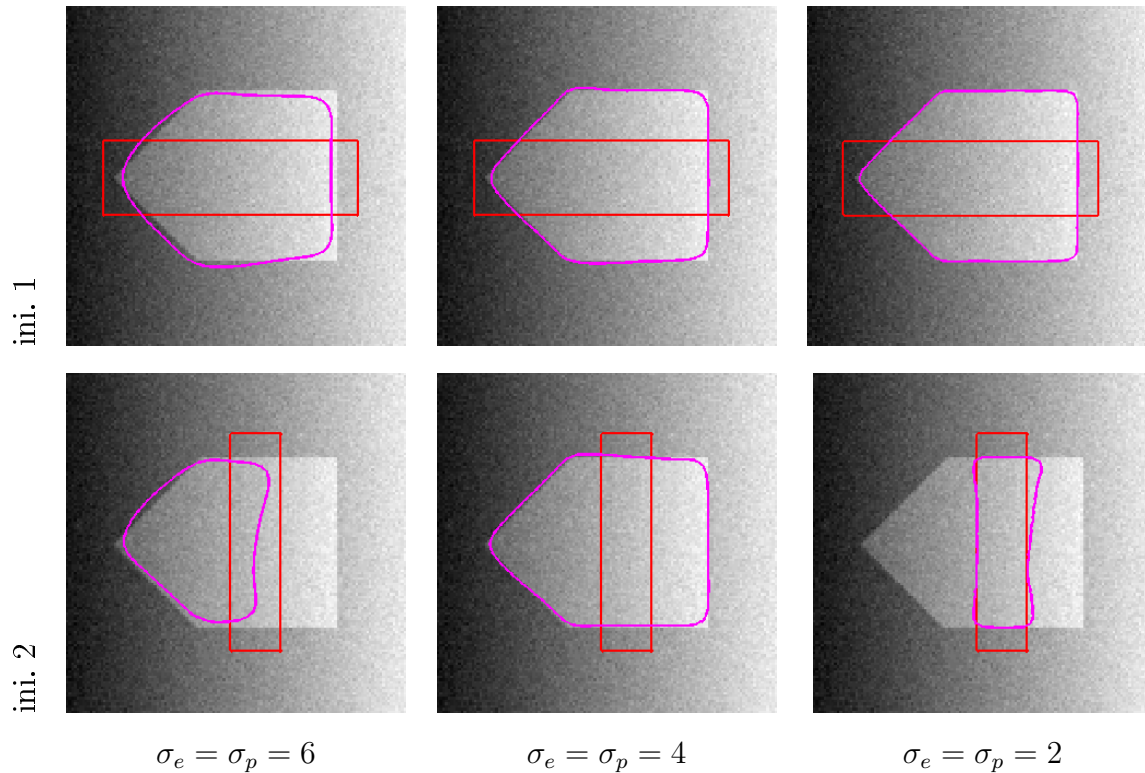


Figure 3.6 – Segmentation examples with the Gaussian fitting model Eq. (3.11). The figure illustrates the importance of the choices of kernel’s sizes when $\sigma_e = \sigma_p$. The best scales are 2 for ini. 1 and 4 for ini. 2. Even these best results have mis-localisation problems at sharp corners.

Figure 3.6 shows the segmentation results using the local Gaussian fitting method when $\sigma_e = \sigma_p$ on the test image shown previously. For the first column $\sigma_e = \sigma_p = 6$, the obtained segmentations have serious mis-localisation issues. When the estimation of the model parameters becomes more local, $\sigma_e = \sigma_p = 2$ for the first initialisation and 4 for the second initialisation, this local Gaussian model gives its best result. The over-smoothing of the contour however, still remains at sharp corners. If the locality shrinks further, such as $\sigma_e = \sigma_p = 2$ in the second row, only the partial boundary close to the initial contour can be found. Therefore, similar to the BC model, picking an optimal scale for E_{wang} is required in order to achieve a satisfactory segmentation result.

Remarks :

1. The BC model in Eq. (3.5) can be seen as simply using a spatially varying region-based statistics to replace the constant ones in the global energy. The Localised energy functions described in Eq. (3.10) and Eq. (3.11) use double integrals, which are essentially different from the BC model.
2. The local binary fitting and the local Gaussian fitting introduced in [120, 196],

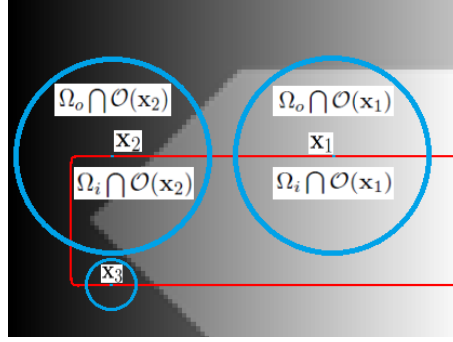


Figure 3.7 – Demonstration of a priori probability. For the marked points $\mathbf{x}_1, \mathbf{x}_2, \mathbf{x}_3$ along the contour C , the two partitions for \mathbf{x}_2 do not have equal probability.

assumed that all partitions $p(\mathbf{y} \in \Omega_r \cap \mathcal{O}(\mathbf{x}))$ have a priori equal probabilities. Hence this term has been ignored. In practice, this assumption is not always true. As illustrated in Fig. 3.7, $p(\mathbf{y} \in \Omega_i \cap \mathcal{O}(\mathbf{x}_1)) = p(\mathbf{y} \in \Omega_o \cap \mathcal{O}(\mathbf{x}_1)) = 1/2$, however, clearly $p(\mathbf{y} \in \Omega_i \cap \mathcal{O}(\mathbf{x}_2)) < p(\mathbf{y} \in \Omega_o \cap \mathcal{O}(\mathbf{x}_2))$. In addition, we check that for the point \mathbf{x}_3 , $p(\mathbf{y} \in \Omega_i \cap \mathcal{O}(\mathbf{x}_3)) = p(\mathbf{y} \in \Omega_o \cap \mathcal{O}(\mathbf{x}_3)) = 1/2$ because the size of the local kernel is very small. Therefore, this underlying assumption is reliable only when σ_e is extremely small and when the image boundary does not have sharp corners.

3. According to [120, 196], the local kernel K_{σ_e} is chosen to be a Gaussian one, and $K = K_{\sigma_e}$ is assumed to calculate the local region statistics. Notice that σ_p should be large in order to better estimate the local image model parameters. This is the case when the initial contour is in a comparatively homogeneous region or when the image noise is important. On the other hand, increasing the value of σ_e will bring more bias to the energy function (because of the above point). This problem will be discussed later in § 3.5.2.

3.4 Local intensity fitting with bias correction

Li et al. [119] have recently combined the local intensity fitting models introduced in § 3.3 with a bias field estimation technique. They considered a multiplicative model of intensity inhomogeneity, thus the observed image I can be expressed by :

$$I(\mathbf{x}) = bJ(\mathbf{x}) + n , \quad (3.13)$$

where $J(\mathbf{x})$ is the true image, b refers to a bias field or a shading image, and n is the additive noise which is normally assumed to be zero mean Gaussian noise. In order to establish a local external energy for this model, two assumptions are made as follows :

1. The bias field b is varying slowly, which means $b(\mathbf{x})$ can be well approximated by a constant in the neighbourhood of \mathbf{x} .
2. The true image $J(\mathbf{x})$ is approximated by N distinct constant values $\{c_r\}_{r=1}^N$ in different regions $\{\Omega_r\}_{r=1}^N$.

In a circular neighbourhood $\mathcal{O}(\mathbf{x})$, the values $b(\mathbf{y})$ for all \mathbf{y} are close to $b(\mathbf{x})$. In other words, $b(\mathbf{y}) \approx b(\mathbf{x})$, when $|K_{\sigma_e}(\mathbf{y} - \mathbf{x})| > 0$. Then, in each subregion $\mathcal{O}(\mathbf{x}) \cap \Omega_r$, $b(\mathbf{y})J(\mathbf{y})$ approximates $b(\mathbf{x})c_r$. Therefore, the image model in Eq. (3.13) is locally equivalent to :

$$I(\mathbf{y}) = b(\mathbf{x})c_r + n(\mathbf{y}) \ , \ \mathbf{y} \in \mathcal{O}(\mathbf{x}) \cap \Omega_r \ . \quad (3.14)$$

In the view of a clustering problem, the observed image intensities could be seen as N clusters with centres $b(\mathbf{x})c_r$. Note that the cluster centres are function of image position \mathbf{x} . This is what the authors have denoted as a "local intensity clustering property". Thus given a local clustering criterion, Li and colleagues proposed a global energy function to achieve the segmentation. For instance assuming that the variance is constant, the L_2 norm is used as a local clustering criterion which leads to the following energy data term [119] :

$$E_D = \int_{\Omega} \left(\sum_r \int_{\Omega_r} K_{\sigma_e}(\mathbf{x} - \mathbf{y}) |I(\mathbf{y}) - b(\mathbf{x})c_r|^2 d\mathbf{y} \right) d\mathbf{x} \ . \quad (3.15)$$

Minimising the above energy with respect to b for fixed ϕ and c_r gives :

$$\text{where } \hat{b}(\mathbf{x}) = \frac{\{I \sum_r c_r H_r(\phi)\} * K_{\sigma_e}}{\{\sum_r c_r^2 H_r(\phi)\} * K_{\sigma_e}} \ , \ r = 1, 2, \dots, N \ . \quad (3.16)$$

Alternatively, minimising with respect to c_r for fixed ϕ and b gives :

$$\hat{c}_r = \frac{\int_{\Omega} H_r(\phi) (b * K_{\sigma_e}) I d\mathbf{x}}{\int_{\Omega} H_r(\phi) (b^2 * K_{\sigma_e}) d\mathbf{x}} \ , \ r = 1, 2, \dots, N \ . \quad (3.17)$$

Given the estimates \hat{b} and \hat{c}_r , the minimisation of Eq. (3.15) with respect to ϕ can be obtained by means of the Gâteaux derivative :

$$\frac{\partial E_D(\phi)}{\partial t} = - \sum_r \delta(\phi) \int_{\Omega_r} K_{\sigma_e}(\mathbf{x} - \mathbf{y}) |I(\mathbf{y}) - \hat{b}(\mathbf{x})\hat{c}_r|^2 d\mathbf{y} \ . \quad (3.18)$$

When $b = 1$, this local clustering function reduces to the data fitting term. This term, which can be seen as a generalised CV model, aims at finding piecewise constant means. The energy in Eq. (3.15) evaluates the classification of the intensities in the neighbourhood $\mathcal{O}(\mathbf{x})$ given by the current partition.

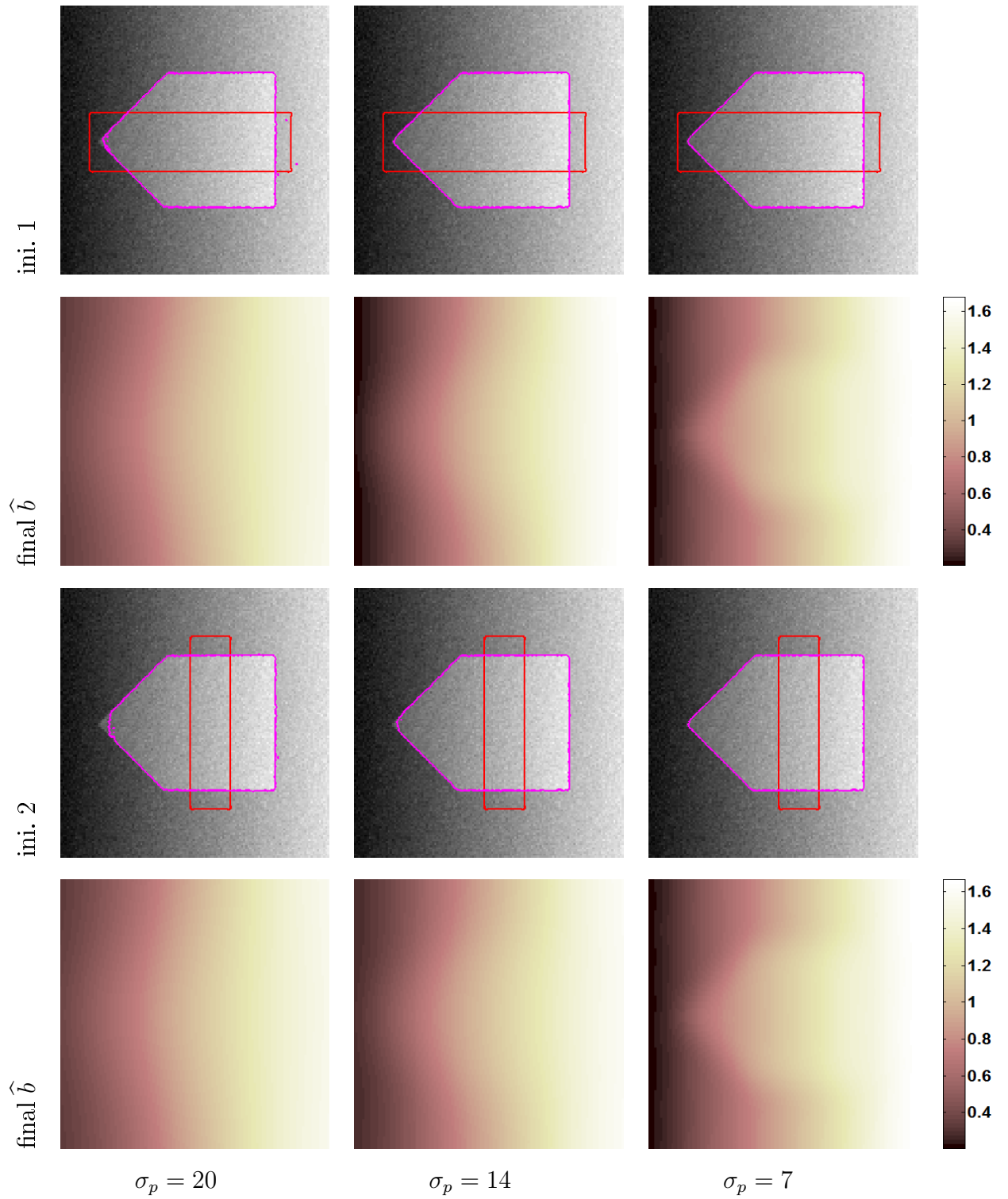


Figure 3.8 – Influence of the scale of the local kernel and the initialisation on the segmentation method using bias correction. From top to bottom : segmentation results and corresponding bias field estimations. $\nu = 650$.

Figure 3.8 is a segmentation example of the degraded noisy image using Eq. (3.18). At each time step, the contour and the bias field are updated according to Eq. (3.16). Thus, the segmentation and the bias field estimation are jointly performed while minimising this data-driven energy. Notice that the bias correction energy function Eq. (3.15) is not normalised, thus the corresponding weight for internal energy should be important. In this test, we choose a very large ν for the length term $|C|$, in order to avoid the over-segmented problem. However, this could prevent the curve C to reach the sharp boundary. Indeed, for both initialisations, using the large scale $\sigma_p = 20$ can not obtain the left corner of the object of interest. To summarize this experiment, the bias correction procedure is more significant for smaller local scales, and can help in the segmentation of inhomogeneous objects, to a certain degree.

3.5 General framework for region-based methods

3.5.1 Lankton and Tannenbaum model

Lately, Lankton and Tannenbaum have proposed a framework to guide active contours in segmentation, which can be used to localise global region-based energies [109] :

$$E_{LT}(\phi) = \int_{\Omega_{\mathbf{x}}} \delta(\phi(\mathbf{x})) \int_{\Omega_{\mathbf{y}}} K_{\sigma_e}(\mathbf{x}, \mathbf{y}) F(I(\mathbf{y}), \phi(\mathbf{y})) d\mathbf{y} d\mathbf{x} , \quad (3.19)$$

where the local mask $K_{\sigma_e}(\cdot, \cdot)$ performs similarly as that in local fitting models. F is an energy measure used to represent local adherence to a given model at each point along the contour. The Dirac function $\delta(\phi(\mathbf{x}))$ is multiplied in the outer integral ; i.e. the defined energy function is a line integral along the contour. Notice that this term ensures that the curve will not change topology by spontaneously developing a new contour, although it still allows the contour to split and merge. For every point \mathbf{x} selected by δ , $K_{\sigma_e}(\cdot, \cdot)$ guarantees that F operates on local image information about \mathbf{x} . Therefore, the total energy is the sum of values for every neighbourhood along the zero level set.

By taking the partial derivative of the energy $E_{LT}(\phi)$ with respect to ϕ , the evolution function is given by [109] :

$$\frac{\partial E_{LT}(\phi)}{\partial t} = \delta(\phi(\mathbf{x})) \int_{\mathcal{O}_{\mathbf{y}}} K_{\sigma_e}(\mathbf{x}, \mathbf{y}) \nabla_{\phi(\mathbf{y})} F(I(\mathbf{y}), \phi(\mathbf{y})) d\mathbf{y} . \quad (3.20)$$

Thus, the only restriction on the function F is that its first variation with respect to ϕ

can be computed. For example, the local binary fitting model has :

$$\begin{aligned} F(I(\mathbf{y}), \phi(\mathbf{y})) &= H(\phi(\mathbf{y}))(I(\mathbf{y}) - \mu_i(\mathbf{x}))^2 + H(-\phi(\mathbf{y}))(I(\mathbf{y}) - \mu_o(\mathbf{x}))^2 \\ \Rightarrow \nabla_{\phi(\mathbf{y})} F(I(\mathbf{y}), \phi(\mathbf{y})) &= \delta(\phi(\mathbf{x})) [(I(\mathbf{y}) - \mu_i(\mathbf{x}))^2 - (I(\mathbf{y}) - \mu_o(\mathbf{x}))^2] . \end{aligned}$$

After the estimation of the local means for current segmentation, the above function can be substituted directly into Eq. (3.20) to form the evolution of a completely localised energy. With this framework, more examples such as the local mean separation and the local histogram separation methods are derived in [109].

3.5.2 Localised Bayesian interpretation

The segmentation problem can be described as the minimisation of the following localised Bayesian interpretation [196] :

$$E = \int_{\Omega} \left[\sum_r \int_{\Omega_r} K_{\sigma_e}(\mathbf{x} - \mathbf{y}) \log p(I(\mathbf{y}) | \mathbf{y} \in \Omega_r) d\mathbf{y} \right] d\mathbf{x} + \nu |C| , \quad (3.21)$$

where the pdf $p(I(\mathbf{y}) | \mathbf{y} \in \Omega_r)$ models the distribution of local image intensities.

The scale σ_p controls the size of region used for estimating the local image statistics, and σ_e decides the contribution points in curve evolution. Here, we first eliminate the assumption that $\sigma_p = \sigma_e$ in [120, 109, 196], and consider their values separately. Then, it can be shown that, based on the above energy function, most existing region-based segmentation methods can be included as special cases. For instance, when $\sigma_e = 0$ and $p(I(\mathbf{y}) | \mathbf{y} \in \Omega_r)$ follows the local Gaussian distribution, the energy function Eq. (3.21) degrades into the BC model Eq. (3.5). It can be simplified further by setting to a constant the standard deviation $\sigma_r = \sqrt{0.5}$ for the whole image domain; the method becomes a piecewise smooth one. Moreover, if μ_r is no longer a function but collapses into a single value, which is known as the cartoon limit. In the particular case of a binary segmentation,

| σ_p | σ_e | μ_r | σ_r | method |
|----------------------|-----------------------|-----------------|--------------|-------------------------|
| $\sigma_p = +\infty$ | $\sigma_e = 0$ | global binary | $\sqrt{0.5}$ | Chan & Vese [40] |
| $\sigma_p = +\infty$ | $\sigma_e = 0$ | global Gaussian | global | Rousson & Deriche [172] |
| $\sigma_p = a$ | $\sigma_e = \sigma_p$ | local binary | $\sqrt{0.5}$ | Li et.al [120] |
| $\sigma_p = a$ | $\sigma_e = \sigma_p$ | local Gaussian | local | Wang et.al [196] |
| $\sigma_p = a$ | $\sigma_e = 0$ | local Gaussian | local | Brox & Cremers [32] |

Table 3.1 – Region-based Segmentation Methods. $a \in \mathbf{R}^+$.

Eq. (3.21) becomes the formula of the CV model. Table 3.1 gives a summary of the above discussion.

The general frameworks in Eq. (3.19) and Eq. (3.21) are different in several aspects. The outer integral of the former equation includes the contributions from the points nearby the zero level set, while the latter integrates over all the \mathbf{x} in the image domain Ω . Regarding the locality, Eq. (3.19) uses $\sigma_p = \sigma_e$, thus, it has the same problem in fixing the size of local kernel as the local fitting models introduced in § 3.3. Facing with this dilemma, we suggest that σ_e should be much smaller than σ_p . Therefore, on one hand, the model becomes more general and is capable to include more energies. On the other hand, a larger local window can be used in order to estimate the local model parameters. For instance, we tested minimising Eq. (3.21) with a fixed $\sigma_e = 1$ by different σ_p . According to the obtained results shown in Fig. 3.9, we notice that a very small σ_e causes less mislocalisation and gives a smoother segmentation, also using $\sigma_p \gg \sigma_e$ has the potential to give a better estimation of local image statistics when intensity inhomogeneity is less strong.

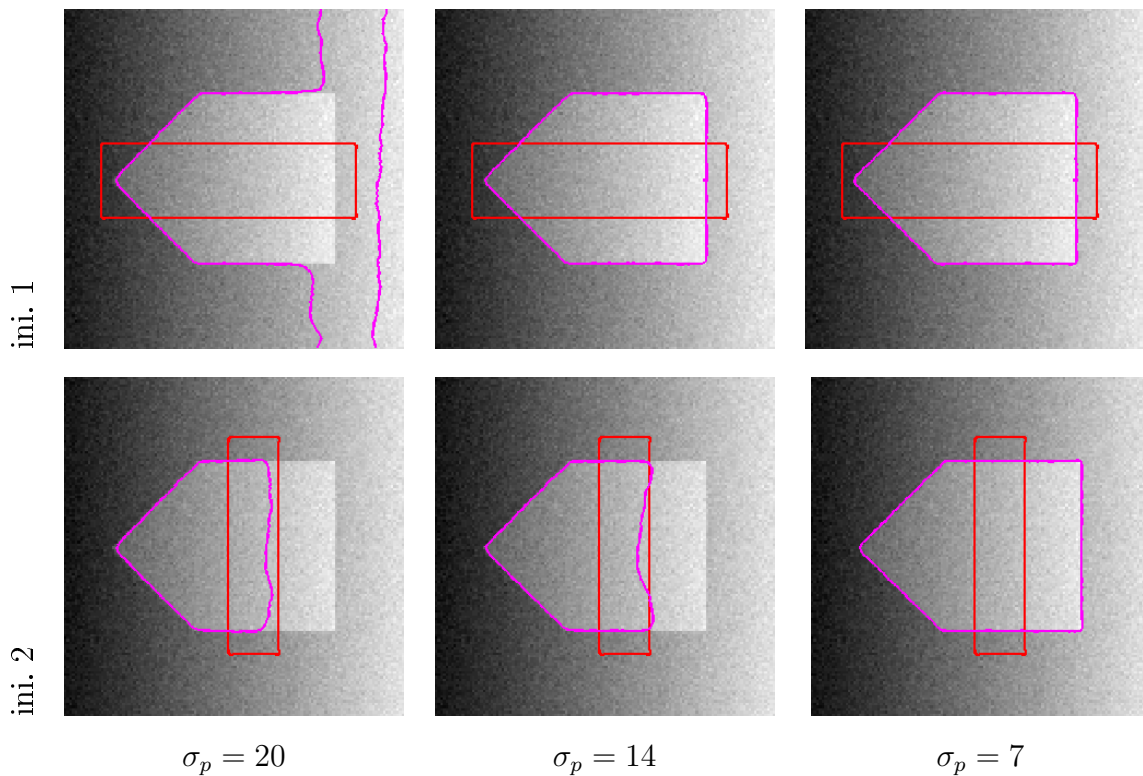


Figure 3.9 – Segmentation results of Eq. (3.21) when $\sigma_e = 1$. From left to right, the kernel size σ_p changes for the estimation of local region statistics. The above results are to be compared to Fig. 3.6

3.6 Conclusion

In this chapter, we focused on several recently developed algorithms based on local region statistics, including the BC model [32], local intensity fitting model [120, 196] and the local fitting model with bias field correction [119]. We also gave some segmentation examples of synthetic images with intensity inhomogeneities. We also reviewed the general framework for local region-based segmentation models proposed in [109]. Finally, we presented a synthesis of most local methods base on a variant of the Bayesian interpretation in [196]. Although local image statistics outperforms global ones for the segmentation of inhomogeneous images, their results are still sensitive, mainly to the initialisation. The results are also highly dependent on the choice of size of the locality. The following chapter will introduce several possible solutions to these problems, such as the combination of global and local image information as well as scale selection strategies for local active contours.

Optimal spatial adaptation for local region-based segmentation

Chapter summary

In this chapter, we will concentrate on discussing local region-based segmentation methods. More specifically, we aim to give answers to two questions. i) How global and local image information can be combined? ii) How to estimate an appropriate size of the spatial kernel that defines locality? First, we will briefly review several algorithms that solve similar issues in image denoising. Then, we consider segmentation methods that use both global and local image information. Finally, our main contributions will be presented in more details.

Contents

| | |
|---|-----------|
| 4.1 Introduction | 54 |
| 4.2 Denoising methods | 55 |
| 4.3 Combination of global and local image statistics | 58 |
| 4.3.1 A MAP-MRF framework | 58 |
| 4.3.2 Local and global intensity fitting energy | 59 |
| 4.3.3 Non-local active contours | 59 |
| 4.4 Local region-based methods with adaptive scales | 60 |
| 4.4.1 Piovano-Papadopoulos scale selection strategy | 60 |
| 4.4.2 LPA-ICI rule | 62 |
| 4.4.3 Proposed segmentation algorithm | 71 |
| 4.5 Conclusion | 78 |

4.1 Introduction

Local region-based segmentation models are surely better alternatives to global ones for images in the presence of intensity inhomogeneities. However, they are found to be more sensitive to initialisations if the local spatial scale is not chosen appropriately. A decrease of robustness to noise is also observed when small neighbourhoods are used. Therefore, this brings out two problems : the combination of global and local image statistics in one model and the selection of optimal pixel-dependent scales for local methods. Facing with these problems, the rest of this chapter will be organized as the following three parts.

We can learn a lot from the progress of denoising methods [34, 99, 101, 100], which aim at smoothing images while preserving edges. Conventional denoising techniques, such as filtering, are based on local averaging. Therefore, these problems of choosing locality also exist in image denoising area. An increase of the size of the averaging window does not solve the problem, as it brings bias into image regions where the noise free data are not constant. In this perspective, the possible solution is to use an adaptive number of image pixels assigned with data-dependent contributions in the filtering process.

A first segmentation model, which uses both global and local information within the level set framework, has been proposed by Wang et al. [197]. Their approach is straightforward in the sense that it adds two energy functions of the same nature, where the region-based statistics are estimated globally in one and locally in the other. In fact, this is not the first time that global and local image statistics are combined together for the purpose of solving a segmentation problem. To our knowledge, the first proposition has been introduced in [24, 23] within the Bayesian framework. The authors focus on the adaptive character of a MAP algorithm and discuss how global and local region statistics are utilised in order to control the adaptive properties of the segmentation process.

Similar to image denoising, an appropriate size of the local kernel can help in obtaining a meaningful segmentation than using an empirically fixed one. Two pixel-dependent scale selection strategies have been recently introduced in local region-based active contours. The first was by Piovano and Papadopoulo, which defines the local scale as the smallest one inducing an evolution speed superior to a given threshold [163]. The second one is by us, where we proposed an optimal scale in the sense of the MSE minimisation of a Local Polynomials Approximation of the observed image conditional on the current segmentation [209]⁶.

6. Although the work of Piovano and Papadopoulo was published before ours, we were not aware of it until the beginning of year 2012.

4.2 Denoising methods

Suppose the independent random observations $I(\mathbf{x}_s)$ are given in the form :

$$I(\mathbf{x}_s) = J(\mathbf{x}_s) + n(\mathbf{x}_s) \quad , \quad s = 1, \dots, m \quad , \quad (4.1)$$

where the observations coordinates \mathbf{x}_s are known. The original noise free image J is corrupted by a zero-mean white Gaussian noise $n(\cdot)$. The goal of image denoising methods is to recover the unknown image J from the noisy measurement $I(\mathbf{x}_s)$. In order to search for efficient denoising algorithms, several popular solutions exist in the literature [190, 98, 34, 106, 99, 101, 167, 100, 86].

Image denosing techniques through filtering assume that images typically vary slowly over space. So adjacent pixels are likely to have similar values, and it is appropriate to average them together. However, this assumption fails at edges, which are consequently blurred by low-pass filtering. Tomasi and Manduchi [190] have proposed the bilateral filter for edge preserving smoothing. This filter is a normalised weighted average of a neighbourhood around \mathbf{x}_s , given by :

$$\hat{J}(\mathbf{x}_s) = \frac{\sum_{\mathbf{x} \in \mathcal{O}(\mathbf{x}_s)} w[\mathbf{x}_s, \mathbf{x}] I(\mathbf{x})}{\sum_{\mathbf{x} \in \mathcal{O}(\mathbf{x}_s)} w[\mathbf{x}_s, \mathbf{x}]} \quad . \quad (4.2)$$

The weights $w[\mathbf{x}_s, \mathbf{x}]$ are defined by multiplying a spatial closeness function w_c with an intensity similarity function w_s :

$$w[\mathbf{x}_s, \mathbf{x}] = \underbrace{f(\|\mathbf{x}_s - \mathbf{x}\|, \sigma_s)}_{w_c} \underbrace{\exp\left(-\frac{(I(\mathbf{x}_s) - I(\mathbf{x}))^2}{2\sigma_I^2}\right)}_{w_s} \quad . \quad (4.3)$$

Therefore, the weights $w[\mathbf{x}_s, \mathbf{x}]$ includes two ingredients. The first term measures the geometric proximity $\|\mathbf{x}_s - \mathbf{x}\|$. The function f is monotonically non-increasing, which may take many forms, such as a Gaussian with a variance σ_s^2 . This way, close-by samples influence the final result more than distant ones. The second weight is the proximity among the observed intensities $I(\mathbf{x}_s)$ and $I(\mathbf{x})$. The parameter σ_I controls the effect of the grey-level difference between the two pixels. This way, when two pixels are different, the corresponding weight is very small. Thereby, this neighbour should not be trusted in averaging.

The non-local means (NLM) filter [34] could be seen as a generalisation of the bilateral filtering [167]. The radiometric part in the weights of the NLM is computed by the Euclidean distance between two image patches, which are centred at the involved two

pixels :

$$w[\mathbf{x}_s, \mathbf{x}] = \underbrace{f(\|\mathbf{x}_s - \mathbf{x}\|, \sigma_s)}_{w_c} \underbrace{\exp\left(-\frac{\|\mathbf{R}_{\mathbf{x}_s}^I - \mathbf{R}_{\mathbf{x}}^I\|^2}{2\sigma_I^2}\right)}_{w_s}. \quad (4.4)$$

Here, $\mathbf{R}_{\mathbf{x}_s}^I$ is an operator which extracts a patch of a fixed and pre-determined size ($\tau \times \tau$) from the observed image. For instance,

$$\mathbf{R}_{\mathbf{x}_s}^I(\mathbf{l}) = I(\mathbf{x}_s + \mathbf{l}), \quad \forall \mathbf{l} \in [-\tau/2, \tau/2]^2. \quad (4.5)$$

Obviously, when $\mathbf{R}_{\mathbf{x}_s}^I$ extracts only a single pixel, the bilateral filter emerges as a special case of the NLM algorithm.

The choice of σ_s suffers from the same problem as the scale σ_p in local image statistics estimations for segmentation. A variant of the NLM filter optimises explicitly the size of the local window in order to achieve the best trade-off between a minimum bias and a minimum variance of the estimates [101]. The selection of the best parameters of the NLM filter is also addressed in [59]. Their approach is based on a popular method of risk estimation, namely the Stein Unbiased Risk Estimate (SURE) [186]. Thus, it is also a bias and variance trade-off method, but differs from the work in [101]. This is because the SURE method focuses on the choice of the smoothing parameter σ_I and the latter on the size of the searching window σ_s .

Anisotropic LPA-ICI denoising

An alternative approach to the above mentioned denoising techniques is based on a Local Polynomial Approximation (LPA) of image patches. Katkovnik et al. [98, 99] have proposed a selection mechanism based on a bias and variance trade-off to optimise the size of the local spatial window. Formally, the selection algorithm is based on the Intersection of Confidence Intervals (ICI) rule, first proposed in [76, 97]. The most general formulation of the LPA-ICI method can estimate not only the size of the local window, but also its shape when it is used in its anisotropic form. This method uses a starshaped estimation of the neighbourhood at each point. The starshape kernel offers enough geometrical flexibility to fit to edges in a large number of natural images. Examples of the ideal neighbours are labelled by the grey regions in Fig. 4.1. In order to describe these starshapes, a directional adaptive scale estimator has been introduced by Katkovnik et al. [98]. The authors use a set of sectors characterized by a direction and an optimal scale obtained by the anisotropic LPA-ICI approach. Figure 4.2 shows examples of estimations of sectorial kernels for image denoising, where the directional resolution polar coordinates is 16.

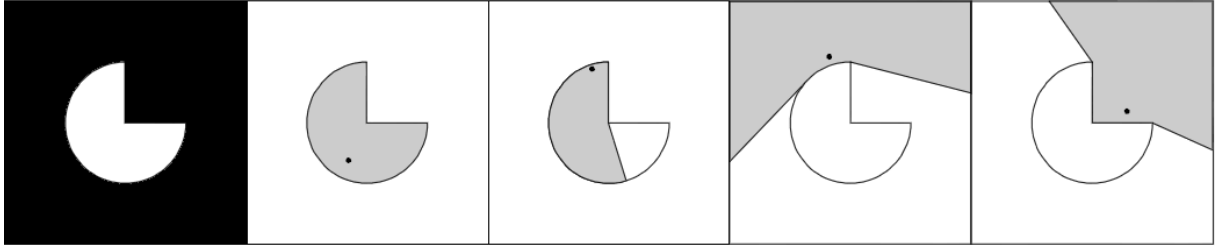


Figure 4.1 – Examples of ideal starshaped neighbourhoods [66]. From left to right : true image, illustration of ideal spatial neighbourhoods used for denoising at four different pixel locations.

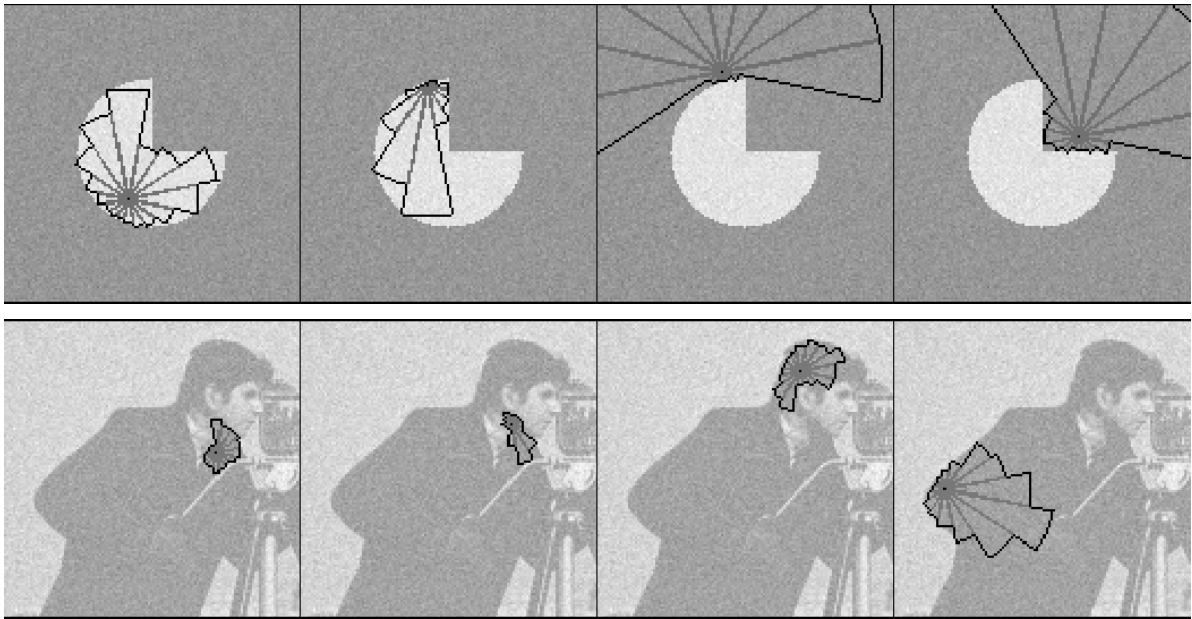


Figure 4.2 – Examples of optimal neighbourhoods obtained by the LPA-ICI rule using sectorial kernels [66]. Any two different sectors overlap only in the central point. Notice that the shape and the size of estimated windows are well adapted to image content at different pixel locations. This anisotropic kernel ensures the LPA-ICI filter to average only i.i.d. observations.

Denoising example : Finally, figure 4.3 shows the denoising example obtained by the NLM and the anisotropic LPA-ICI. Both methods appear to be promising, which successfully reduce the noise and preserve the edge information.

In the rest of this chapter, we will first introduce three typical segmentation methods, which use both global and local image statistics. Then, our main contributions will be detailed in § 4.4. Alternative to using a fixed local scale, we will concentrate on finding the optimal window size for local region-based segmentation method. Motivated by the anisotropic LPA-ICI algorithm, we have proposed a local region-based segmentation method with an adaptive scale selection strategy. Finally, we will discuss the performances of our approach in dealing with image intensity inhomogeneities.



Figure 4.3 – Image denoising example using the NLM and the anisotropic LPA-ICI. From left to right : the noisy image with SNR=14dB, the NLM and the anisotropic LPA-ICI denoising results. For the NLM, $\sigma_s = 2$, the similarity window $\tau = 5$, and $\sigma_I^2 = 0.9\hat{\sigma}^2$, where $\hat{\sigma}^2$ is the estimated noise variance from the observed image. For the anisotropic LPA-ICI, the optimal scale is chosen from the set $\mathbf{h} = [3, 6, 9, 15, 21, 33]$, the parameter Γ controls the trade-off between bias and variance is 1.05, and the directional resolution is 8.

4.3 Combination of global and local image statistics

4.3.1 A MAP-MRF framework

Boukerroui et al. [24, 23] have proposed a region-based segmentation method and discussed how global and local image statistics can be utilised within a Bayesian framework. Their approach introduced an enhancement in controlling the adaptive properties of the segmentation process. Thus, its data-driven energy function to be minimised is given by [23] :

$$E_D = \sum_{\mathbf{x}_s \in \Omega} \varphi(w_r(\mathbf{x}_s), a) \left[\left(\frac{I(\mathbf{x}_s) - \mu_r(\mathbf{x}_s)}{\sqrt{2}\sigma_r(\mathbf{x}_s)} \right)^2 + \log(\sigma_r(\mathbf{x}_s)) \right]. \quad (4.6)$$

$\mu_r(\mathbf{x}_s)$ and $\sigma_r(\mathbf{x}_s)$ are local region statistics of the segmentation class r , whose similarity to global image statistics are measured by the weighting coefficient $w_r(\mathbf{x}_s)$. The weight $w_r(\mathbf{x}_s)$ can be determined by any similarity measure. For instance, the authors used the Kolmogorov-Smirnov distance between the global images statistics and the local one. The idea behind this mechanism is to favour the expansion of homogeneous region. The positive parameter a controls the contribution of the global region statistics, i.e. for large values of a the function $\varphi = 1$ for all r . Meaning the global data-driven information is not taken into account. However, for small a values, inhomogeneous regions are penalised by increasing their contribution in the energy function.

4.3.2 Local and global intensity fitting energy

Within the level set framework, a region-based model, including local and global image information, has been proposed in [197]. Its external energy term is a direct linear combination of a local intensity fitting term [120], which is responsible for attracting the contour towards boundaries, and an equivalent global fitting one, which improves the robustness :

$$E_D = (1 - \omega) \underbrace{\int_{\Omega} \left(\sum_r \int_{\Omega_r} K_{\sigma_e}(\mathbf{x} - \mathbf{y}) |I(\mathbf{y}) - \mu_r(\mathbf{x})|^2 d\mathbf{y} \right) d\mathbf{x}}_{E_{Li}} + \omega \underbrace{\sum_r \int_{\Omega_r} (I(\mathbf{x}) - \mu_r)^2 d\mathbf{x}}_{E_{CV}} , \quad (4.7)$$

where the positive weighting parameter ω belongs to $[0, 1]$. Clearly, the evolution equation of the gradient descent of the energy is also a linear combination of the corresponding forces of Li and CV given respectively in Eq. (3.10) and Eq. (2.24).

The influence of these two energies on the curve evolution is complementary. Indeed, it is well known that global image statistics are more robust to initialisations. If the initial contour is far away from the true boundaries, the local energy will be unable to drive the contour to an acceptable result. In such cases, the global energy should be dominant, thus a relatively large ω should be used. On the contrary, the accuracy of a segmentation of an image with inhomogeneities relies on local image statistics. Local region statistics should be essential for images with severe inhomogeneities, which means a small ω should be chosen. Otherwise the global force may prevent the segmentation contour from stopping at true boundaries. In the original local and global intensity fitting model [197], the value of ω is a constant, which is chosen according to the degree of inhomogeneity. Alternatively, authors of [216, 205] proposed that the contribution of global energy term ω could be defined dynamically by local contrast of the image.

4.3.3 Non-local active contours

Non-local methods, originally proposed by Buades et al. for denoising, have been explored in many papers because they are well adapted to texture. The idea has been extended to image segmentation by [74, 61, 27, 95]. For example, Jung et al. [95] have recently proposed a novel class of segmentation energies that imposes a local homogeneity of patch features. This method is based on comparisons between pairs of patches within each region [95] :

$$d(\mathbf{R}_x^I, \mathbf{R}_y^I) = \int_1 K_a(\mathbf{l}) \|\mathbf{R}_x^I(\mathbf{l}) - \mathbf{R}_y^I(\mathbf{l})\|^2 d\mathbf{l} , \quad (4.8)$$

where K_a is used to give more influence to the central pixel, and a truncated Gaussian kernel is commonly applied. \mathbf{R}_x^I and \mathbf{R}_y^I , satisfying Eq. (4.5), are two patches of the observed image centred at image points \mathbf{x} and \mathbf{y} respectively. The non-local interaction $d(\cdot, \cdot)$ measures the similarity between these patches. This weighted distance only constrains the local homogeneity, which is crucial to capture regions with smoothly spatially varying features.

The data-driven energy defined by the similarity of each local region is measured by considering all possible pairwise patch interactions at a given scale $b > 0$ [95] :

$$\begin{aligned} E_D &= \sum_r E_{NL}(\Omega_r) \\ &= \sum_r \int_{\Omega_r} \frac{\int_{\Omega_r} K_b(\mathbf{x}, \mathbf{y}) d(R_x^I, R_y^I) d\mathbf{y}}{\int_{\Omega_r} K_b(\mathbf{x}, \mathbf{y}) d\mathbf{y}} d\mathbf{x} . \end{aligned} \quad (4.9)$$

K_b is a decaying function of $\|\mathbf{x} - \mathbf{y}\|$. The parameter b is important since it controls the scale of the local homogeneity required for the segmented object. The minimisation of the above energy function enforces the similarity features within each region. By designing an appropriate $d(\cdot, \cdot)$, this energy can be adapted to various segmentation problems.

4.4 Local region-based methods with adaptive scales

In order to segment an image with intensity inhomogeneities, local image statistics should be used. However, for local region-based methods as well as the one combining both global and local image statistics, their segmentation results depend upon the choice of the scale of the local window⁷. In certain controlled situation, appropriate scales may be known a priori. But under most circumstances, it may not be obvious at all to determine in advance the proper scale. To cope with this problem, in this section, we aim to find the suitable scale for each point along the contour. First, we will briefly recall the scale selection method proposed by Piovano and Papadopoulo [163]. Then, we will introduce our main contributions.

4.4.1 Piovano-Papadopoulo scale selection strategy

In [163], the authors proposed a scale selection strategy when using local region statistics in active contours. Their idea is to find the most salient scale for each point

7. In this thesis, the window size and the scale are interchangeable concepts. We recall that we denote by h the half widows size and by σ_p, σ_e the kernel standard deviation.

in order to make the contour evolved locally. As mentioned earlier, it is desirable that the contour should evolve even in locally homogeneous area. Therefore, the pixel-dependent scale is defined as the smallest one inducing an evolution speed superior to a given threshold ξ [163] :

$$h^*(\mathbf{x}) = \inf_{h \in \mathbf{h}} \left(h : \left| \frac{\partial \phi(\mathbf{x})}{\partial t} \right| > \xi \right) . \quad (4.10)$$

The authors minimised the local region-based energy presented in the BC model Eq. (3.5). Thereby, the evolution speed in the level-set notation is obtained similarly.

This scale selection method can estimate continuous scales but for efficiency reasons, the search is generally limited to a finite set of ordered scale values $\mathbf{h} = \{h_1 < h_2 < \dots < h_u\}$. At each iteration of the level set evolution, various kernel sizes are used to obtain local image statistics. The optimal local scale is found for every image pixel along the zero level set function, by increasing h from the minimum h_1 to the maximum h_u , until the absolute value of the evolution speed is superior to ξ . Therefore, when the active contour is close to a boundary, small neighbourhoods are chosen ; and large neighbourhoods are applied if the segmentation curve is in homogeneous areas.

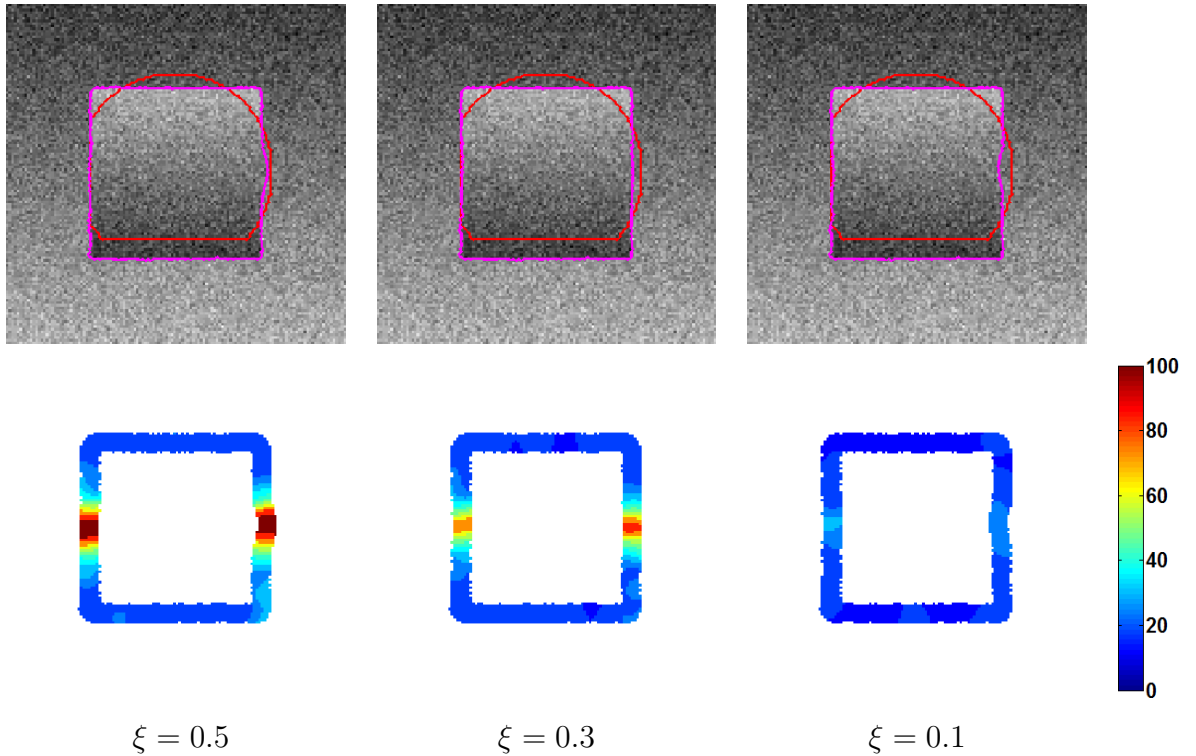


Figure 4.4 – Influence of the threshold ξ on the scale selection strategy proposed by Piovano and Papadopoulo. Top row : initial (red) and final (magenta) contour for three values of ξ . Bottom row : estimated sizes of the local kernels $\hat{h}(\mathbf{x})$, where \mathbf{x} are within a narrow band. The colourbar indicates the values of $\hat{h}(\mathbf{x})$. Image size is 128×128 , and $\mathbf{h} = [12, 14, 16, 18, 20, 22, 24, 27, 30, 33, 36, 40, 44, 48, 53, 58, 64, 70, 77, 84, 92, 100]$.

However, it is unclear how should we fix the positive constant ξ . For example, the segmentation of a synthetic image is shown in Fig. 4.4. Notice that we only consider the estimated scales $\hat{h}(\mathbf{x})$ within a narrow band. When the threshold is suitable, here $\xi = 0.3$ shown in the middle column, the Piovano's model selects proper scales for pixels around the curve. Accordingly, this method can help to segment the image with inhomogeneities. For $\xi = 0.5$ or $\xi = 0.1$, the selected scales have overestimation or underestimation problems in the middle right part, because of the very low contrast between the inside and the outside of the true boundary. Consequently, this model leads to similar segmentation results as the single scale local region-based model.

4.4.2 LPA-ICI rule

In the following section, we will introduce an alternative approach, in order to choose a good value for the spatial scale at every pixel location along the contour. The LPA is a powerful non-parametric estimation in a point-wise manner based on a mean square polynomial fitting in a sliding window. Similar to local segmentation method, the selection of an appropriate window size is of great interest for the LPA, in order to obtain the most natural and relevant approximation. Here, we mean by natural approximation a smooth one and relevant a non-biased one. The ICI rule [97, 98, 99] is an adaptation algorithm, which searches for the largest local window size where LPA assumptions fit well to the observations. The ICI rule can be applied with many existing linear and non-linear filters where a bias-variance trade-off is a good criterion for the parameter selection. The optimal window size is defined by a compromise between the bias and the variance of estimation.

4.4.2.1 Basis of LPA

Recall the noisy observation model defined in Eq. (4.1). The LPA assumes the true image J can be well approximated locally by a polynomial function in some neighbourhoods of the point of interest. It provides estimations in a point-wise manner, which finds the weighted least-square fitting in a sliding window. The LPA for the point $\mathbf{x} = (x, y)^T$ in a neighbourhood of the centre $\mathbf{x}_s = (x_s, y_s)^T$ is of the form :

$$J_h(\mathbf{x}, \mathbf{x}_s) = \mathbf{C}^T \boldsymbol{\psi}_h(\mathbf{x} - \mathbf{x}_s) , \quad (4.11)$$

$$\boldsymbol{\psi}_h(\mathbf{x}) = \boldsymbol{\psi}(\mathbf{x}/h) , \quad \boldsymbol{\psi}(\mathbf{x}) = [\psi_1(\mathbf{x}), \psi_2(\mathbf{x}), \dots, \psi_M(\mathbf{x})]^T ,$$

| m | M | $\boldsymbol{\psi}_h(x, y)$ |
|-----|-----|--|
| 0 | 1 | $\psi_1 = 1$ |
| 1 | 3 | $\psi_2 = -x \quad \psi_3 = -y$ |
| 2 | 6 | $\psi_4 = x^2/2 \quad \psi_5 = y^2/2 \quad \psi_6 = xy$ |
| 3 | 10 | $\psi_7 = -x^3/6 \quad \psi_8 = -y^3/6 \quad \psi_9 = -x^2y/6 \quad \psi_{10} = -xy^2/6$ |

Table 4.1 – 2D polynomials $\boldsymbol{\psi}$ for the order $m \in \{0, 1, 2, 3\}$.

where h is a scaling parameter. $\mathbf{C} = [C_1, C_2, \dots, C_M]^T$ is a vector of the parameters, and $\boldsymbol{\psi}$ is a vector of linearly independent 2D polynomials :

$$\boldsymbol{\psi} = (-1)^{k_1+k_2} \frac{x^{k_1} y^{k_2}}{k_1! k_2!}, \quad \text{with } k_1 + k_2 = 0, 1, \dots, m. \quad (4.12)$$

The total number of polynomials is equal to $M = (m + 2)(m + 1)/2$. For example, the above polynomials for the order $m \in \{0, 1, 2, 3\}$ are shown in Table 4.1. For an order m , the set of the polynomials includes the row corresponding to m as well as all rows with smaller values of m .

The standard LPA minimises the following weighted least-square criteria with respect to the coefficient \mathbf{C} [63] :

$$LS_h(\mathbf{x}) = \sum_{\mathbf{x}_s \in \Omega} w_h(\mathbf{x}_s - \mathbf{x}) (I(\mathbf{x}_s) - J_h(\mathbf{x}, \mathbf{x}_s))^2. \quad (4.13)$$

The window $w_h(\mathbf{x}) = \frac{1}{h^2} w\left(\frac{\mathbf{x}}{h}\right)$ satisfies the conventional properties of kernel estimates and h is a scaling parameter. The Taylor series for $I(\mathbf{x}_s)$ with the reference point \mathbf{x} is :

$$\begin{aligned} I(\mathbf{x}_s) &= J_h(\mathbf{x}) - \partial_x J_h(\mathbf{x})(x - x_s) - \partial_y J_h(\mathbf{x})(y - y_s) \\ &\quad + \frac{1}{2} \partial_x^2 J_h(\mathbf{x})(x - x_s)^2 + \frac{1}{2} \partial_y^2 J_h(\mathbf{x})(y - y_s)^2 + \partial_x \partial_y J_h(\mathbf{x})(x - x_s)(y - y_s) + \dots \end{aligned}$$

Consider the model $J_h(\mathbf{x}, \mathbf{x}_s)$ in Eq. (4.11) with the polynomials of the corresponding powers :

$$\begin{aligned} J_h(\mathbf{x}, \mathbf{x}_s) &= C_1 - \frac{C_2}{h}(x - x_s) - \frac{C_3}{h}(y - y_s) \\ &\quad + \frac{C_4}{2h^2}(x - x_s)^2 + \frac{C_5}{2h^2}(y - y_s)^2 + \frac{C_6}{2h^2}(x - x_s)(y - y_s) + \dots \end{aligned}$$

Therefore, the residuals in Eq. (4.13) can be given in the following form :

$$\begin{aligned} I(\mathbf{x}) - J_h(\mathbf{x}, \mathbf{x}_s) = & (J_h(\mathbf{x}) - C_1) + \left(\frac{C_2}{h} - \partial_x J_h(\mathbf{x}) \right) (x - x_s) + \left(\frac{C_3}{h} - \partial_y J_h(\mathbf{x}) \right) (y - y_s) \\ & + \left(\frac{1}{2} \partial_x^2 J_h(\mathbf{x}) - \frac{C_4}{2h^2} \right) (x_s - x)^2 + \left(\frac{1}{2} \partial_y^2 J_h(\mathbf{x}) - \frac{C_5}{2h^2} \right) (y_s - y)^2 \\ & + \left(\partial_x \partial_y J_h(\mathbf{x}) - \frac{C_6}{2h^2} \right) (x_s - x)(y_s - y) + \dots \end{aligned}$$

Because all the polynomials in the above equation are linearly independent, minimisation of Eq. (4.13) is equivalent to minimise $(J_h(\mathbf{x}) - C_1)$, $(\frac{C_2}{h} - \partial_x J_h(\mathbf{x}))$ and so on. In this way, the estimate of the function J_h is given as $\hat{J}_h(\mathbf{x}) = \hat{C}_1(\mathbf{x}, h)$ and similarly its derivative is given by :

$$\partial_x \hat{J}_h(\mathbf{x}) = \frac{C_2}{h} \quad , \quad \partial_y \hat{J}_h(\mathbf{x}) = \frac{C_3}{h} \quad , \quad \dots$$

The estimate given by the LPA can be written as the kernel operator on the observations [98, 99] :

$$\hat{J}_h(\mathbf{x}) = \sum_{\mathbf{x}_s \in \Omega} g_h(\mathbf{x}, \mathbf{x}_s) I(\mathbf{x}_s) \quad , \quad (4.14)$$

where the kernel is given by :

$$g_h(\mathbf{x}, \mathbf{x}_s) = w_h(\mathbf{x} - \mathbf{x}_s) \boldsymbol{\psi}_h^T(\mathbf{x} - \mathbf{x}_s) \boldsymbol{\Psi}_h^{-1} \boldsymbol{\psi}_h(0) \quad , \quad (4.15)$$

$$\boldsymbol{\Psi}_h = \sum_{\mathbf{x}_s \in \Omega} w_h(\mathbf{x} - \mathbf{x}_s) \boldsymbol{\psi}_h(\mathbf{x} - \mathbf{x}_s) \boldsymbol{\psi}_h^T(\mathbf{x} - \mathbf{x}_s) \quad .$$

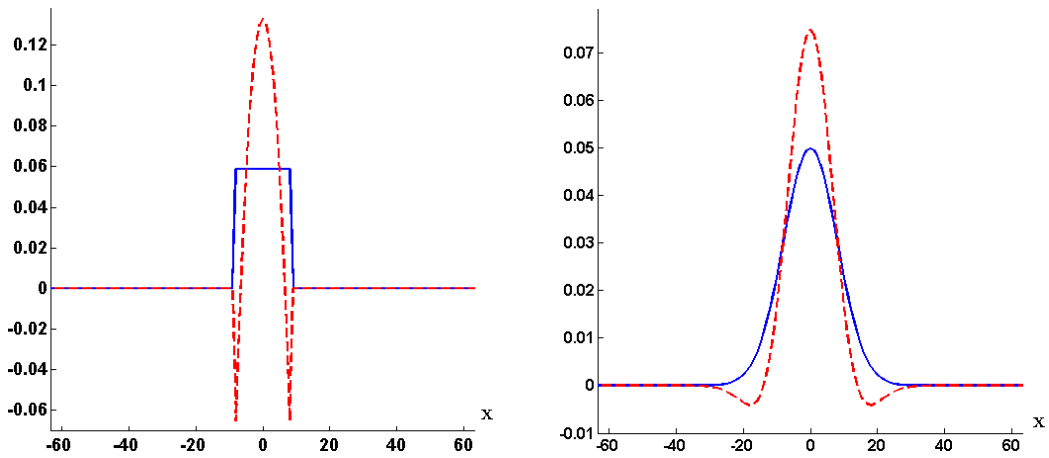


Figure 4.5 – The kernels g_h of the smoothing filters in Eq. (4.15). From left to right, g_h are designed with a symmetric rectangular window and a Gaussian window (w_h) of the orders $m = 0$ (blue continues lines) and $m = 2$ (red dotted lines). Notice that the increase of m reduces the bandwidth of these low-pass filters.

When the grid is assumed to be regular, the LPA kernel $g_h(\mathbf{x}, \mathbf{x}_s)$ becomes shift-invariant on \mathbf{x} , thereby, the solution of the above estimation is given by a convolution operation. The kernel g_h is defined by the window w_h and the set of polynomials $\boldsymbol{\psi}_h$. Figure 4.5 shows examples of the kernel g_h for 1D LPA. The g_h based on Gaussian model is smoother than the corresponding one based on a rectangular window.

4.4.2.2 Ideal scale

Let the accuracy of the LPA can be measured by the pointwise mean-square risk :

$$r_{\hat{J}_h}(\mathbf{x}, h) = \mathbb{E}\{(e_{\hat{J}_h}(\mathbf{x}, h))^2\} = \mathbb{E}\{(J(\mathbf{x}) - \hat{J}_h(\mathbf{x}))^2\} ,$$

where $e_{\hat{J}_h}(\mathbf{x}, h)$ is the error of estimation. This function can be written as the sum of the squared bias and the variance of the estimation :

$$\begin{aligned} r_{\hat{J}_h}(\mathbf{x}, h) &= \left(\mathbb{E}\{\hat{J}_h(\mathbf{x})\} - J(\mathbf{x}) \right)^2 + \mathbb{E} \left\{ \left(\hat{J}_h(\mathbf{x}) - \mathbb{E}\{\hat{J}_h(\mathbf{x})\} \right)^2 \right\} \\ &\quad + 2\mathbb{E} \left\{ \left(\mathbb{E}\{\hat{J}_h(\mathbf{x})\} - J(\mathbf{x}) \right) \left(\hat{J}_h(\mathbf{x}) - \mathbb{E}\{\hat{J}_h(\mathbf{x})\} \right) \right\} , \\ &= m_{\hat{J}_h}^2(\mathbf{x}, h) + \sigma_{\hat{J}_h}^2(\mathbf{x}, h) + 0 . \end{aligned} \quad (4.16)$$

Assume the given image is sampled by a small interval Δ , and the sampling grid is regular. Let the noise in the observation model in Eq. (4.1) be white with variance σ^2 . Omitting the higher-order terms in the estimation of bias and variance, the upper bound of the above mean-square risk $\bar{r}_{\hat{J}_h}$ is given by [98, 99] :

$$r_{\hat{J}_h}(\mathbf{x}, h) \leq \underbrace{\left(h^{m+1} J^{(m+1)}(\mathbf{x}) A_g \right)^2}_{\bar{m}_{\hat{J}_h}^2} + \underbrace{\sigma^2 \frac{\Delta^2}{h^2} B_g}_{\bar{\sigma}_{\hat{J}_h}^2} = \bar{r}_{\hat{J}_h}(\mathbf{x}, h) , \quad (4.17)$$

$$\text{with } A_g = \frac{1}{(m+1)!} \left| \int g(\mathbf{u}) \mathbf{u}^{m+1} d\mathbf{u} \right| , \quad B_g = \int g^2(\mathbf{u}) d\mathbf{u} ,$$

where $J^{(m+1)}$ is the $(m+1)^{th}$ derivatives of the noise free data.

The window size h is crucial for the accuracy of the LPA. Figure 4.6 demonstrates the influence of the h on the 1D LPA of a noise degraded signal. Obviously, using a small kernel size, generally leads to a small bias in estimation, but a large variance is caused by the noise. On the contrary, a big one brings a smooth estimation, which has a very larger bias for inhomogeneous parts and a small variance. Analyse the expression of mean-square risk in Eq. (4.17) and the above example of the LPA, we notice that : the bias of the estimation $m_{\hat{J}_h}$ is a monotonically increasing function of h , while the variance $\sigma_{\hat{J}_h}^2$ is a

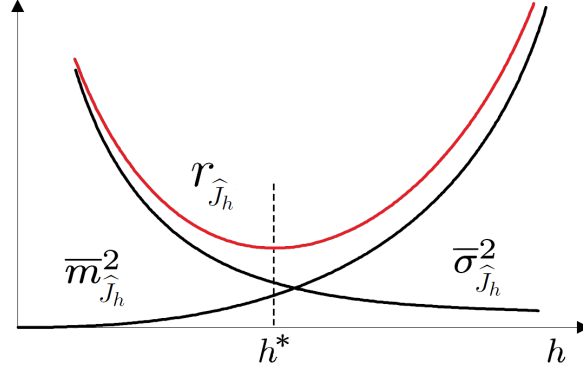


Figure 4.6 – The contribution of bias $\bar{m}_{\hat{J}_h}^2$ and variance $\bar{\sigma}_{\hat{J}_h}^2$ to the mean-square risk $r_{\hat{J}_h}$. The ideal scale h^* corresponds to the minimal $r_{\hat{J}_h}$.

monotonically decreasing one. Therefore, it exists a bias and variance balance giving the ideal scale $h^*(\mathbf{x})$, which can be found by the minimisation of the $r_{\hat{J}_h}(\mathbf{x})$. This idea leads to following inequality [98, 99] :

$$|\bar{m}_{\hat{J}_h}(\mathbf{x}, h)| \begin{cases} \leq \gamma \cdot \sigma_{\hat{J}_h}(\mathbf{x}, h) & \text{if } h \leq h^* , \\ > \gamma \cdot \sigma_{\hat{J}_h}(\mathbf{x}, h) & \text{if } h > h^* , \end{cases} \quad (4.18)$$

which means the ideal bias-variance trade-off is achieved when the ratio between the absolute value of the bias to the variance is equal to γ . Under the assumption of an additive Gaussian noise, the following inequality holds with probability $p = (1 - \alpha)$ [98, 99] :

$$|e_{\hat{J}_h}(\mathbf{x}, h)| \leq |\bar{m}_{\hat{J}_h}(\mathbf{x}, h)| + z_{(1-\alpha/2)} \sigma_{\hat{J}_h}(\mathbf{x}, h) , \quad (4.19)$$

where $z_{(1-\alpha/2)}$ is the $(1 - \alpha/2)^{th}$ quantile of the standard Gaussian distribution. $\sigma_{\hat{J}_h}$ is the standard deviation of the estimates, which can be estimated given the noise model and its variance :

$$\hat{\sigma}_{\hat{J}_h}^2(\mathbf{x}, h) = \sigma^2 \sum_{\mathbf{x}_s \in \Omega} g_h^2(\mathbf{x} - \mathbf{x}_s) .$$

The above function relies on the preliminary estimation of the noise variance $\hat{\sigma}^2$, which can robustly be estimated from the input data [110]. More details can be found in Appendix C.

4.4.2.3 The ICI Rule

The two inequalities Eq. (4.18) and Eq. (4.19) are the starting point for the development of a hypothesis testing, on which the data-driven scale selection method is built. Combine the first inequality of the former with the latter inequality, the estimation error satisfies :

$$|e_{\hat{J}_h}(\mathbf{x}, h)| \leq \underbrace{(\gamma + z_{(1-\alpha/2)})}_{\Gamma} \sigma_{\hat{J}_h}(\mathbf{x}, h) , \quad \forall h \leq h^*(\mathbf{x}) . \quad (4.20)$$

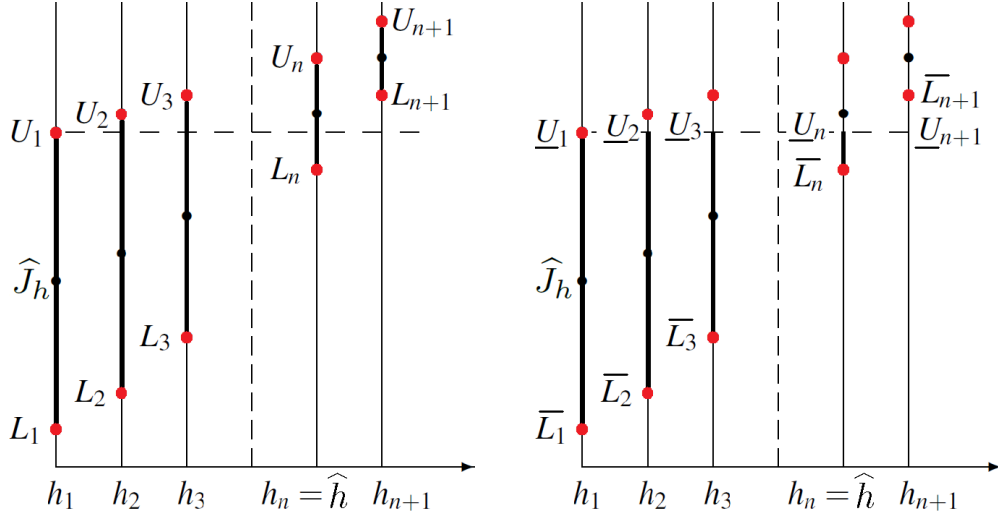


Figure 4.7 – Illustration of the idea and implementation of the ICI rule. Left image : the confidence intervals $Q_i = [L_i, U_i]$ are labelled by thick vertical lines. Right image : the successive intersections, marked by thick vertical lines, are decreasing with the increasing h_i .

This determines the confidence intervals $Q(h)$ of the estimate :

$$Q(h) = \left[\widehat{J}_h(\mathbf{x}) - \Gamma \cdot \sigma_{\widehat{J}_h}(\mathbf{x}, h), \widehat{J}_h(\mathbf{x}, h) + \Gamma \cdot \sigma_{\widehat{J}_h}(\mathbf{x}, h) \right] . \quad (4.21)$$

Denote the sequence of the Q_i as follows :

$$Q_i = Q(h_i) = [L_i, H_i] , \quad h_i \in \mathbf{h} ,$$

where L_i and H_i respectively represent lower and upper bounds of the confidence interval. Eq. (4.21) is equivalent to : $\forall h_i \leq h^*(\mathbf{x}), J_{h_i}(\mathbf{x}) \in Q_i$ holds with certain probability p , related to the threshold Γ . Therefore, for all $h_i < h^*$, the intervals Q_i have a point in common, namely $J(\mathbf{x})$. On the contrary, if the ICI is empty, it indicates $h_i > h^*$. In this way, the ICI rule can be used to test the existence of this common point and to obtain the adaptive window size.

The ICI rule aims at searching for the largest local window size (minimising local variances) where the LPA fits well to the observations (minimising local bias). The estimates $\widehat{J}_h(\mathbf{x})$ are calculated for $h_i \in \mathbf{h}$ and compared. The ICI rule, which uses the estimates and their variances, identifies a scale closest to the ideal one, $\widehat{h} \approx h^*$. Figure 4.7 illustrates graphically the ICI rule. Assuming the intersection with h_{n+1} is empty, the adaptive scale is $\widehat{h} = h_n$.

The following algorithm implements the ICI rule [98, 99] :

1. Define a sequence of confidence intervals $Q_i, \forall h_i \in \mathbf{h}$ as in Eq. (4.21) with their lower bounds L_i and upper bounds U_i .

2. For $i = 1, 2, \dots, u - 1$, let

$$\bar{L}_1 = L_1, \quad \bar{L}_{i+1} = \max\{\bar{L}_i, L_{i+1}\} ;$$

$$\bar{U}_1 = U_1, \quad \bar{U}_{i+1} = \min\{\bar{U}_i, U_{i+1}\} .$$

According to these formulas, \bar{L}_{i+1} and \bar{U}_{i+1} are respectively non-decreasing and non-increasing sequences.

3. Find the largest value i , when

$$\bar{L}_i \leq \bar{U}_i, \quad i = 1, 2, \dots, u ,$$

is still satisfied. Denote this value by n . As was discussed above, the ICI adaptive scale is $\hat{h} = h_n$.

These calculations are point-wise repeated for each \mathbf{x} .

Remark :

- The ICI depends on the estimates $\hat{J}_{h_i}(\mathbf{x})$ giving a centre position of the Q_i and on the width of the interval $\Gamma \cdot \sigma_{\hat{J}_h}(\mathbf{x}, h)$. This thresholding parameter Γ plays an important role in the ICI algorithm. Assuming $\alpha = 0.05$ or 0.01 [98, 99], the theoretical values of Γ are given by :

$$m = 0 , \quad \Gamma = \begin{cases} 3.0 & \alpha = 0.05 \\ 4.0 & \alpha = 0.01 \end{cases} ;$$

$$m = 1 , \quad \Gamma = \begin{cases} 2.7 & \alpha = 0.05 \\ 3.7 & \alpha = 0.01 \end{cases} .$$

In practice, if the signal I is piecewise smooth with rare and slow variations, larger Γ is recommended for better noise reduction ; otherwise, smaller Γ is used to preserve more details of the data.

4.4.2.4 1D denoising example

Figure 4.8 is an example of 1D denoising using the LPA-ICI method. Here we use the LPA estimator of order $m = 1$ with the symmetric Gaussian window. The denoised curve demonstrates that the LPA-ICI filter generally preserves the jumps of signal and smooths the piecewise constant parts. Compared with the noisy free signal, there still exists oversmoothing problems. The root mean square error (RMSE) is 9.073. The bottom row of Fig. 4.8 shows the optimal windows sizes estimated by the ICI rule. We notice that

the ICI rule chooses smaller values at signal's discontinuities and larger ones for the continuous parts. For example, the largest jump in the observed data corresponds with the minimal scale in \mathbf{h} .

Figure 4.9 shows the denoising results of the same noisy signal with polynomials of the order $m = 2$. As expected, the higher order estimation has a relatively smaller RMSE than that in Fig. 4.8. Also, the corresponding computation cost improves largely. Therefore, we use $m = 1$ for the following test. Figure 4.10 provides more details about the anisotropic LPA-ICI algorithm. The optimal right and left scales for the noisy signal are shown on the top two rows. Reconsider the largest jump in observed data, the values of a left Gaussian

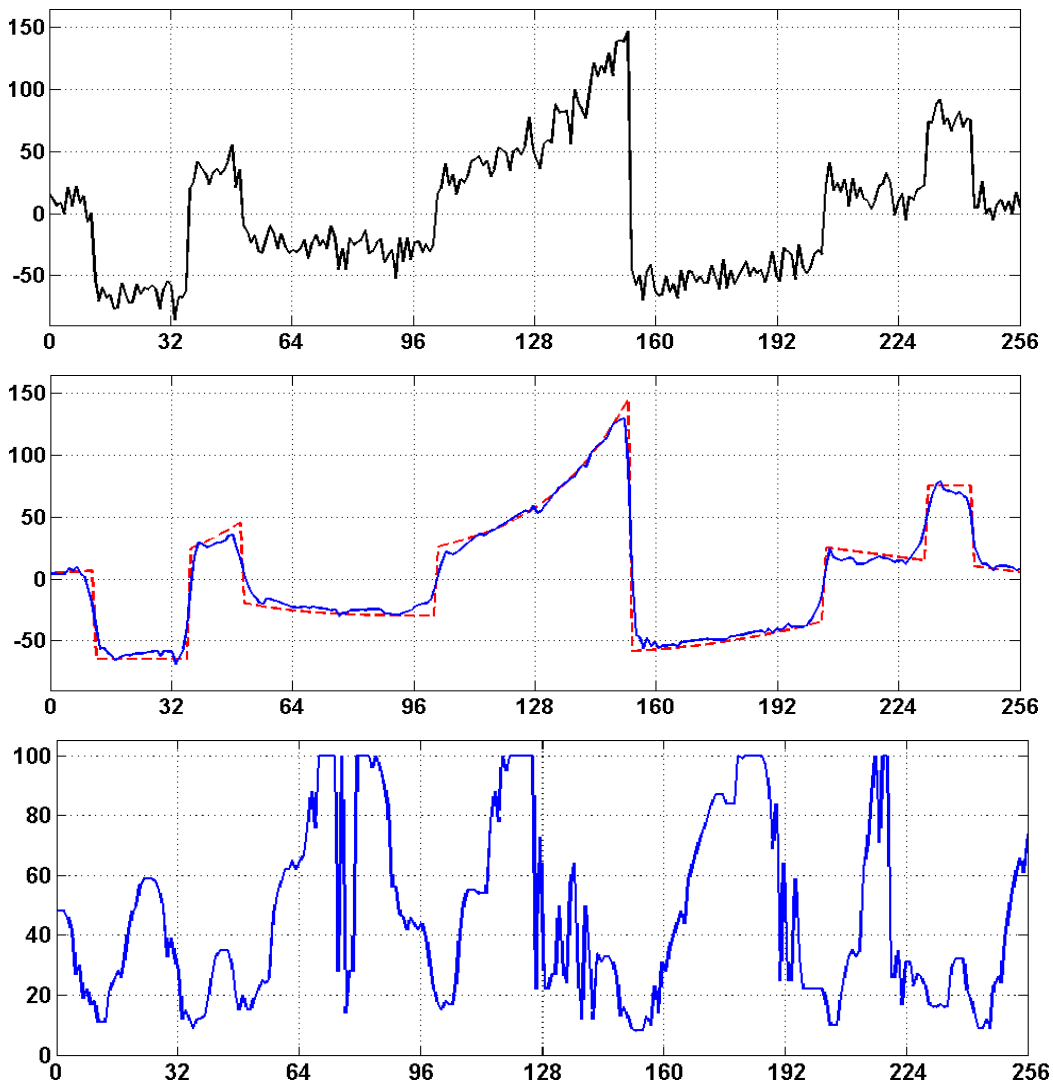


Figure 4.8 – 1D denoising example using the LPA-ICI rule. From top to bottom : the noisy observation ; the noise free signal (red dotted line) and the LPA estimation (blue continuous line) of the order $m = 1$ with the symmetric Gaussian window, while the $\text{RMSE} = 9.073$; the corresponding adaptive window sizes \hat{h} obtained by the ICI rule for $\Gamma = 1$. The set of local windows size is $\mathbf{h} = [1, 2, \dots, 100]$.

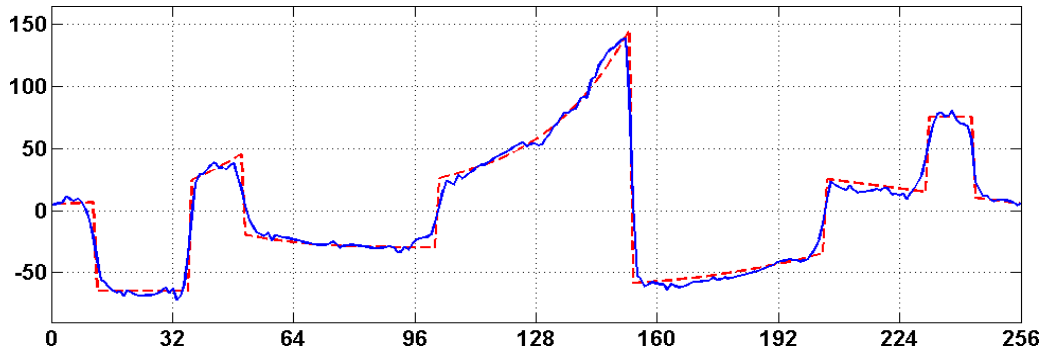


Figure 4.9 – 1D LPA-ICI denoising using higher order $m = 2$. The LPA estimations use symmetric Gaussian window. The RMSE is 8.6956. $\Gamma = 1$, $\mathbf{h} = [1, 2, \dots, 100]$.

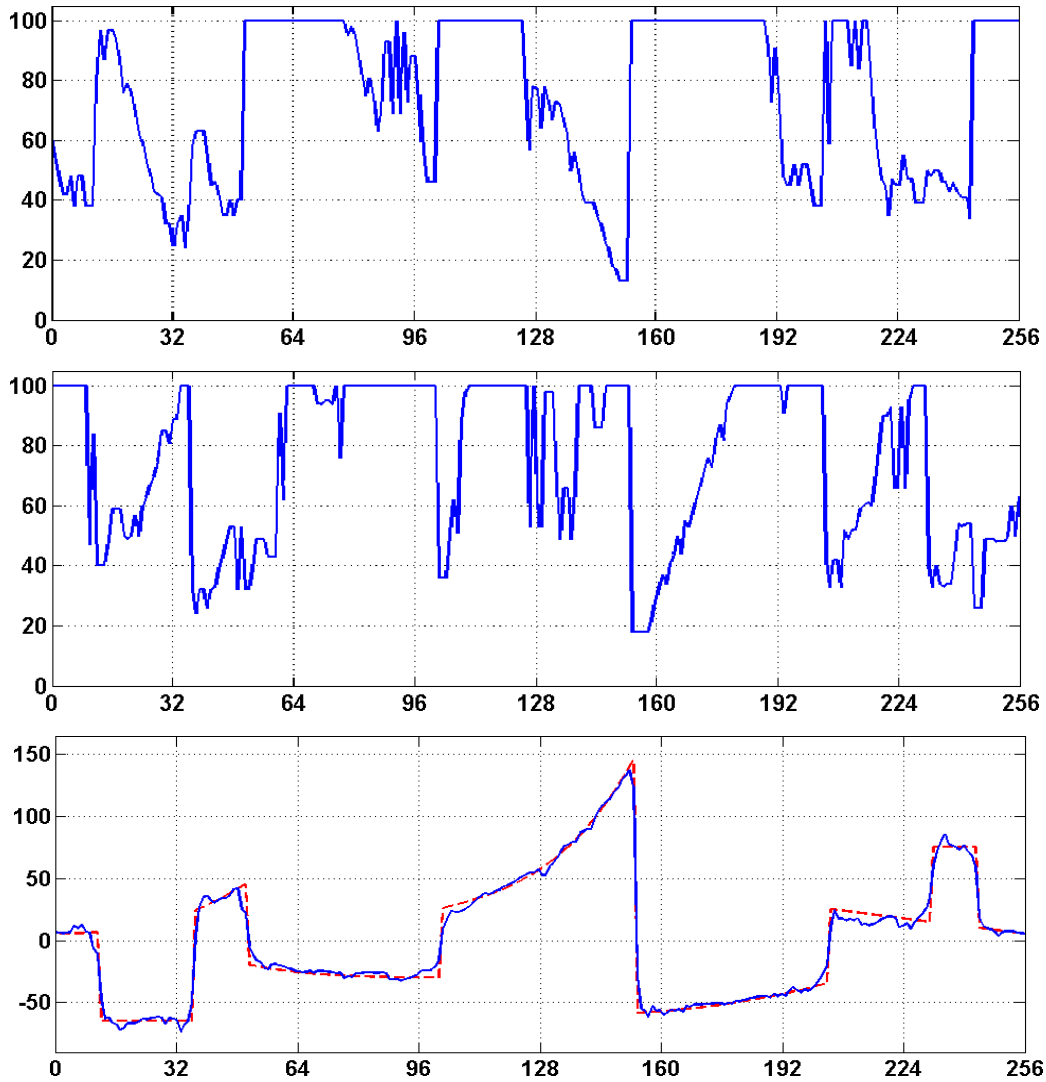


Figure 4.10 – 1D denoising using the anisotropic LPA-ICI approach. From top to bottom : adaptive windows sizes obtained respectively by the right and left Gaussian kernels, and the fused denoising result. $m = 1$, $\Gamma = 1$, $\mathbf{h} = [1, 2, \dots, 100]$, RMSE = 5.8462.

windows decrease for that part, while the right one behaves oppositely. The anisotropic method combines these two kernels sizes in the denoising process, therefore, it leads to a large improvement with a RMSE = 5.8462.

4.4.3 Proposed segmentation algorithm

4.4.3.1 Local region-based segmentation using the LPA-ICI rule

In [210], we have proposed applying the ICI approach to optimise the spatial adaptation for local region-based active contours. For each point, the ICI finds an optimal kernel size that meets the trade-off between the bias and the variance of the LPA. This optimal local scale is then used for the estimation of local image statistics used in the segmentation model.

Suppose we are given a noisy image with intensity inhomogeneities. We define an initial zero level set C , as the red contour shown in Fig. 4.11. Given a finite set of window sizes \mathbf{h} , we calculate g_h for each element. Then utilise the LPA Eq. (4.14) to get the local estimations of the regions inside Ω_i and outside Ω_o , respectively. This means that if a point \mathbf{x} is inside of C , its approximation uses only observed image pixels in $\mathcal{C}(\mathbf{x}) \cap \Omega_i$, and vice versa. As introduced in the previous section, we can calculate the confidence intervals Q_h of these estimations, then apply the ICI algorithm for each point. After that, we obtain the optimal kernel sizes that well balance the trade-off between bias and variances.

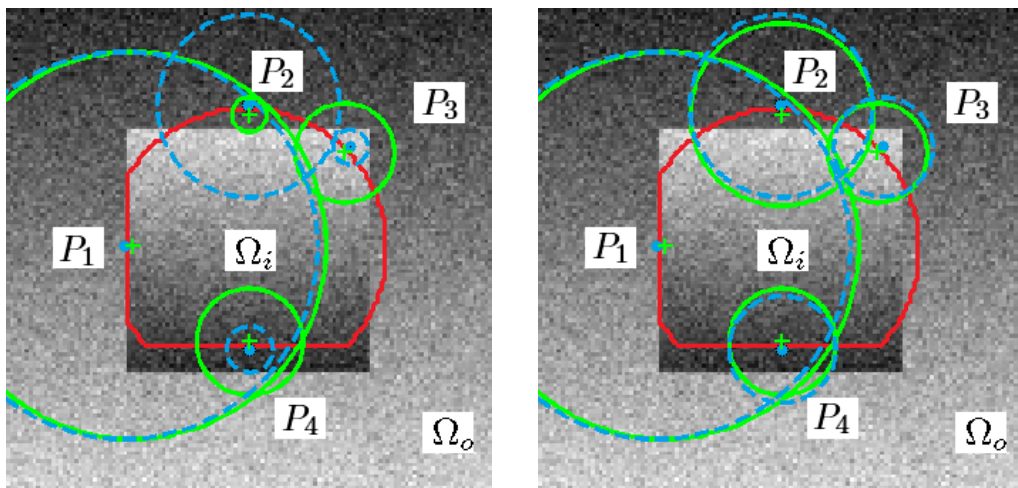


Figure 4.11 – Demonstration of kernel sizes selection. Four pairs of points P_1, \dots, P_4 are studied. For each pair, one point locates inside and the other is outside of C (marked by green + and blue • respectively). The circle centred at each labelled point represents the size of local kernel. Left : scale estimations obtained by the LPA-ICI rule. Right : scale estimations after the maximum filtering operation.

In order to study the relation of these data adaptive scales with the position of the segmentation contour, we picked out several typical points for analysis. As we are only interested in a narrow band of C , within which we select four pairs of neighbours P_1 to P_4 . For each pair, one point locates inside and the other is outside of C , marked with green '+' and blue '•' respectively in the left image of Fig. 4.11. The corresponding estimated scales are illustrated by the sizes of circles, shown in the same figure.

- The leftmost pair P_1 is around a region with very low contrast between Ω_i and Ω_o , where the local region statistics for inside and outside are very similar. Also the contour near P_1 is the correct boundary, where locally the segmentation has been achieved. In order to maintain this partition, we tend to consider more image information, which corresponds to the large kernel size obtained by LPA-ICI algorithm.
- For the pair P_2 around the top of C , the inside one, laying between C and the true boundary, has a small kernel size. This is expected as larger windows, in that position, will introduce greater estimation bias. However, its symmetric point has larger scale estimates, because the image is relatively homogeneous in this neighbouring region within Ω_o .
- The pairs P_3 and P_4 are laying on the foreground. Thus, they have larger window size inside and smaller one outside, which are opposite to P_2 .

Therefore, if we directly use these kernel sizes \hat{h} in the segmentation algorithm, as the curve C evolves closer to the real boundary, the local regions of points between them should be decreased, and so will be the estimated local scale. This brings out the problem that the closer C is to the correct segmentation, slower the evolution speed is. Analysing the case P_2 (or P_3), the spatial scale for the local inside (outside) need to be at least as big as the outside (inside), in order to increase the force driving the segmentation process. To overcome this problem, we smooth the estimated local scales \hat{h} inside and outside of C respectively, and run a max filter of a small size, 3×3 for example. So for the points near C , their estimated scales have similar values. Indeed, the estimated scales are very appropriate as it can be seen on the correct segmentation of P_1 . This filtering operation is necessary only when the algorithm is in progress. For the purpose of maintaining the accuracy, we run a few iterations by replacing the maximum with an average filtering and then by using the estimated scales directly.

As a summary, the proposed segmentation method using adaptive windows sizes selected by the LPA-ICI algorithm has following basic steps :

1. Initialisation : Give an image I , an initial segmentation C_0 or ϕ_0 , a finite set of win-

dow sizes $\mathbf{h} = \{h_i, i = 1, 2, \dots, u\}$, a vector of 2D polynomials $\boldsymbol{\psi}$, a threshold Γ and the weights of internal and external energies for the local region-based segmentation.

- (a) Estimate the noise variance $\hat{\sigma}^2$ from the observed image⁸.
 - (b) For each $h \in \mathbf{h}$, build the set of linear filters g_h for the LPA.
2. Spatial kernel size estimation by the LPA-ICI algorithm : Consider the pixels \mathbf{x} within a narrow band of the current segmentation C .
- (a) For the inside points $\mathbf{x} \in \Omega_i$ and the outside points $\mathbf{x} \in \Omega_o$ respectively, calculate the LPA estimation $\hat{J}_h(\mathbf{x}), \forall g_h$.
 - (b) According to Eq. (4.21), determine the lower bounds L_i and upper bounds U_i of the confidence intervals Q_i for the estimation $\hat{J}_{h_i}(\mathbf{x})$. Loop on i , update the bounds of intersections. Test the existence of the ICI, and get the adaptive window sizes $\{\hat{h}(\mathbf{x}), \forall \mathbf{x}\}$.
 - (c) For the inside and the outside regions, smooth the obtained $\hat{h}(\mathbf{x})$ respectively. When the algorithm is in process, run a maximum filtering locally for all the smoothed $\hat{h}(\mathbf{x})$; otherwise, use an average filtering for few iterations, then use directly the smoothed $\hat{h}(\mathbf{x})$.
3. Local region-based segmentation : Compute the internal energy of C , and the external energy, for example, proposed by Brox and Cremers Eq. (3.5).
- (a) For all \mathbf{x} , their optimal neighbourhoods $\mathcal{O}(\mathbf{x})$ are defined by $\hat{h}(\mathbf{x})$. Calculate the local image statistics by the ML estimation for $\Omega_i \cap \mathcal{O}(\mathbf{x})$ and $\Omega_o \cap \mathcal{O}(\mathbf{x})$ regions.
 - (b) By the obtained local region statistics, the external energy is calculated. Together with the internal energy, update the contour C .
4. Repeat steps 2 and 3 until convergence.

The proposed method utilises an adaptive size of the local kernel at every image location. Thus, it combines the advantage of using local region statistics with the consideration of relatively global information.

4.4.3.2 Segmentation examples and discussions

Figure 4.12 shows the segmentation of three images with inhomogeneities obtained using the proposed scale selection strategy. As expected, our segmentation method leads

⁸. The noise variance may be estimated respectively for the regions inside and outside of the current segmentation, and be updated after a fixed number of iterations.

to very satisfactory results. The values of colour maps correspond to the dynamically selected local kernel sizes. Notice that the estimated window sizes for the local inside are smaller than those for the local outside for all three images. This can be explained by the fact that the inhomogeneity in Ω_i is relatively stronger than in Ω_o . This difference of scales, between Ω_i and the Ω_o , is important for the forces in competition around low contrasted boundaries.

In order to further consider the influence of the noise level on the estimation of the spatial kernel size, we use a synthetic image and study the LPA-ICI behaviour on two pairs of points. A number in '1' to '4' is assigned to each point as shown in Fig. 4.13.

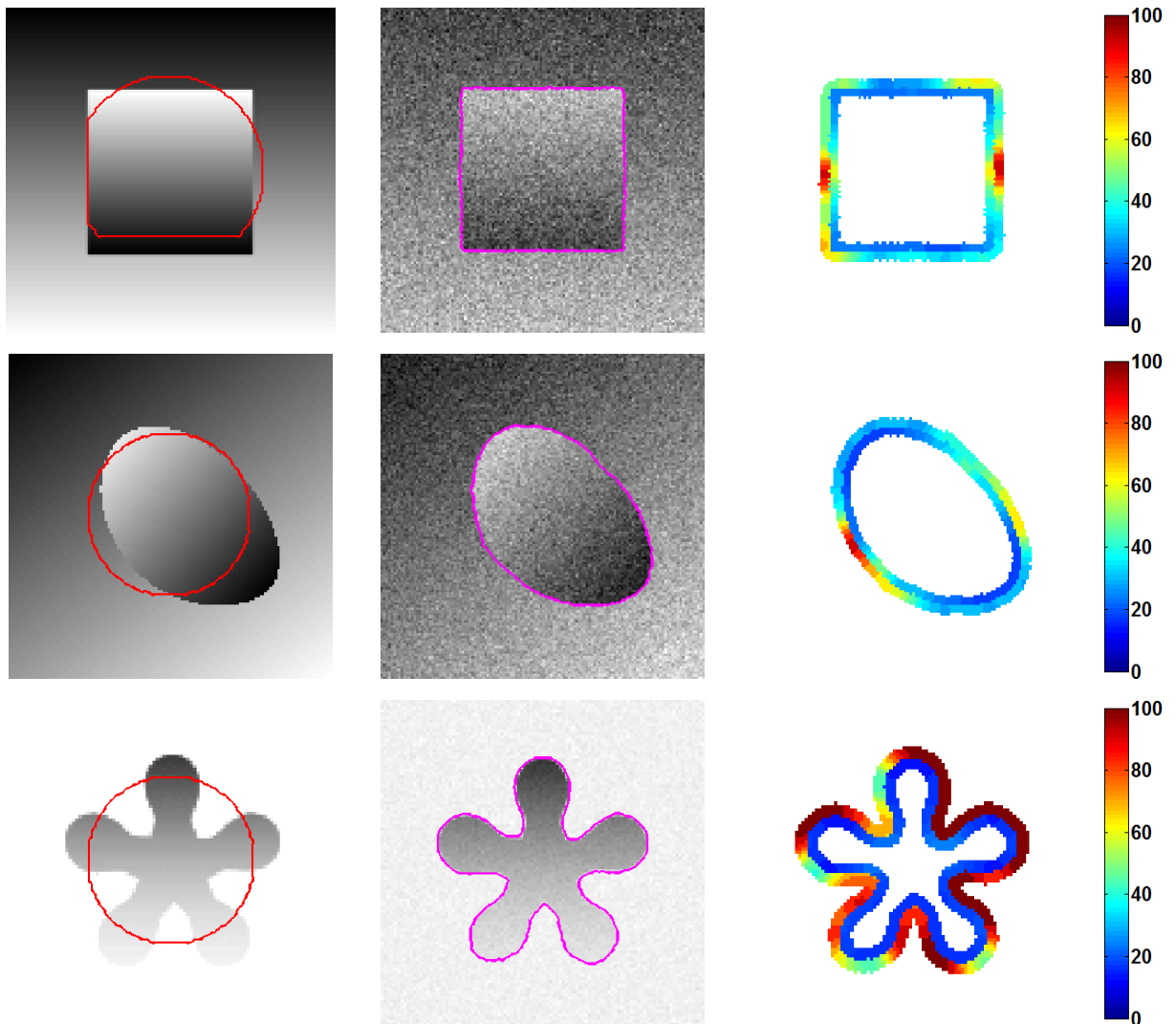


Figure 4.12 – Segmentation example of images with inhomogeneities using the proposed method. From left to right : noise free images with initialisations, noise degraded images with segmentation results and the estimated kernel sizes for the final contour. The size of three images is 128×128 , and the local optimal scales are selected from the same \mathbf{h} used in Fig. 4.4.

The study is carried out for the special case of an ideal segmentation, in other words, we discard the influence of bias estimation. In order to obtain statistically meaningful estimations, we run the experiment 20 times and for 7 different SNR values. The means and the standard deviations, calculated with the 20 estimated kernel sizes, are visualised as error bars versus decreasing SNR values on Fig. 4.13, one curve for each point.

We observe that the kernel sizes for these estimations are inversely proportional to the SNR values. It implies that, when the image noise increases, the corresponding optimal kernel size also increases, and the proposed segmentation method tends to be more global. We also notice that the scales of the inside point ‘1’ are always smaller than those of the outside point ‘2’. But point ‘3’ and point ‘4’, in the regions with low contrast between foregrounds and background, have similar kernel size for SNR values lower than 16dB.

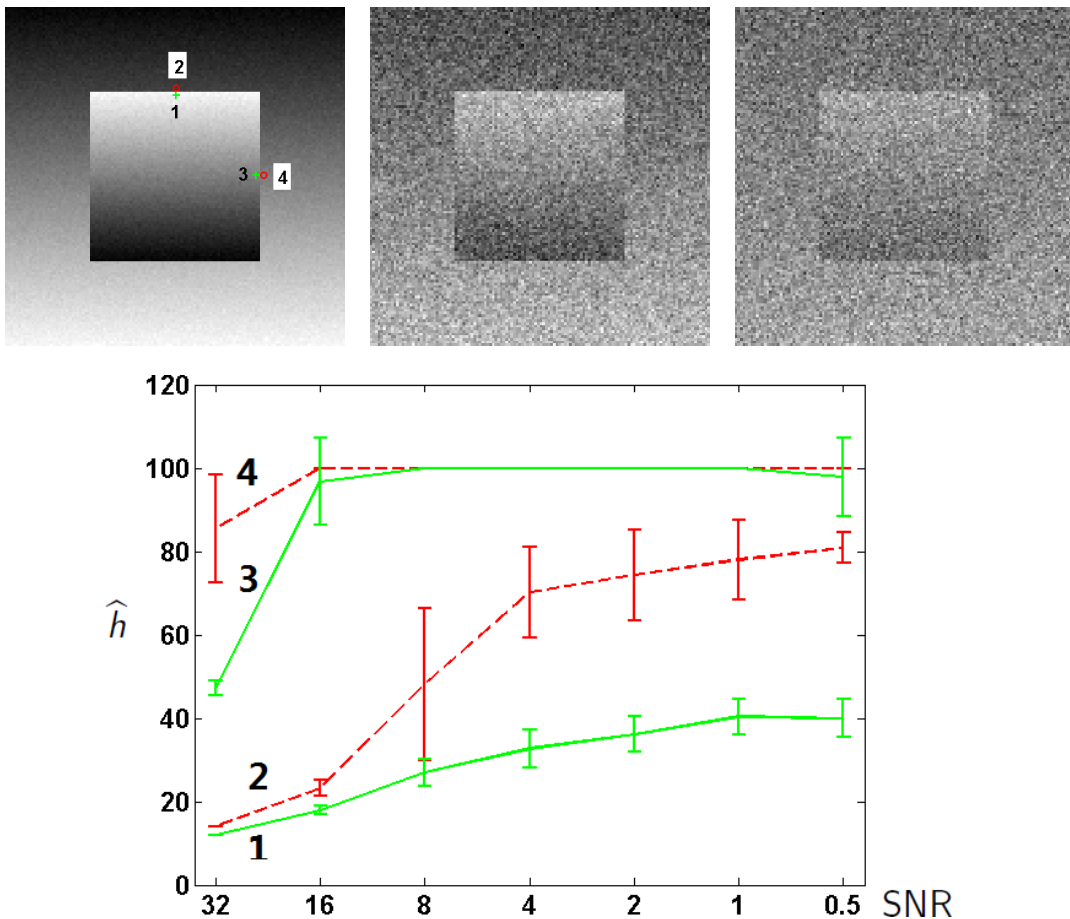


Figure 4.13 – Influence of the noise level on the estimation of local scales. Top : noisy image with SNR = 32dB, 8dB and 4dB. Point ‘1’ and ‘3’ (green +) belong to the foreground, and point ‘2’ and ‘4’ (red o) belong to the background. Bottom : the plot shows the estimated kernel sizes versus the image SNR values. The error bars are drawn from 20 repeated experiments when $\Gamma = 2.2$. The numbers ‘1’, ‘2’, ‘3’, ‘4’ on the left side of each curve represent the point number shown in the top image. Image size is 128×128 , and \mathbf{h} is the same set used in Fig. 4.12.

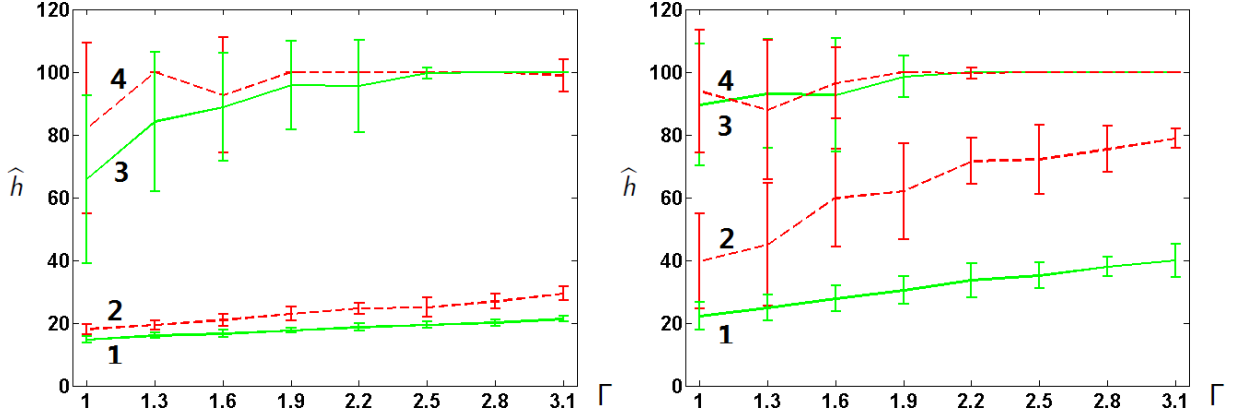


Figure 4.14 – Influence of Γ on the estimation of local scales. The plot shows the estimation kernel size versus the Γ values. The error bars are drawn from 20 repeated experiments. Each curve represents the estimated kernel sizes for a point shown in Fig. 4.13. Left : SNR=16dB. Right : SNR=4dB. \mathbf{h} is the same set used in Fig. 4.12.

The role of the threshold parameter Γ is to define the reliability of the adaptive estimate $\hat{J}_{\mathbf{h}}$. At first glance, it may seem that Γ should be as small as possible, so as to minimise the risk of the adaptive-scale estimate. However, a too small Γ makes the probabilities of the confidence intervals too small to have any practical significance. In order to study the effects of Γ on the estimated local windows sizes, we do a similar test to the one shown in Fig. 4.13 for the same labelled points. Figure 4.14 illustrates that the estimated kernel sizes are proportional to the values of Γ . For both noise levels, the estimated scales for the outside points (red dotted curves) are generally larger or equal to their corresponding inside ones (green continuous curves), which corresponds our former discussions. However, when the inside and outside regions have very low contrast, here points ‘3’ and ‘4’, the estimations for $\Gamma = 3.1$ for SNR = 16dB and at $\Gamma = 1.3$ for SNR = 4dB do not follow the others patterns. Therefore, when the image noise is less important, we tend to use a smaller threshold Γ in order to increase the sensitivity of the ICI rule. On the contrary, if the noise is very important, a larger Γ should be used in segmentation.

Finally, we compare the behaviour of the proposed automatic scale selection algorithm with the Piovano and Papadopoulo’s method. Figure 4.15 shows the contour evolution and the estimated scale maps. In the first column, both $\hat{h}(\mathbf{x})$ for the initial contour reflect clearly the degradation of image intensity. From the values of local kernels shown by the colour maps, we observe that the Piovano and Papadopoulo’s method initially gets higher scales, and then uses smaller size when the algorithm approaches to convergence. In this method, the evolution speed is small when C is in an homogeneous region, thus large $\hat{h}(\mathbf{x})$ are selected ; while C approaches the ideal boundary, $\hat{h}(\mathbf{x})$ decreases in order to keep the

same evolution speed ξ ; once C reaches the boundary, all the $\hat{h}(\mathbf{x})$ are almost equal to the smallest value in the set \mathbf{h} . For the proposed algorithm, $\hat{h}(\mathbf{x})$ aims to well balance the bias-variance trade-off. When \mathbf{x} belongs to an homogeneous region, local image statistics of its neighbours are very similar, thus larger $\hat{h}(\mathbf{x})$ are obtained by the LPA-ICI algorithm. Here, $\hat{h}(\mathbf{x})$ defines the optimal region that represents well the image statistics at point \mathbf{x} .

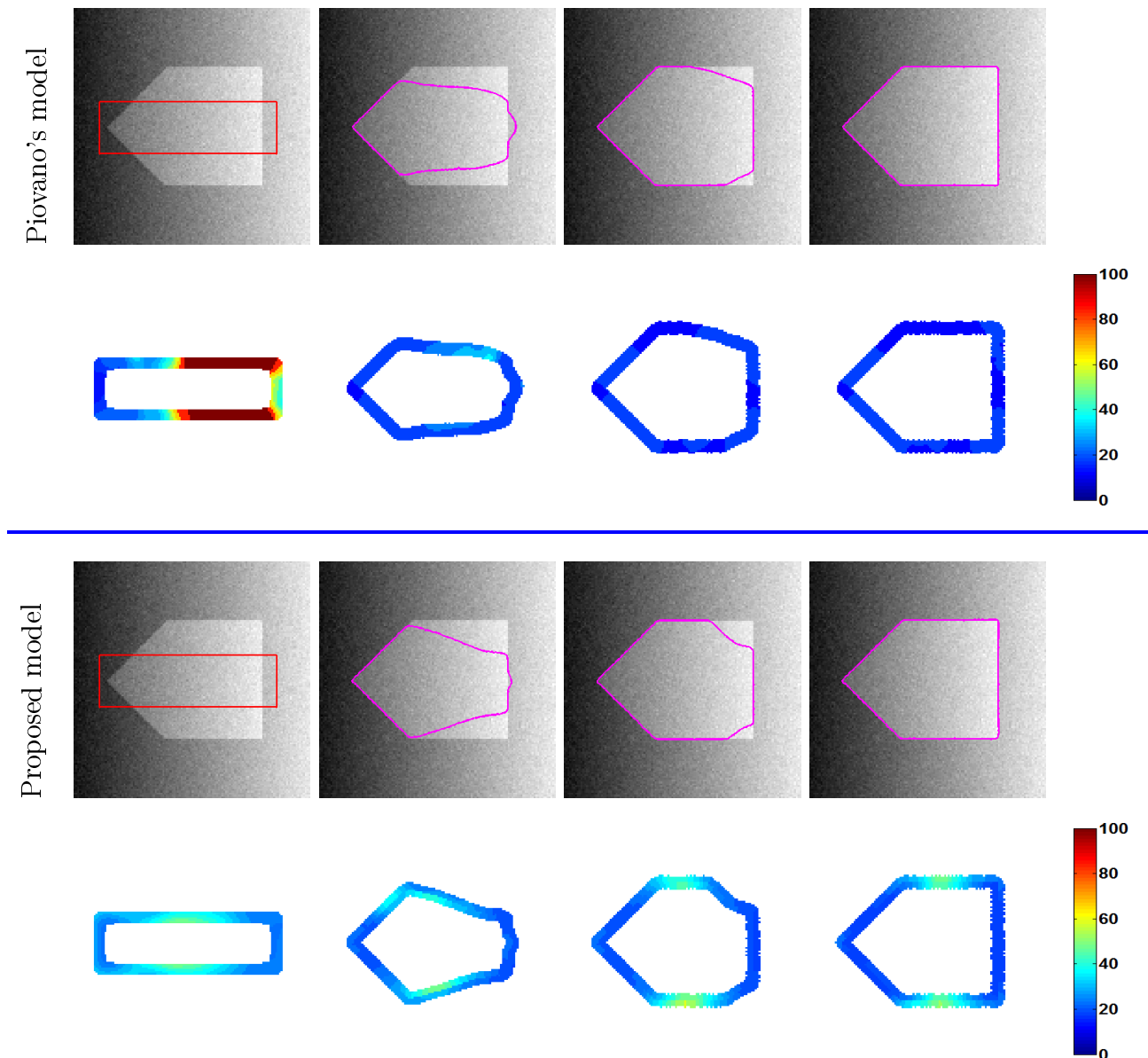


Figure 4.15 – Comparison of the behaviour of two scale selection strategies. Top two rows : Piovano's model [163], $\varepsilon = 0.5$. Bottom two rows : the proposed one [209], $\Gamma = 2.5$. From left to right : the curve evolution from the initial contour to the final contour with the corresponding estimated \hat{h} . Image size 128×128 , \mathbf{h} is the same set used in Fig. 4.12.

4.5 Conclusion

In this chapter, we discussed possible solutions for two problems in the local region-based segmentation. We have recalled the denoising algorithms which have similar difficulties. We reviewed three segmentation models, which make use of both global and local image statistics. Then, we proposed a local region-based segmentation method with adaptive kernel scales within the level set framework. These optimal scales, derived by the LPA-ICI rule, are determined respectively for interior and exterior regions around the segmentation contour. Through some segmentation examples of synthetic images, we found that the proposed method is quite promising in the segmentation of images with inhomogeneities. More experiments and further analysis will be presented in the following chapter.

Ultrasound image segmentation

Chapter summary

This chapter will first review the methodology of ultrasound image segmentation. We will present the development of segmentation algorithms, in the consideration of ultrasound physics and prior information. Then, a more rigorous analysis of our proposed segmentation method will be given. We will use comparative experiments to verify the interest of our contribution. Complete analysis on these results will be demonstrated. Finally, we will provide some application examples on segmentation of real medical images.

Contents

| | |
|--|-----------|
| 5.1 Introduction | 80 |
| 5.2 State of the art on ultrasound image segmentation | 81 |
| 5.2.1 Statistics of speckle | 81 |
| 5.2.2 Prior information | 82 |
| 5.3 Justification of our approach | 84 |
| 5.4 Experiments and discussion | 85 |
| 5.4.1 Simulated ultrasound images | 86 |
| 5.4.2 Echocardiographic images | 95 |
| 5.4.3 CT images | 96 |
| 5.5 Conclusion | 96 |

5.1 Introduction

Medical ultrasonography is a non-invasive imaging technique used for the visualisation of subcutaneous body structures, and has steady progresses in the last decades [30, 194]. It helps the diagnosing process and is involved in all stages of disease treatment. Segmentation, quantification and analysis of ultrasound images could ultimately improve the comprehension of diseases, the early detection of degradations and the interventional therapy. In a standard ultrasound system, there are three basic types of data available for analysis [145] : radio-frequency (unprocessed) signals, envelope (magnitude) detected signals, and B-mode (log-compressed) images. In this study, we will focus on the segmentation of ultrasound B-mode images, because B-mode ones are traditionally available on commercial ultrasound systems.

Ultrasound image segmentation, largely driven by clinical needs, is a particularly challenging task. The echography has advantages in studying the function of moving structures in real-time. However, its segmentation result is strongly influenced by the quality of the acquired data [146]. Ultrasound B-mode images are known to have a low SNR, a low contrast between areas of interest and high amounts of speckle. Furthermore, the presence of characteristic artefacts, such as non-linear attenuation, shadows and signal dropout, also complicate the segmentation task. Finally, the orientation dependence of acquisition can result in missing boundaries [146]. Therefore, the appearance of geometric boundaries in ultrasound images is dependent on the acoustic impedance difference between tissues and on the above mentioned factors. Thus, conventional segmentation methods, which assume strong-intensity edges, often perform poorly on ultrasound images. Facing with this problem, numerous studies have been carried out [181, 146, 145]. These methods can be broadly defined in terms of those that make use of imaging physics constraints and those that make use of anatomical shape or temporal constraints.

In the rest of this chapter, we will first briefly recall used intensity models for the speckle noise. Then we will review several ultrasound image segmentation methods in consideration of prior constraints, such as intensities, phase, texture and shape. After that, we will give the justification of the proposed local region-based method with the scale selection strategy. In order to demonstrate the usefulness of our approach, segmentation results on simulated and real ultrasound images will be presented. We will further analyse its performance in comparison with several previously introduced segmentation methods based on local image statistics. Finally, we will present few results when applied on CT images.

5.2 State of the art on ultrasound image segmentation

5.2.1 Statistics of speckle

Speckle is caused by the backscattered echoes of either randomly or coherently distributed scatterers in the tissue. It gives the granular texture appearance of ultrasound images. This signal dependent effect has been well studied in ultrasound-based imaging. The speckle can be seen either as a noise introduced by the sensor or as a signal carrying some information about the observed tissues. Regarding the former, there exist an extensive literature on speckle reduction. Recent works include [57, 225, 217, 1, 62, 215]. This denoising step can be considered as a preprocessing step before performing segmentation. In the latter, speckle is used as a valuable information and is used as a feature in order to separate different tissues.

The statistical properties of the received echo signal depend on the density and the spatial distribution of the scatters [195]. A suitable model of the observed speckle is useful not only for segmentation, and several distribution families have been proposed in the literature [58, 141, 145, 55]. When there is a large number of randomly located scatterers, known as the case of fully developed speckle, the statistics of the envelope signal follow a Rayleigh distribution [195, 33]; if there is an additional non-random coherent component in the echo signal, the Rice distribution is an appropriate model [195]. Both models suppose the presence of a large number of scatterers in the tissue. In practice, the effective number of scatterers is finite, thus the K -distribution is proposed for this case of partially developed speckle [90, 180]. More generalisations, namely the homodyned K -distribution [56, 166], the Nakagami distribution [179], the Gamma distribution [12] and the Rician inverse of Gaussian distribution [62], have been proposed for different scattering conditions. A recent critical review of most existing models is provided in [55]. The work of Nillesen et al. on modelling envelope statistics of blood and myocardium for the segmentation of echocardiographic image is also of interest [144].

As it has been already pointed out by several researchers, for instance in [123, 146, 22], it is important to highlight that all these statistical models only give the speckle probability density function at the transducer output. Meaning that the models are valid only for the unfiltered envelope of the received RF signal (i.e. before interpolation, log-compression and Time-Gain-Compensation). Thus, the validity of such models on ultrasound images acquired under clinical conditions is questionable [123, 188, 223]. Empirical models of speckle in clinical log-compressed images have been reviewed and compared in [188].

5.2.2 Prior information

The resolution of ultrasound B-mode images is quite poor, in comparison with other clinical imaging techniques. In addition, ultrasound images have the problem of missing boundaries. Therefore, the utilisation of prior knowledge is a good way to characterize the object of interest, and helps solving the segmentation problem of ultrasound images. Here, we will briefly introduce three main categories of constraints [146, 145] : the intensity-based, the geometric and temporal priors.

1. Intensity derivatives : Similar to edge-based segmentation method, this prior is appropriate if the goal is to find acoustic (impedance) discontinuities in ultrasound images. As speckle gives a strong gradient response, intensity derivatives methods work only at high SNR observations. Therefore, speckle reduction techniques are usually necessary [159]. Some specific edge operators, which take into account the presence the multiplicative nature of speckle noise, have been proposed (see eg. [218]). This constraint works well when there is a strong boundary between different tissues. One of its limitations is caused by the anisotropy of ultrasound image acquisition. In real images the object of interest usually has missing edges.
2. Phase information : As a robust alternative to intensity gradient, the local phase has been proposed for acoustic boundary detection in [138]. The most important advantage of this method is its theoretical contrast invariance. Therefore, it is in principle robust to attenuation. Generally, phase is estimated by means of a quadrature filter bank [21]. Recently, phase information has attracted a lot of interest and an increase of its application in the processing of ultrasound images is observed. See for instance [15, 14] for recent examples of image segmentation within the level set framework.
3. Grey level distribution : As introduced earlier, various intensity distributions can be employed to describe the speckle in the envelope signal. The Rayleigh model has been popularly used in segmentation, for example it is incorporated into the level set framework in [175, 22]. The Gaussian [23, 123] and the Gamma [188] distributions have also been applied for the segmentation of ultrasound images. This parametric pdf constraint works well for region-based methods. Global model parameter estimation decreases the robustness as it ignores effects such as signal attenuation, shadowing and signal drop-out.
4. Image texture : Texture analysis methods have been proved capable in the extraction of relevant ultrasound image characteristics, and have been utilised in

segmentation methods with some success [140, 82, 23, 154]. However, this constraint is intrinsically a descriptor of the microstructure of the observed tissue and the imaging system. Thus, different system parameters lead to different texture patterns and the true characterisation of physical properties of tissues is still an issue. Texture characterisation is also strongly limited to the chosen spatial scale. Therefore, multi-resolution approaches are commonly considered [140, 146].

The above mentioned intensity-based priors generally use the features extracted from the given ultrasound image, which are often insufficient for a reliable segmentation. Therefore, geometric and temporal information are often introduced to improve segmentation results.

5. Shape : Such constraint can be embedded in segmentation algorithms in several forms. To our knowledge, the shape constraint used in ultrasound image is first given by a parametric shape in [87]. With this prior, one major problem in segmentation is how to choose a general model, which is valid for all objects even those with pathological tissues. Thus, the shape information is commonly obtained from a training process [89, 48, 77]. Alternatively, the shape prior may be defined simply as a boundary regularisation, which corresponds to the internal energy in active contour methods. The shape information can be represented explicitly as a point distribution model [49], or implicitly as a signed distant transform [115]. Note that the shape constraint is only as good as the training samples from which it was built and the chosen shape-space model framework. Also, texture and shape information can be combined in a single model, known as the Active Appearance Models (AAM) [135].
6. Motion : Since ultrasound is a real time imaging modality, it is useful to consider the temporal information in segmentation when available. The segmentation solution may simply require global [39] or local [176] temporal coherence. Image segmentation can also be formalised as a motion estimation problem. Typical examples are using optical flow estimation [134] or block matching velocity estimation [25]. More complex models exist in the literature, which extend the AAMs to include motion, namely the Active Appearance Motion Models (AAMM) [20].

In practice, a number of image segmentation methods combine two or more of the above mentioned constraints. Here, the review and organisation is not an exhaustive list of all forms of priors that appeared in the image segmentation literature. We may for example use the incompressibility constraint on echocardiographic image segmentation [223], the volume conservation constraint [71] or the statistical overlap constraint [11].

5.3 Justification of our approach

The segmentation of images with intensity inhomogeneities is quite a challenging problem. Our main objective is to provide an acceptable solution to these degraded images, such as the attenuation problem in ultrasound images. In order to well segment these images, there exists many methods that take the advantage of prior information. According to the findings in the previous section, these prior constraints can overcome some difficulties, like the low contrast and missing boundaries. For instance, a statistical model, which exploits knowledge of image formation, has been proposed for magnetic resonance images [200] and then adapted for ultrasound images segmentation [206]. The underlying model can simultaneously enhance image contrast and help the segmentation. In this work, we focus on studying the external energy, and use a length term as an internal constraint for regularisation. The combination of other prior information is beyond the scope of our current study.

We mainly concentrate on handling the segmentation of images with intensity inhomogeneities using local region-based methods. Indeed, segmentation methods based on global image statistics are known to fail on this type of data, mainly because of the intensity inhomogeneities. Region-based methods using local image statistics have better results. Through our study presented in Chapter 3, it is clear that the size of the spatial window appears to be important for local methods. Therefore, in order to build a more robust model to handle images with intensity inhomogeneities, we have proposed to use a pixel-dependent adaptive local scale. More specifically, this scale value is defined using the LPA-ICI scale selection strategy conditional on the current segmentation. From the segmentation examples in Chapter 3, we have found out that the method using optimal locality leads to better results than applying a single scale.

Note that the LPA method assumes an additive Gaussian noise for the observed image. This assumption is not valid in practice, for example for displayed ultrasound data. However, some literature [8, 23] takes the advantage of the Central Limit Theorem, which states that the average of a large number of random variables must tend toward a Gaussian distribution around their collective mean. This proposition is reasonably acceptable for low-pass filtered and decimated images that are originally governed by non-Gaussian statistics [8, 23]. Alternatively to the multi-resolution implementation used in [8, 23], our approach is based on local region statistics with optimal window sizes. The proposed segmentation model can be implemented very efficiently using recursive Gaussian filtering [164, 31], although its performance may decrease when the local Gaussian approximation is violated.

5.4 Experiments and discussion

In this section, we will test the previously introduced segmentation algorithms based on local image statistics. Within the level set framework, we will use six models from two categories, which include⁹

i) Local region-based methods with a single scale

- (a) the straightforward local Gaussian model : Brox and Cremers [32], § 3.2, Eq. (3.5),
- (b) the local intensity fitting energies : Wang et. al [196], § 3.3, Eq. (3.11),
- (c) the local intensity fitting energies with $\sigma_p \gg \sigma_e$: proposed in § 3.5.2, Eq. (3.21),
- (d) the local intensity fitting with a bias correction technique : Li et. al [119], § 3.4, Eq. (3.15);

ii) Local region-based methods with adaptive scales

- (e) Piovano and Papadopoulo's scale selection strategy [163] : § 4.4.1, Eq. (4.10),
- (f) our scale selection strategy based on the LPA-ICI rule : proposed in § 4.4.3.

We will present comparative experiments of these methods on images with intensity inhomogeneities. To this end, the results will be compared qualitatively and quantitatively. For the latter one, we will use two distance measures, namely the Dice Similarity Coefficient (DSC) and the Mean Average Distance (MAD). The DSC is defined as :

$$\text{DSC}(S, S_{true}) = 2 \frac{|S \cap S_{true}|}{|S| + |S_{true}|} , \quad (5.1)$$

where S and S_{true} represent the segmentation and the true boundary respectively. The closer the DSC values to 1, the better is the segmentation. The MAD computes the average distances between two curves C_1 and C_{true} , which are described as a set of points $C_1 = \{a_1, a_2, \dots, a_n\}$ and $C_{true} = \{b_1, b_2, \dots, b_m\}$. The distance between a point a_i and its nearest one on C_{true} is calculated by :

$$d(a_i, C_{true}) = \min_{b_j \in C_{true}} \|b_j - a_i\| .$$

These distances are averaged for all the points of the two curves. Thus, the MAD of C_1 and C_{true} is given by :

$$\text{MAD}(C_1, C_{true}) = \frac{1}{2} \left[\frac{1}{n} \sum_{i=1}^n d(a_i, C_{true}) + \frac{1}{m} \sum_{j=1}^m d(b_j, C_1) \right] . \quad (5.2)$$

⁹. In all subsequent experiments, we will refer to these local region-based segmentation algorithms by method (a) to (f).

5.4.1 Simulated ultrasound images

First, we will show experiments on realistic ultrasound simulations. To this end, we have used the simulation program Field-II [94, 93], to synthesize phantom data with known ground truth. A linear scan of a first phantom (PH1) was done with a 290 elements transducer using 64 active elements. The scatterers in the phantom were randomly distributed within the phantom of $80 \times 80 \times 15$ mm cube size. The scatters amplitudes follow a Gaussian distribution with different standard deviations for each homogeneous tissue. A single transmit focus was placed at 70 mm, and receive focusing was done at 10 mm intervals from 30 mm from the transducer surface. 128 lines were simulated at 5 Mhz. The second phantom (PH2) of size $100 \times 100 \times 15$ mm cube was placed at 10 mm depth from the transducer surface, and was scanned with a 7 MHz 128 elements phased array transducer. A single transmit focus at 60 mm from the transducer was used, and focusing during reception is at 10 to 150 mm in 1 mm increments. The images consist of 128 lines with 0.7 degrees between lines. Hanning apodisation in transmit and receive was used in all experiments. Three levels of tissue attenuations were simulated for both phantoms. We also used different dB ranges for the envelope log compression to simulate different image contrasts.

For the following experiments, we use the weighted length term $\nu|C|$ as the internal energy, where $\nu = 650$ for method (c) and $\nu = 2$ for all the other segmentation models. The maximal time step Δt is set to 0.2. For the Heaviside function, we use the approximation given by Eq. (2.30) with $\varepsilon = 0.7$. For method (e) and (f), the set of local windows sizes is $\mathbf{h} = [12, 14, 16, 18, 20, 22, 24, 27, 30, 33, 36, 40, 44, 48, 53, 58, 64, 70, 77, 84, 92, 100]$. We will test on 60 simulated ultrasound images of size 192×192 with 3 different initialisations.

i) Single scale methods

Figure 5.1 shows the behaviour of the BC model (method (a)) when different sizes of the local spatial kernel and different initialisations were used. Notice the low contrast between tissues, the speckle and the attenuation in these simulated ultrasound images. This experiment clearly shows that the size of the local spatial kernel σ_p affects the segmentation. When using a very large scale value, the top row in Fig. 5.1, the algorithm's behaviour is similar to the global method. For $\sigma_p = 70$, this method is quite robust to noise (ini. 2) but can not deal with the weak boundary (ini. 1) and the attenuation (ini. 3). As expected, the smaller scales $\sigma_p = 20, 12$ lead to satisfactory results. Notice that for the first initialisation, $\sigma_p = 20$ performs poorly at a part of the inside boundary. Small

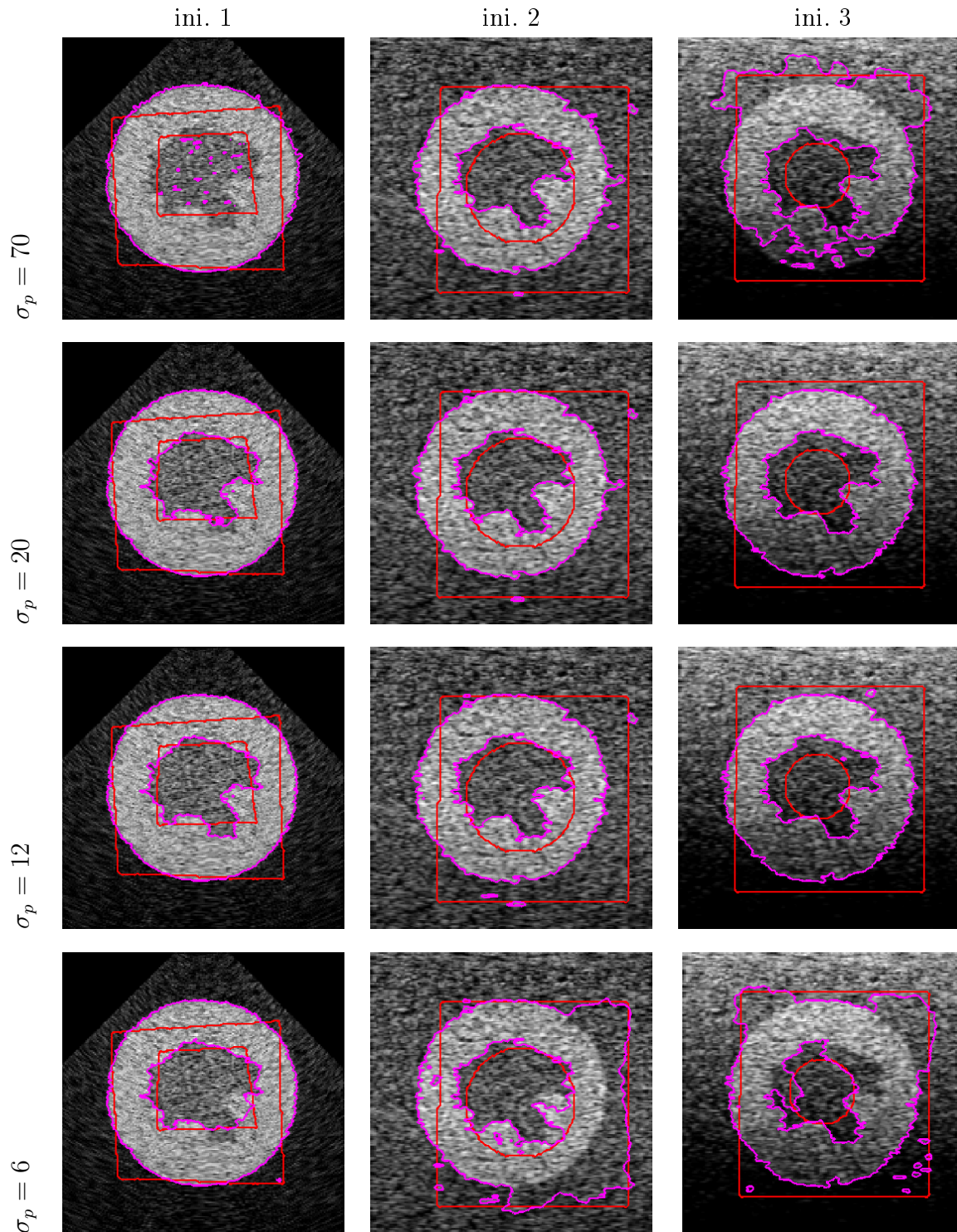


Figure 5.1 – Segmentation results of the BC model (method (a)) on simulated ultrasound images with 3 different initialisations. From left to right column : images ‘PH1_45dB’, ‘PH2_35dB’ and ‘PH2_ATT_60dB’. Here, ‘45dB’ means a range of 45dB is used in log envelope compression. ‘Att’ means with images with attenuation simulation. $\nu = 2$.

local scales generally decrease the capture range of the active contour and increase the number of local minima. This is the case, for example, for the results of the last row when $\sigma_p = 6$. Therefore, the selection of an appropriate kernel scale should be determined by the very specific cases, such as the position of the initial curve C , the noise level and the size of the target.

Figure 5.2 shows the segmentation results of method (b) on the same simulated ultrasound images of Fig. 5.1. In the work of Wang et al., $\sigma_e = \sigma_p = 3$ is applied for testing. However, this setting fails on our data. Clearly, local Gaussian fitting energy with $\sigma_p = \sigma_e$ can not find the correct image boundaries for all initialisations. The first image shows that, the large window size, for instance $\sigma_e = \sigma_p = 5$, leads to serious mis-

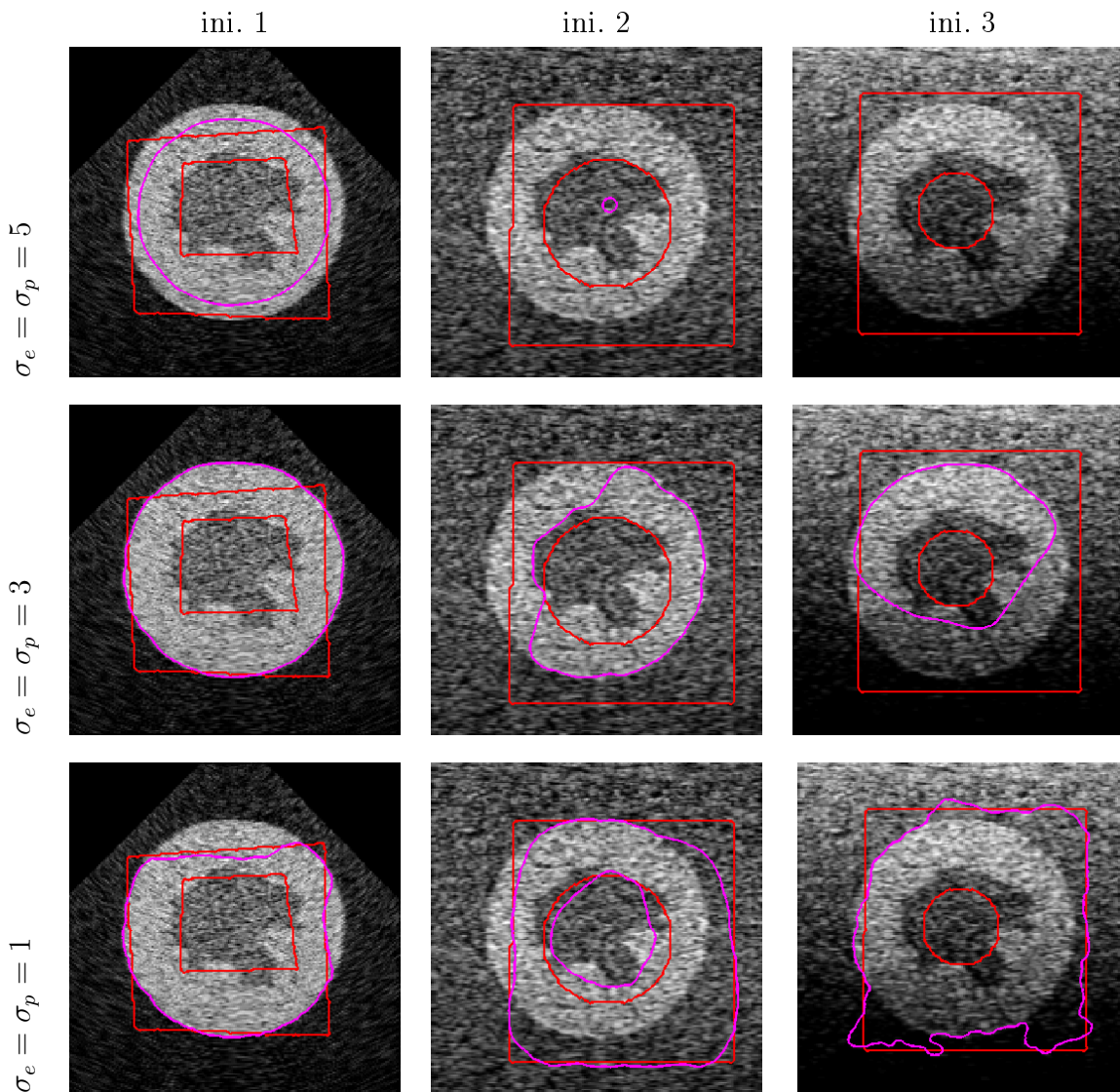


Figure 5.2 – Segmentation results of the local Gaussian fitting model (method (b)). From left to right column : images with 3 different initialisations used in Fig. 5.1. $\nu = 2$.

localisation issues for the outsider contour, and the inside contour disappears totally. On the other hand, the small ones $\sigma_e = \sigma_p \in \{3, 1\}$ perform comparatively better for the outside contours (ini. 1). Still both scales are inappropriate, particularly when the initial curves are far from the true boundaries (ini.2 and 3).

Figure 5.3 shows the segmentation results of method (c). Recall the dilemma of method (b) discussed in § 3.5.2. We suggest to use a very small σ_e and set $\sigma_p \gg \sigma_e$. Therefore, this small σ_e can help to obtain a smoother segmentation with less mis-localisations, and the locality defined by σ_p can better estimate the local region statistics. With $\sigma_e = 1$, all the outcomes of Fig. 5.3 are more appropriate in comparison with these of the method (a) and (b) shown in figures 5.1 and 5.2.

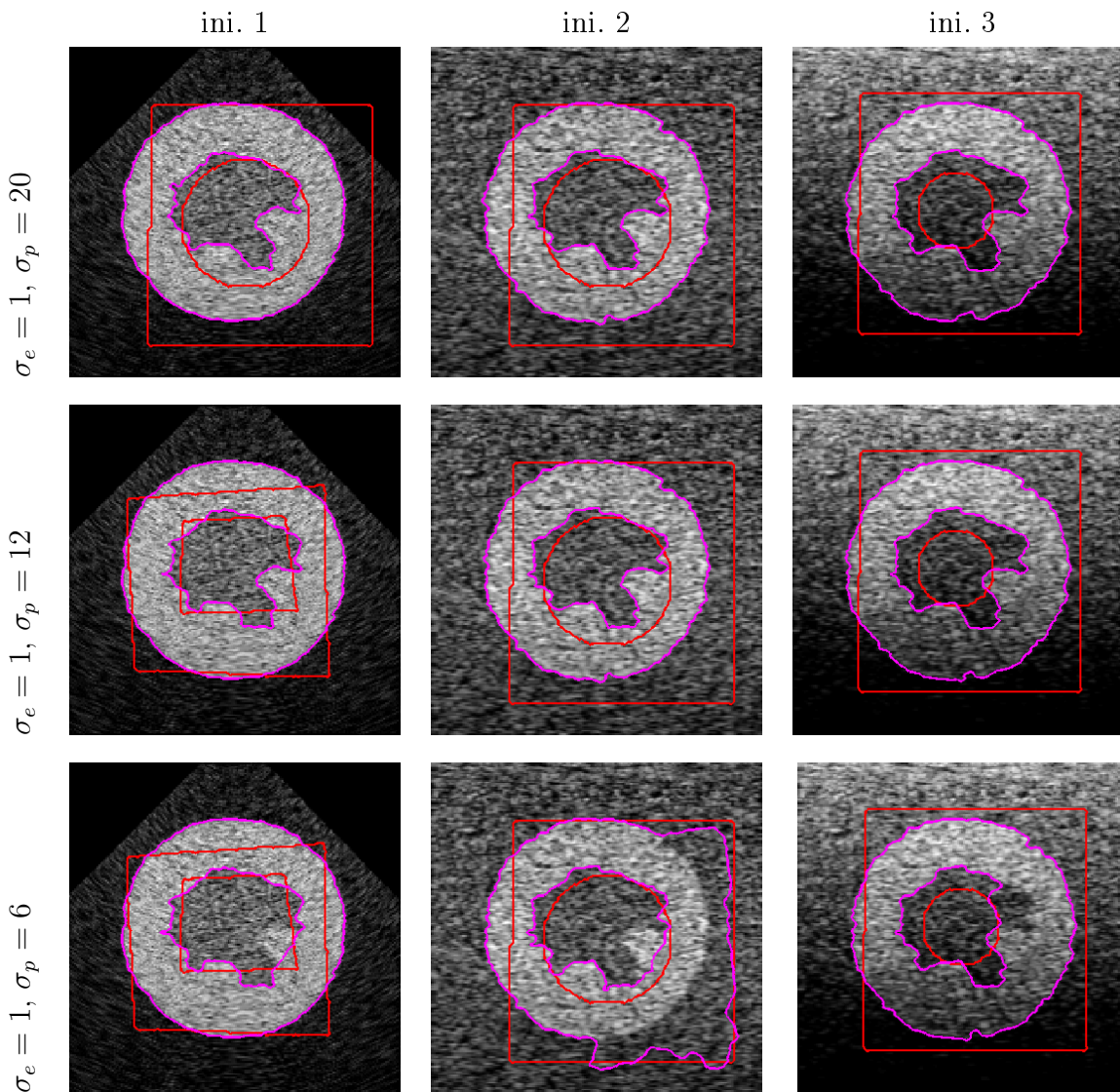


Figure 5.3 – Segmentation results of method (c). From left to right column : images with 3 different initialisations used in Fig. 5.1. $\sigma_e = 1, \nu = 2$.

Finally, we segment these simulated ultrasound images by the local images fitting energy with bias correction (method **(d)**). Notice that, we use an extremely large weight of the internal term, $\nu = 650$. This value depends on the intensity range of the input data (because its external energy function in Eq. (3.15) is not normalised). Method **(d)** also estimates the bias field with the current segmentation. Thus, it should be generally more robust to the attenuation than methods **(a)** to **(c)**. In Fig. 5.4, the image shown in the 3rd column has strong intensity inhomogeneities. For this image, acceptable segmentation results are obtained when using the local scales $\sigma_p = 20, 12$. However, applying $\sigma_p = 6$ shows no improvement than the previously presented methods. To summarise up, the

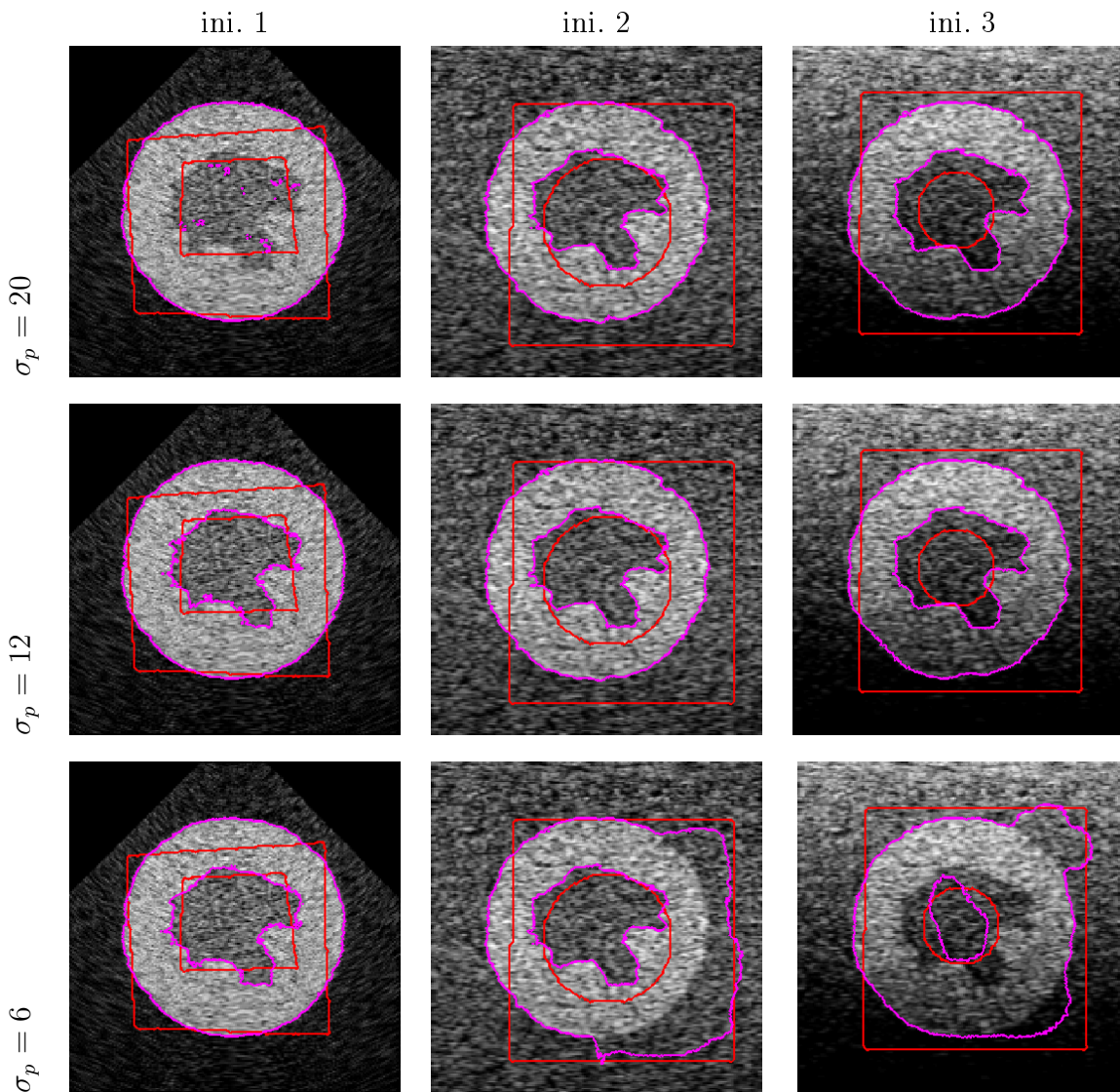


Figure 5.4 – Segmentation results of the local intensity fitting energy with bias correction algorithm (method **(d)**). From left to right column : images with 3 different initialisations used in Fig. 5.1. $\nu = 650$.

performance of method **(d)** also depends highly on the choice of the local scale, which is a typical problem for local region-based algorithms.

ii) Local region-based methods with adaptive scales

Figure 5.5 shows the corresponding results to figures 5.1 to 5.4, when method **(e)** and **(f)** are applied. Both models obtain the appropriate inside and outside boundaries, because they use scale selection procedures to set an optimal scale for each pixel. In order to understand better the behaviour of these two automatic scale selection algorithms, Figure 5.6 shows the contour evolution and the estimated scale maps for the two approaches on the third image of Fig 5.5. As it has been reported recently in [22], the interpretation of the threshold ξ in Piovano and Papadopoulos's method is more difficult than that of α in the ICI algorithm. The proposed approach is based on a compromise between bias and variance for the LPA conditional on the current segmentation.

Figure 5.6 clearly shows that our algorithm uses higher scale values than method **(e)**, when the algorithm converges. For the last few iterations, we no longer apply the max filter, thus the scale maps are reduced in order to increase the accuracy of segmentation.

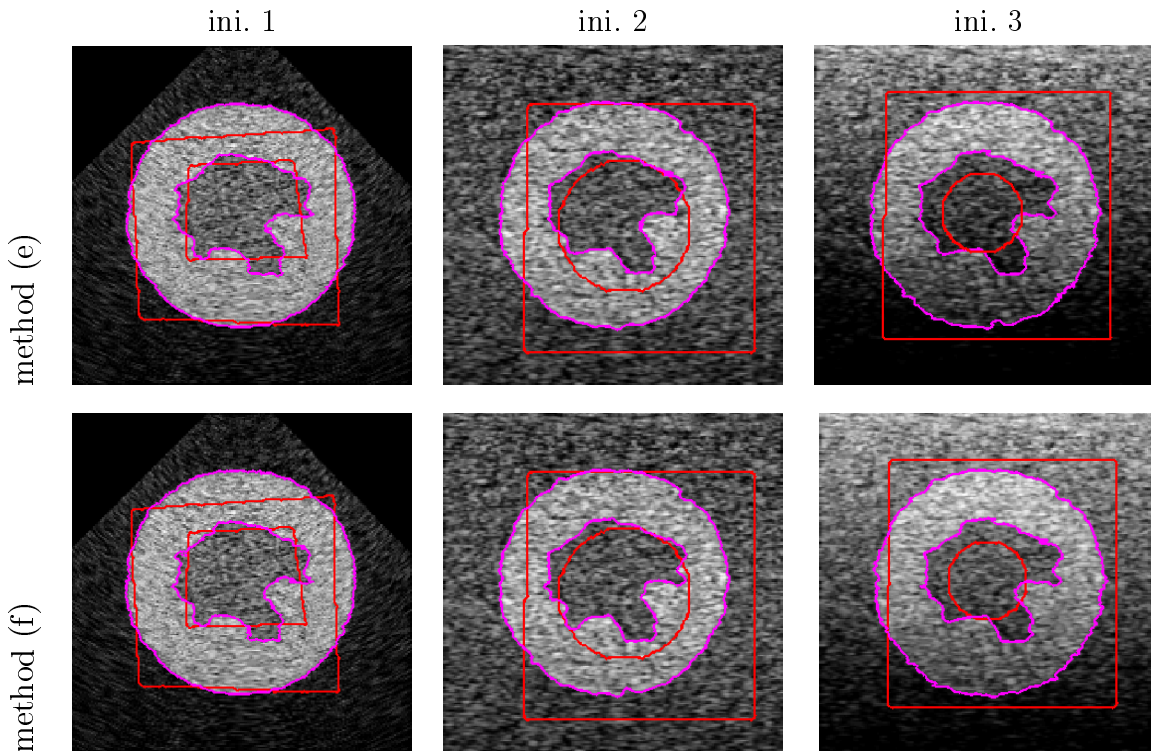


Figure 5.5 – Segmentation results of the local region-based methods with adaptive scales (method **(e)** and **(f)**). From left to right column : images with 3 different initialisations used in Fig. 5.1. Top : Piovano and Papadopoulos's method, $\xi = 1$; bottom : our proposed method, $\Gamma = 2.5$. $\nu = 2$.

For the final scales map, the method (e) uses the minimal value of \mathbf{h} for almost every point, and the proposed one can better reflect the local image information around the segmentation contour.

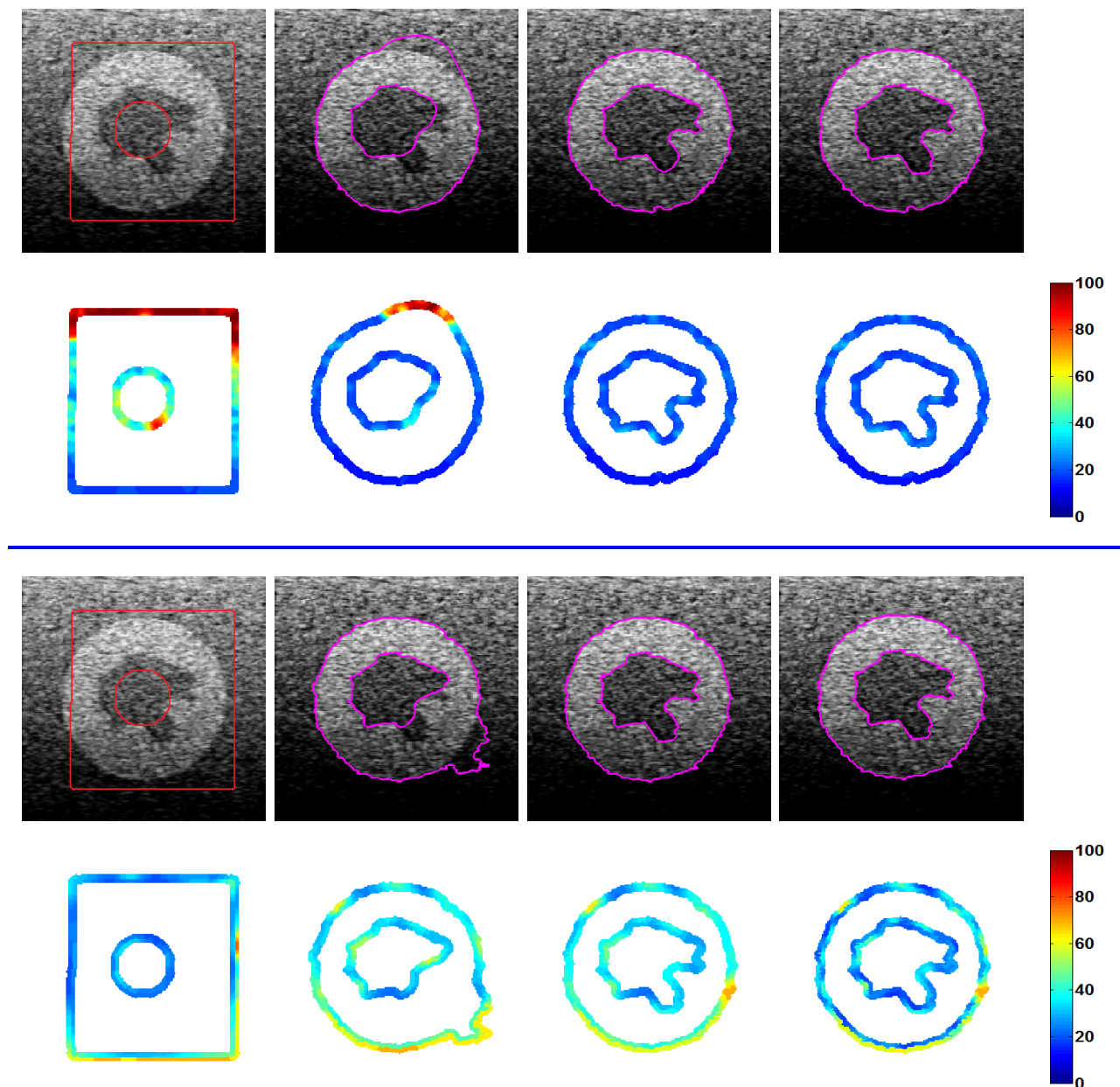


Figure 5.6 – Behaviour of the automatic scale selection algorithms for method (e) and (f). From left to right : the evolution of the segmentation and its corresponding local scales. The top two rows : Piovano and Papadopoulos's method, $\xi = 1$; bottom two rows : our approach, $\Gamma = 2.5$, $\nu = 2$.

iii) Quantitative comparison

We will quantitatively compare our approach with the Piovano and Papadopoulo's scale selection method, as well as the above mentioned algorithms with single local scales. We use 60 simulated ultrasound images with the 3 initialisations shown in previous experiments. The quantitative evaluations are summarized in Table 5.1. It shows statistics of the DCS errors (1-DSC) and the MAD values. Indeed, the table lists the minimum, the three quartiles, the maximum and the interquartile range (IQR) of these two measurements, for five local region-based methods. The closer these statistics to 0, the better is the segmentation. The Q_3 and the maximal values of the DSC error and the MAD indicate the worst cases. Notice that the IQR values is a robust measure of dispersion.¹⁰

| | 100-DSC (%) | | | | | | MAD (in pixels) | | | | | |
|-----------------|-------------|-------------|-------------|-------------|--------------|-------------|-----------------|-------------|-------------|-------------|--------------|-------------|
| | min | Q_1 | Q_2 | Q_3 | max | IQR | min | Q_1 | Q_2 | Q_3 | max | IQR |
| method (a) | | | | | | | | | | | | |
| $\sigma_p = 70$ | 5.26 | 6.68 | 11.55 | 23.52 | 50.16 | 16.84 | 1.46 | 1.78 | 1.96 | 8.83 | 34.86 | 7.05 |
| $\sigma_p = 40$ | 4.53 | 4.89 | 5.29 | 8.57 | 44.82 | 3.68 | 1.39 | 1.52 | 1.62 | 3.54 | 16.82 | 2.02 |
| $\sigma_p = 30$ | 4.35 | 4.58 | 4.88 | 5.36 | 43.24 | 0.78 | 1.38 | 1.46 | 1.55 | 4.07 | 36.90 | 2.61 |
| $\sigma_p = 20$ | 4.14 | 4.37 | 4.59 | 5.27 | 54.24 | 0.90 | 1.35 | 1.42 | 1.48 | 4.51 | 23.55 | 3.09 |
| $\sigma_p = 12$ | 3.99 | 4.26 | 4.56 | 11.29 | 57.85 | 7.03 | 1.25 | 1.44 | 1.52 | 3.35 | 22.40 | 1.91 |
| $\sigma_p = 6$ | 4.07 | 4.44 | 9.88 | 22.90 | 38.22 | 18.47 | 1.34 | 1.51 | 6.84 | 12.63 | 24.23 | 11.12 |
| method (c) | | | | | | | | | | | | |
| $\sigma_p = 40$ | 4.29 | 4.67 | 5.09 | 5.65 | 46.86 | 0.98 | 1.39 | 1.49 | 1.62 | 1.74 | 23.65 | 0.26 |
| $\sigma_p = 30$ | 4.10 | 4.18 | 4.56 | 5.06 | 46.54 | 0.88 | 1.40 | 1.42 | 1.48 | 1.61 | 23.25 | 0.18 |
| $\sigma_p = 20$ | 3.74 | 4.04 | 4.18 | 4.42 | 54.45 | 0.38 | 1.30 | 1.38 | 1.41 | 1.49 | 18.01 | 0.11 |
| $\sigma_p = 12$ | 3.60 | 3.91 | 4.10 | 4.32 | 55.21 | 0.41 | 1.24 | 1.36 | 1.45 | 1.51 | 17.39 | 0.16 |
| $\sigma_p = 6$ | 4.10 | 4.21 | 5.10 | 18.39 | 37.19 | 14.17 | 1.20 | 1.45 | 1.50 | 7.75 | 21.04 | 6.31 |
| method (d) | | | | | | | | | | | | |
| $\sigma_p = 40$ | 4.06 | 5.11 | 5.51 | 7.87 | 32.69 | 2.76 | 1.32 | 1.45 | 1.58 | 1.85 | 14.14 | 0.40 |
| $\sigma_p = 30$ | 4.00 | 4.38 | 5.09 | 5.51 | 32.56 | 1.13 | 1.29 | 1.41 | 1.50 | 1.60 | 10.99 | 0.19 |
| $\sigma_p = 20$ | 3.71 | 4.05 | 4.71 | 5.04 | 32.31 | 0.99 | 1.16 | 1.34 | 1.48 | 1.56 | 14.73 | 0.22 |
| $\sigma_p = 12$ | 3.54 | 4.35 | 4.53 | 5.44 | 28.56 | 1.09 | 1.11 | 1.41 | 1.47 | 1.57 | 17.63 | 0.16 |
| $\sigma_p = 6$ | 3.70 | 4.21 | 6.35 | 19.40 | 30.32 | 15.19 | 1.12 | 1.39 | 1.44 | 4.14 | 20.44 | 2.75 |
| Scale selection | | | | | | | | | | | | |
| method (e) | 3.61 | 4.07 | 4.27 | 4.53 | 35.46 | 0.50 | 1.17 | 1.30 | 1.47 | 1.51 | 21.02 | 0.19 |
| method (f) | 3.53 | 4.06 | 4.21 | 4.56 | 29.44 | 0.47 | 1.15 | 1.27 | 1.42 | 1.51 | 16.59 | 0.24 |

Table 5.1 – Statistics of the DSC errors and the MAD measures obtained on 60 simulated ultrasound images with 3 different initialisations. σ_p is the standard deviation of its spatial kernel. From top to bottom : method (a) $\sigma_e = 0$, method (c) with $\sigma_e = 1$ and $\sigma_p \gg \sigma_e$, method (e) for $\xi = 1$ and method (f) when $\Gamma = 2.5$.

10. A similar comparison was previously used in [22].

Table 5.1 clearly shows that local image statistics should be used for images in the presence of intensity inhomogeneities. Recall that the BC model [32] is equivalent to the local Gaussian fitting model [196] with $\sigma_e = 0$. The largest value of local scale, here $\sigma_p = 70$, for the BC model leads to the worst results. In this case, the local region-based method behaves similarly as the global Gaussian fitting model presented in § 2.5.3.2. With the proposed setting $\sigma_e = 1$, we notice that the segmentation errors of method (c) are smaller than those of the BC model. The maxima of DSC errors and MAD are much smaller for the method (d) in comparison to method (a) and (c), while the rest of the quantitative measures are nearly equivalent. It means that, segmentation results with the help of bias correction algorithm have less outliers in their DSC and MAD. Considering the statistics of all three methods, we can conclude that the decreasing of windows sizes, for example from $\sigma_p = 40$ to 12, could probably improve the performance of segmentation algorithms for these tested images. If the local scale is too small, here $\sigma_p = 6$, the segmentation errors would increase. This reflects exactly the problem of segmentation methods using local image statistics with a single scale.

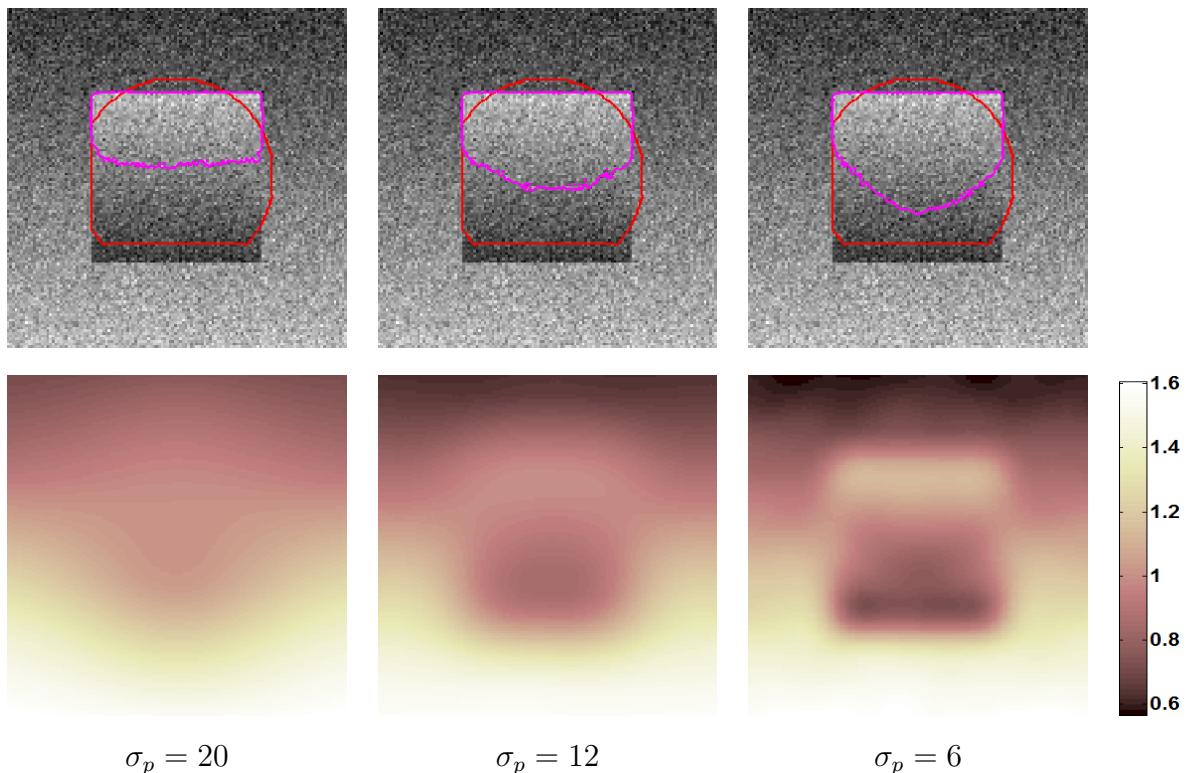


Figure 5.7 – Segmentation of a synthetic image by the intensity fitting model with bias correction (method (d)). The top row : segmentation results using $\sigma_p \in \{20, 12, 6\}$. Bottom row : the estimated bias field corresponding to the above results. Image size 128×128 , $\nu = 650$. See figures 4.4 and 4.12 for the results obtained by method (e) and (f).

The bottom part of table 5.1 shows the statistics of the segmentation results obtained by two scale selection methods : the Piovano and Papadopoulos's algorithm and the proposed one. Notice that both approaches performed pretty well on this dataset. Among all the listed models, our approach generally leads to the smallest minimal and Q_1 to Q_3 values. The interpretation of these measurements indicates a superiority of our algorithm on Piovano and Papadopoulos's.

From Table 5.1, we found out that method **(d)** has quite robust results for the segmentation of ultrasound images. Indeed, its bias correction strategy has the advantage of dealing with the attenuation. In practice, a very large value should be used for its internal term, because its internal energy is not normalised. However, this may ignore small details and decrease the accuracy of the segmentation. Additionally, method **(d)** supposes the bias field is smooth. If the true bias field is piecewise smooth, the corresponding segmentation can not grantee a good result. Figure 5.7 shows an example, where the image foreground and background are degraded separately. The estimated bias field fails to model this piecewise smooth case, thus the segmentation results show no advantage than other local region-based methods with a single local scale.

5.4.2 Echocardiographic images

Ultrasound imaging is the most widely used technique in cardiology, because of its good temporal resolution and relatively low cost. In this part, we will apply local region-based methods for the segmentation of echocardiographic image. Figure 5.8 illustrates several results obtained by the local region-based segmentation methods using a single spatial scale. Form the 1st to 3rd rows, method **(a)** utilises $\sigma_p = 10, 7, 4$; and the bottom two rows illustrate the results obtained by method **(d)** with $\sigma_p = 10, 7$. As expected, an appropriate scale is necessary. The segmentation results are very sensitive to the choice of σ_p , because of the complexity of echocardiographic images. For the examples shown in Fig. 5.8, if the size of the spatial window is large, method **(d)** performs better than **(a)**; if the size of spatial window is smaller, for example $\sigma_p = 7$, the segmentation results of method **(d)** are usually over-smoothed. This is because of the large regularisation term applied for the method with bias correction technique.

Figure 5.9 shows the segmentation results of the same echocardiographic images in Fig. 5.8, as well as three more examples. It verifies that the Piovano and Papadopoulos's and our approaches with scale selection methods can handle this problem. Both methods lead to more acceptable outcomes than the above single scale ones. Therefore, they have the potential to well segment the real ultrasound images. In practice, the prior information

is frequently introduced in segmentation in order to obtain more precise partitions. We believe that the combination of our data-based energy with certain priors can provide more accurate segmentation results.

5.4.3 CT images

In this subsection, we will show segmentation examples of liver in 2D CT scans. The liver segmentation is not an easy task. Indeed, inspecting the lower left part of the first image shown in Fig. 5.10, for instance, the contrast between the liver tissue and its surroundings is very low. Thus, leakage problems often appear. The results of the single scale local method, are shown in the top two rows of Fig. 5.10, for two scales $\sigma_p \in \{10, 5\}$. A local window of scale $\sigma_p = 10$ is already considered as too big when the curve arrived to the most blurred part of the liver, even with strong regularisation. In these cases, method (a) suffers from the same drawback as the global region-based model. If, however, a smaller kernel is used, the method suffers from slow convergence, when the initial curve is too far from the true boundary of the liver tissue. It even moves inwards before its convergence. Ultimately, it does converge after 200 more iterations than using $\sigma_p = 10$ and the other approaches with scale selection strategies.

The Piovano and Papadopoulos's and the proposed segmentation methods outperform the BC model, which uses a single scale. This is expected as they can adaptively choose the local kernel size. Therefore, they generally can well segment the liver after fewer iterations. Notice that, the quality of the CT image is much better than the ultrasound one, thus a smaller Γ is used for our approach.

5.5 Conclusion

In this chapter, we have briefly reviewed the state of the art for the segmentation of ultrasound images, and given some arguments in favour of the proposed local region-based method with the scale selection strategy. Then, we have applied the region-based segmentation methods, presented in previous chapters, on simulated and real echocardiographic images. The qualitative and quantitative comparisons have been done between four single scale methods and two adaptive ones. The experiments show that the methods using scale selection strategies generally obtained the best possible segmentation on ultrasound images with attenuation. Results also show the benefits of the proposed segmentation method than the Piovano-Papadopoulos's one. Additionally, we have applied our model on CT images. These results again suggest that the proposed method has the potential to well

segment images with intensity inhomogeneities. To our knowledge, the other literature, using local region-based segmentation methods, gives a very little attention on choosing appropriate scales for the spatial window.

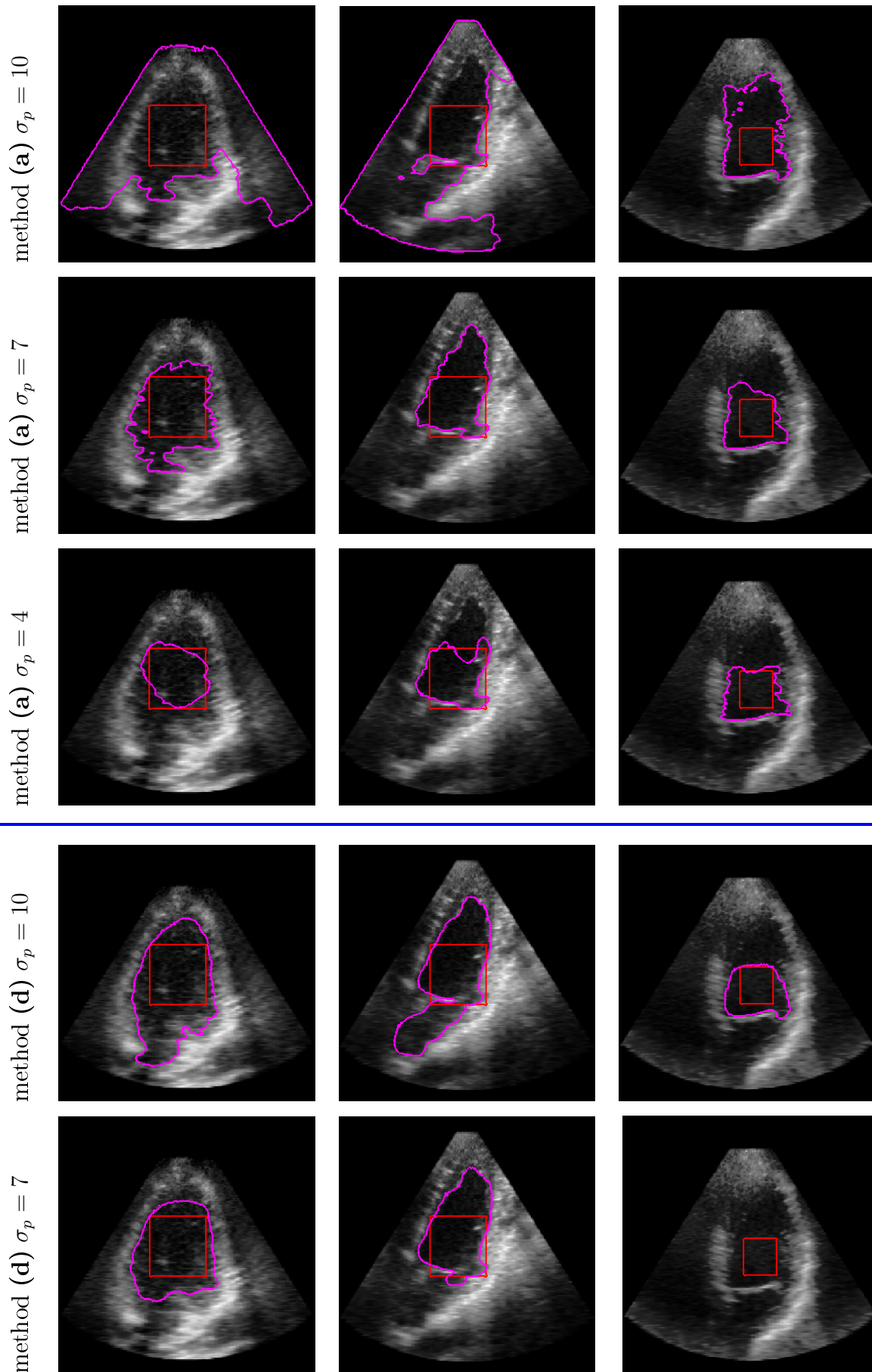


Figure 5.8 – Segmentation of echocardiographic images using local region-based segmentation methods. Top three rows : the BC model, $\nu = 2$. Bottom two rows : the intensity fitting model with bias correction. Image size 208×208 , $\nu = 650$.

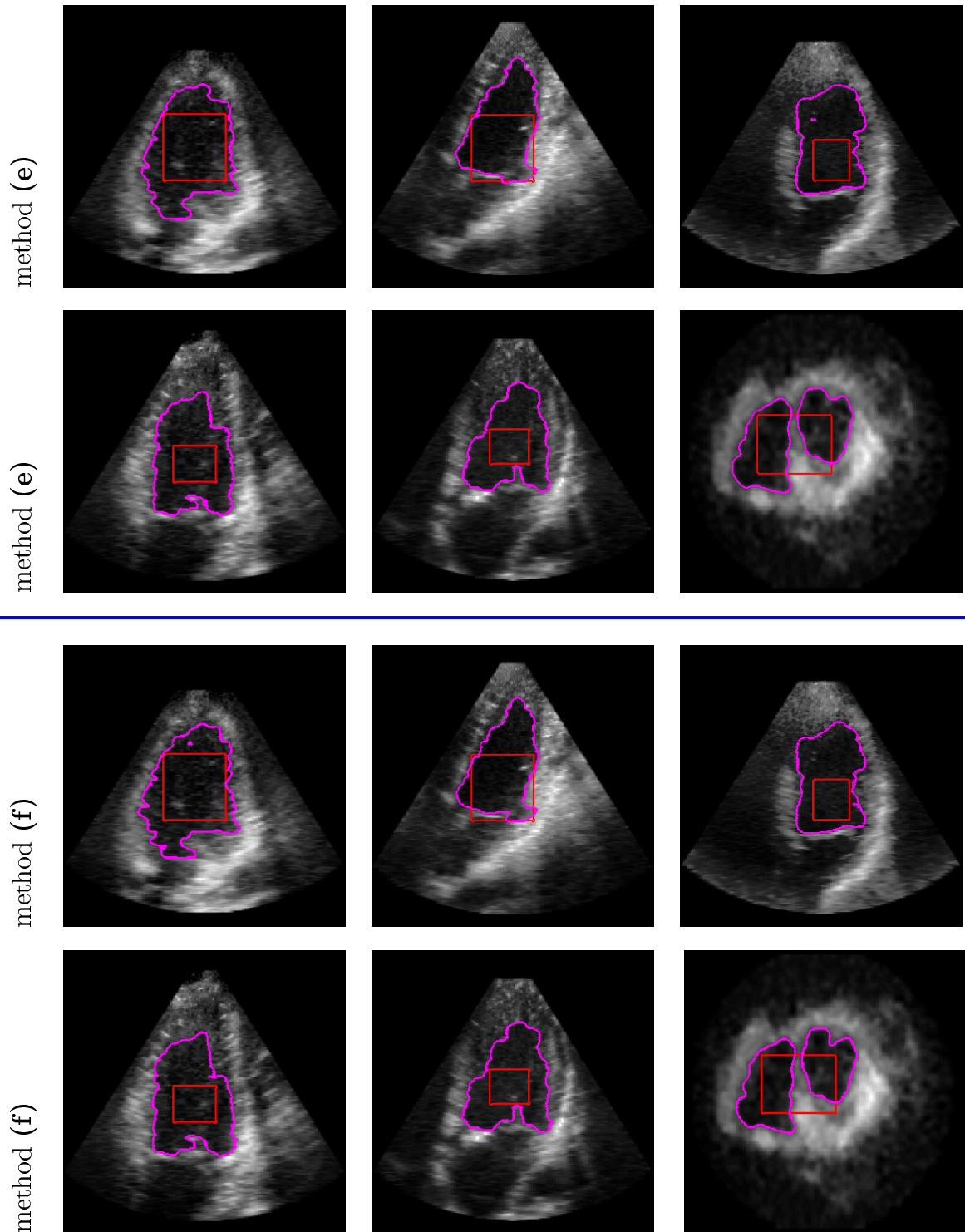


Figure 5.9 – Segmentation of echocardiographic images using local region-based segmentation methods with scale selection strategies. Top : Piovano and Papadopoulo’s model, $\xi = 0.5$; bottom : our approach, $\Gamma = 2.5$.

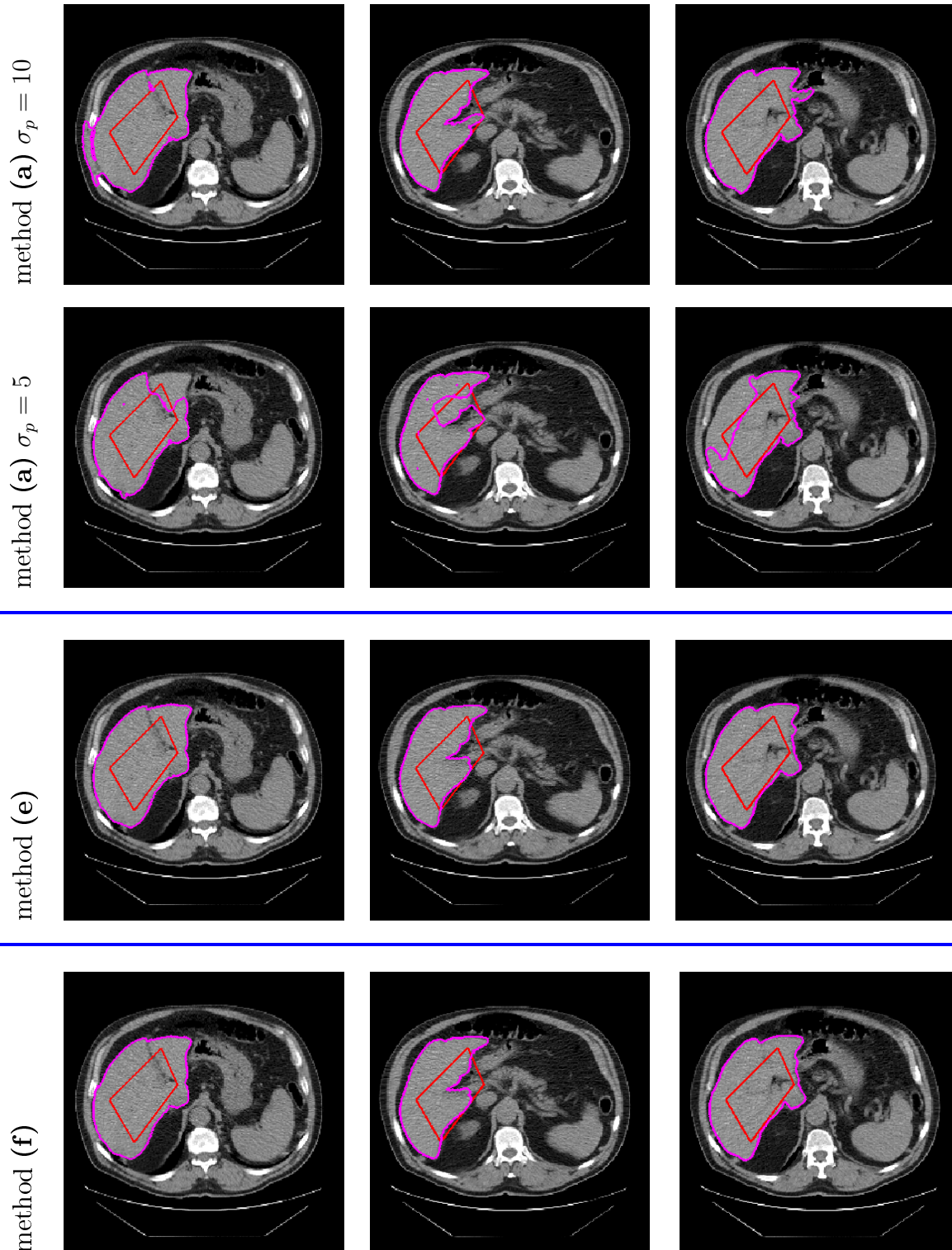


Figure 5.10 – Segmentation examples of liver in 2D scans. The top two rows : the BC model with $\sigma_p = 10$ after 200 iterations and $\sigma_p = 5$ after 400 iterations. The bottom two rows : the Piovano and Papadopoulos’s method ($\xi = 0.5$) and the proposed method ($\Gamma = 1.5$) after 200 iterations. Image size is 256×256 . $\nu = 2$.

Conclusions

6.1 Conclusions

The central objective of this work is to propose effective methods for the segmentation of images with intensity inhomogeneities. To this end, we have studied the recently proposed local region-based segmentation methods. We found out that their performances rely on the choice of the spatial scales, which are used for the estimation of local region statistics. Therefore, we considered this problem when utilising local image information.

Chapter 2 started with an introduction of parametric and geometric active contours. We focused on principles and implementations of the latter and considered methods with an implicit representation of the contours. The segmentation task is achieved via a minimisation of a two terms energy function. We choose to use the conventional length measure as a regularisation term and we limit our analysis to statistical region-based models for the data term. Global segmentation methods are quite robust to initialisations. Also, their external energies can be designed by various statistical models in order to fit the distribution of image intensities. However, they are not valid when the region is statistically inhomogeneous.

In Chapter 3, we investigated the recent developed segmentation algorithms using local image statistics. Through some segmentation examples of simulated images, we have experimentally verified that : 1) local region-based methods outperform global ones in dealing with images with intensity inhomogeneities ; 2) their results are dependent on the choice of the size of the locality. Moreover, we investigated a general functional based on a Bayesian interpretation of the energy function. Originally, it uses the same spatial scale, for the curve evolution (σ_e) and for the estimation of local image statistics (σ_p). We proposed that their sizes should be defined differently. Thus, most existing region-based energies can be incorporated into this model. Additionally, our analysis and test results illustrated that using a very small σ_e with $\sigma_p \gg \sigma_e$ has certain advantages in the segmentation.

In order to improve the robustness of localised segmentation methods, Chapter 4 gave

several possible solutions which can be organized in two categories : 1) combination of global and local image information 2) utilisation of scale selection strategies. We have highlighted that formally these original problems have strong links with image denoising and recent techniques are of interest to our study. Our main contribution was to propose a local region-based segmentation method with adaptive scales. The ICI rule was used to derive a pixel-dependent scale for interior and exterior points along the current segmentation contour. This value is defined in the sense of the MSE minimisation for a LPA of the observed image intensities, inside and outside respectively. The proposed method was successfully applied for the segmentation of some simulated images. We discussed the estimated scales under different SNR levels and probabilities of confidence intervals. These analyses proved that our method outperforms the Piovano and Papadopoulo's scale selection technique.

Finally, Chapter 5 began with a brief review of the state of the art on ultrasound image segmentation. It thereby provides certain foundations of using local region-based segmentation methods. Then, we have evaluated the previously presented segmentation methods using fixed local scales (the BC model [32], the local intensity fitting model of Wang et al.[196] and our modified version with $\sigma_p \gg \sigma_e$, the local fitting model with bias field correction [119]) and methods with adaptive scales selection (Piovano and Papadopoulo's [163] and our LAP-ICI based approach). Experiments on simulated ultrasound images showed that, the local fitting model with bias field correction performs better than other algorithms with a single scale. And as expected, the methods using adaptive scales generally obtained the best possible segmentation. Our approach works quite reliably on images in the presence of intensity inhomogeneities.

6.2 Future works

There are still several issues that need to be further developed in the future.

The quantitative experiments in Chapter 5 have proven that, the local fitting method using the bias correction [119] can handle the attenuation problem in ultrasound images, and may lead to promising segmentation results. Therefore, more discussions and comparisons should be made between this segmentation method and the proposed one with the scale selection strategy. And we may extend our scale selection technique in order to find the optimal local scales for the estimation of local region statistics and bias field compensations.

In Chapter 3, recent local region-based segmentation methods have been introduced.

We noticed that all these algorithms assume a Gaussian distribution in the calculation of local image statistics. In practice, for instance the ultrasound image, the intensity of the observed image does not follow a Gaussian model. For global region-based segmentation methods, a large number of literature has extensively studied the non-Gaussian case. However, their utilisation in local segmentation techniques is quite limited so far [22]. Therefore, there is still a room for further research.

Finally, a very little attention was given to the internal energy. It will be very interesting to combine our data driven energy with an application dependent prior, such as recent non-linear (kernel-based) active shape models, in order to objectively assess the new developments in comparison to the state of the art on ultrasound image segmentation.

6.3 Publications

- Q. Yang and D. Boukerroui, “Ultrasound image segmentation using local statistics with an adaptive scale selection,” *IEEE Int. Symposium on Biomedical Imaging : From Nano to Macro*, Barcelona, Spain, pp. 1096-1099, May, 2012.
- Q. Yang and D. Boukerroui, “Optimal spatial adaptation for local region-based active contours : An intersection of confidence Intervals approach,” *Int. Joint Conference on Computer Vision, Imaging and Computer Graphics Theory and Applications*, Algarve, Portugal, pp. 87–93, March, 2011

Minimisation of local region-based BC energy

A.1 Gâteaux derivative

The Gâteaux derivative [9] is a generalisation of the concept of directional derivative in differential calculus. Suppose X and Y are locally convex topological vector spaces, $U \subset X$, $E : X \rightarrow Y$. The Gâteaux differential of E at $u \in U$ in the direction $\psi \in X$ is defined as :

$$dE(u; \psi) = \lim_{\tau \rightarrow 0} \frac{E(u + \tau\psi) - E(u)}{\tau} = \left. \frac{d}{d\tau} E(u + \tau\psi) \right|_{\tau=0} . \quad (\text{A.1})$$

If the limit exists for all $u \in X$, E is Gâteaux differentiable at u . The Gâteaux derivative can be used in the optimisation of integral function.

Remarks :

1. At each point u , there is a Gâteaux derivative for each direction ψ . In one dimension, there are two Gâteaux differentials for every u , namely forward and backward; in two or more dimensions, there are infinitely many Gâteaux differentials.
2. The Gâteaux derivative is a one-dimensional calculation along a specified direction ψ . Therefore, ordinary one-dimensional calculus and the chain rule work for Gâteaux derivative.

A.2 Gâteaux derivative of the BC model's energy functional

As proposed by Brox and Cremers [32], the data-driven energy of the BC model can be expressed by :

$$E = \sum_r \int_{\Omega} H_r(\phi) \left[\frac{(I(\mathbf{x}) - \mu_r(\mathbf{x}))^2}{2\sigma_r^2(\mathbf{x})} + \frac{1}{2} \log(2\pi\sigma_r^2(\mathbf{x})) \right] d\mathbf{x} . \quad (\text{A.2})$$

For better readability, omit the subindex r , and simply replace μ, σ, H with $\widehat{\mu}_r, \widehat{\sigma}_r, H_r$. Therefore, the external energy of Eq. (A.2) for a single region is written as :

$$E(\phi) = \int_{\Omega} H(\phi(\mathbf{x})) \left[\frac{(I(\mathbf{x}) - \mu(\mathbf{x}))^2}{2\sigma^2(\mathbf{x})} + \frac{1}{2} \log(\sigma^2(\mathbf{x})) \right] d\mathbf{x} , \quad (\text{A.3})$$

where the expressions for $\mu(\mathbf{x})$ and $\sigma^2(\mathbf{x})$ in dependence of ϕ are given by :

$$\begin{aligned} \mu(\mathbf{x}) &= \frac{\int_{\Omega} K(\mathbf{x} - \zeta) H(\phi(\zeta)) I(\zeta) d\zeta}{\int_{\Omega} K(\mathbf{x} - \zeta) H(\phi(\zeta)) d\zeta} , \\ \sigma^2(\mathbf{x}) &= \frac{\int_{\Omega} K(\mathbf{x} - \zeta) H(\phi(\zeta)) I^2(\zeta) d\zeta}{\int_{\Omega} K(\mathbf{x} - \zeta) H(\phi(\zeta)) d\zeta} - \mu^2(\mathbf{x}) , \end{aligned}$$

For computing the minimisation of Eq. (A.3), Brox and Cremers seek its Gâteaux derivative for any direction function $\psi(\mathbf{x})$:

$$\begin{aligned} & \left. \frac{\partial E(\phi(\mathbf{x}) + \tau\psi(\mathbf{x}))}{\partial \tau} \right|_{\tau \rightarrow 0} \\ &= \int_{\Omega} \delta(\phi(\mathbf{x})) \psi(\mathbf{x}) \left[\frac{(I(\mathbf{x}) - \mu(\mathbf{x}))^2}{2\sigma^2(\mathbf{x})} + \log \sigma(\mathbf{x}) \right] d\mathbf{x} \\ & \quad - \frac{1}{2} \int_{\Omega} \frac{H(\phi(\mathbf{x}))}{\sigma^4(\mathbf{x})} \left[2(I(\mathbf{x}) - \mu(\mathbf{x})) \mu_{\phi}(\mathbf{x}) \sigma^2(\mathbf{x}) + (I(\mathbf{x}) - \mu(\mathbf{x}))^2 \sigma_{\phi}^2(\mathbf{x}) \right] d\mathbf{x} \\ & \quad + \int_{\Omega} \frac{H(\phi(\mathbf{x})) \sigma_{\phi}^2(\mathbf{x})}{2 \sigma^2(\mathbf{x})} d\mathbf{x} \\ &= \int_{\Omega} \delta(\phi(\mathbf{x})) \psi(\mathbf{x}) \left[\frac{(I(\mathbf{x}) - \mu(\mathbf{x}))^2}{2\sigma^2(\mathbf{x})} + \log \sigma(\mathbf{x}) \right] d\mathbf{x} \\ & \quad - \frac{1}{2} \int_{\Omega} \frac{H(\phi(\mathbf{x}))}{\sigma^4(\mathbf{x})} \left\{ 2(I(\mathbf{x}) - \mu(\mathbf{x})) \sigma^2(\mathbf{x}) \mu_{\phi}(\mathbf{x}) + \left[(I(\mathbf{x}) - \mu(\mathbf{x}))^2 - \sigma^2(\mathbf{x}) \right] \sigma_{\phi}^2(\mathbf{x}) \right\} d\mathbf{x} , \end{aligned} \quad (\text{A.4})$$

$$\begin{aligned} \text{where } \mu_{\phi}(\mathbf{x}) &= \frac{\int_{\Omega} K(\mathbf{x} - \zeta) \delta(\phi(\zeta)) \psi(\zeta) (I(\zeta) - \mu(\mathbf{x})) d\zeta}{\int_{\Omega} K(\mathbf{x} - \mathbf{z}) H(\phi(\mathbf{z})) d\mathbf{z}} , \\ \sigma_{\phi}^2(\mathbf{x}) &= \frac{\int_{\Omega} K(\mathbf{x} - \zeta) \delta(\phi(\zeta)) \psi(\zeta) (I^2(\zeta) - \sigma^2(\mathbf{x}) - \mu^2(\mathbf{x})) d\zeta}{\int_{\Omega} K(\mathbf{x} - \mathbf{z}) H(\phi(\mathbf{z})) d\mathbf{z}} - 2\mu(\mathbf{x}) \mu_{\phi}(\mathbf{x}) . \end{aligned}$$

Notice that : the first integral in Eq. (A.4) is the usual part considered when applying coordinate descent ; the rest integral takes charge in the changes in the distribution by

varying ϕ . Substitute $\mathbf{x} \rightarrow \mathbf{y}$ and $\zeta \rightarrow \mathbf{x}$ in the second integral of Eq. (A.4) :

$$\begin{aligned}
& \left. \frac{\partial E(\phi(\mathbf{x}) + \tau\psi(\mathbf{x}))}{\partial \tau} \right|_{\tau \rightarrow 0} \\
= & \int_{\Omega} \delta(\phi(\mathbf{x}))\psi(\mathbf{x}) \left[\frac{(I(\mathbf{x}) - \mu(\mathbf{x}))^2}{2\sigma^2(\mathbf{x})} + \log \sigma(\mathbf{x}) \right] d\mathbf{x} \\
& - \frac{1}{2} \int_{\Omega} \frac{H(\phi(\mathbf{y}))}{\sigma^4(\mathbf{y})} 2(I(\mathbf{y}) - \mu(\mathbf{y}))\sigma^2(\mathbf{y}) \frac{\int_{\Omega} K(\mathbf{y} - \mathbf{x})\delta(\phi(\mathbf{x}))\psi(\mathbf{x})(I(\mathbf{x}) - \mu(\mathbf{y}))d\mathbf{x}}{\int_{\Omega} K(\mathbf{x} - \mathbf{z})H(\phi(\mathbf{z}))d\mathbf{z}} d\mathbf{y} \\
& - \frac{1}{2} \int_{\Omega} \frac{H(\phi(\mathbf{y}))}{\sigma^4(\mathbf{y})} \left[(I(\mathbf{y}) - \mu(\mathbf{y}))^2 - \sigma^2(\mathbf{y}) \right] \\
& \frac{\int_{\Omega} K(\mathbf{y} - \mathbf{x})\delta(\phi(\mathbf{x}))\psi(\mathbf{x}) \left[I^2(\mathbf{x}) - \sigma^2(\mathbf{y}) - \mu^2(\mathbf{y}) - 2\mu(\mathbf{y})(I(\mathbf{x}) - \mu(\mathbf{y})) \right] d\mathbf{x}}{\int_{\Omega} K(\mathbf{x} - \mathbf{z})H(\phi(\mathbf{z}))d\mathbf{z}} d\mathbf{y} .
\end{aligned}$$

Then, change the order of integration :

$$\begin{aligned}
& \left. \frac{\partial E(\phi(\mathbf{x}) + \tau\psi(\mathbf{x}))}{\partial \tau} \right|_{\tau \rightarrow 0} \\
= & \int_{\Omega} \delta(\phi(\mathbf{x}))\psi(\mathbf{x}) \left[\frac{(I(\mathbf{x}) - \mu(\mathbf{x}))^2}{2\sigma^2(\mathbf{x})} + \log \sigma(\mathbf{x}) \right] d\mathbf{x} \\
& - \frac{1}{2} \int_{\Omega} \delta(\phi(\mathbf{x}))\psi(\mathbf{x}) \int_{\Omega} \frac{H(\phi(\mathbf{y}))}{\sigma^4(\mathbf{y})} \left[\frac{2(I(\mathbf{y}) - \mu(\mathbf{y}))\sigma^2(\mathbf{y})K(\mathbf{y} - \mathbf{x})(I(\mathbf{x}) - \mu(\mathbf{y}))}{\int_{\Omega} K(\mathbf{x} - \mathbf{z})H(\phi(\mathbf{z}))d\mathbf{z}} \right] d\mathbf{y}d\mathbf{x} \\
& - \frac{1}{2} \int_{\Omega} \delta(\phi(\mathbf{x}))\psi(\mathbf{x}) \int_{\Omega} \frac{H(\phi(\mathbf{y}))}{\sigma^4(\mathbf{y})} \\
& \left\{ \frac{\left[(I(\mathbf{y}) - \mu(\mathbf{y}))^2 - \sigma^2(\mathbf{y}) \right] K(\mathbf{y} - \mathbf{x}) \left[I^2(\mathbf{x}) - \sigma^2(\mathbf{y}) - \mu^2(\mathbf{y}) - 2\mu(\mathbf{y})(I(\mathbf{x}) - \mu(\mathbf{y})) \right]}{\int_{\Omega} K(\mathbf{x} - \mathbf{z})H(\phi(\mathbf{z}))d\mathbf{z}} \right\} d\mathbf{y}d\mathbf{x} .
\end{aligned}$$

Therefore, the shape gradient of the external energy of the BC model can be given by :

$$\begin{aligned}
\frac{\partial E(\phi)}{\partial \phi} = & \delta(\phi(\mathbf{x})) \left[\frac{(I(\mathbf{x}) - \mu(\mathbf{x}))^2}{2\sigma^2(\mathbf{x})} + \log \sigma(\mathbf{x}) \right] \\
& - \frac{1}{2} \delta(\phi(\mathbf{x})) \int_{\Omega} \frac{H(\phi(\mathbf{y}))K(\mathbf{y} - \mathbf{x})}{\sigma^4(\mathbf{y}) \int_{\Omega} K(\mathbf{x} - \mathbf{z})H(\phi(\mathbf{z}))d\mathbf{z}} 2(I(\mathbf{y}) - \mu(\mathbf{y}))\sigma^2(\mathbf{y})(I(\mathbf{x}) - \mu(\mathbf{y}))d\mathbf{y} \\
& - \frac{1}{2} \delta(\phi(\mathbf{x})) \int_{\Omega} \frac{H(\phi(\mathbf{y}))K(\mathbf{y} - \mathbf{x})}{\sigma^4(\mathbf{y}) \int_{\Omega} K(\mathbf{x} - \mathbf{z})H(\phi(\mathbf{z}))d\mathbf{z}} \left\{ \left[(I(\mathbf{y}) - \mu(\mathbf{y}))^2 - \sigma^2(\mathbf{y}) \right] \right. \\
& \left. \left[I^2(\mathbf{x}) - \sigma^2(\mathbf{y}) - \mu^2(\mathbf{y}) - 2\mu(\mathbf{y})(I(\mathbf{x}) - \mu(\mathbf{y})) \right] \right\} d\mathbf{y} .
\end{aligned}$$

The expressions of the second and the third integrals are rather complex. However, one can verify that for a kernel of infinite width these terms can be cancelled. This indicates that the last two terms are only important if the kernel width is very small. In order to

allow for a more efficient implementation, the above function is rearranged and rewritten as [31] :

$$\frac{\partial E(\phi)}{\partial \phi} = \delta(\phi(\mathbf{x})) \left[\frac{(I(\mathbf{x}) - \mu(\mathbf{x}))^2}{2\sigma^2(\mathbf{x})} + \frac{1}{2} \log \sigma^2(\mathbf{x}) - \frac{1}{2} \left(I^2(\mathbf{x})F_4(\mathbf{x}) + I(\mathbf{x})F_5(\mathbf{x}) + F_6(\mathbf{x}) \right) \right] , \quad (\text{A.5})$$

with the following abbreviations :

$$\begin{aligned} F_1(\mathbf{x}) &= \int_{\Omega} K(\mathbf{x} - \mathbf{y})H(\phi(\mathbf{y}))d\mathbf{y} = (K * H(\phi))(\mathbf{x}) , \\ F_2(\mathbf{x}) &= \int_{\Omega} K(\mathbf{x} - \mathbf{y})H(\phi(\mathbf{y}))I(\mathbf{y})d\mathbf{y} = (K * (H(\phi)I))(\mathbf{x}) \quad \rightarrow \quad \mu(\mathbf{x}) = \frac{F_2(\mathbf{x})}{F_1(\mathbf{x})} , \\ F_3(\mathbf{x}) &= \int_{\Omega} K(\mathbf{x} - \mathbf{y})H(\phi(\mathbf{y}))I^2(\mathbf{y})d\mathbf{y} = [K * (H(\phi)I^2)](\mathbf{x}) \quad \rightarrow \quad \sigma^2(\mathbf{x}) = \frac{F_3(\mathbf{x})}{F_1(\mathbf{x})} - \mu^2(\mathbf{x}) , \\ F_4(\mathbf{x}) &= \int_{\Omega} \frac{K(\mathbf{y} - \mathbf{x})H(\phi(\mathbf{y})) \left[(I(\mathbf{y}) - \mu(\mathbf{y}))^2 - \sigma^2(\mathbf{y}) \right]}{\sigma^4(\mathbf{y})F_1(\mathbf{y})} d\mathbf{y} = \left[\bar{K} * \frac{H(\phi)(I - \mu)^2 - \sigma^2}{\sigma^4 F_1} \right](\mathbf{x}) , \\ F_5(\mathbf{x}) &= \int_{\Omega} \frac{K(\mathbf{y} - \mathbf{x})H(\phi(\mathbf{y}))}{\sigma^4(\mathbf{y})F_1(\mathbf{y})} \left\{ 2(I(\mathbf{y}) - \mu(\mathbf{y}))\sigma^2(\mathbf{y}) - 2\mu(\mathbf{y}) \left[(I(\mathbf{y}) - \mu(\mathbf{y}))^2 - \sigma^2(\mathbf{y}) \right] \right\} d\mathbf{y} \\ &= \left\{ \bar{K} * \frac{H(\phi) [2I\sigma^2 - 2\mu(I - \mu)^2]}{\sigma^4 F_1} \right\}(\mathbf{x}) , \\ F_6(\mathbf{x}) &= \int_{\Omega} \frac{K(\mathbf{y} - \mathbf{x})H(\phi(\mathbf{y}))}{\sigma^4(\mathbf{y})F_1(\mathbf{y})} \left\{ 2(I(\mathbf{y}) - \mu(\mathbf{y}))(-\mu(\mathbf{y}))\sigma^2(\mathbf{y}) + \left[(I(\mathbf{y}) - \mu(\mathbf{y}))^2 - \sigma^2(\mathbf{y}) \right] \right. \\ &\quad \left. (-\sigma^2(\mathbf{y}) + \mu^2(\mathbf{y})) \right\} d\mathbf{y} \\ &= \left\{ \bar{K} * \frac{H(\phi) \left[\sigma^2 \left(\frac{F_3}{F_1} - 2I\mu \right) - (I - \mu)^2(\sigma^2 - \mu^2) \right]}{\sigma^4 F_1} \right\}(\mathbf{x}) , \end{aligned}$$

where \bar{K} denotes the mirrored kernel K . Therefore, the Gâteaux derivative of Eq. (A.3) can be implemented efficiently using recursive filters.

Maximum likelihood segmentation with a Rayleigh distribution

Recall the likelihood function with a Rayleigh distribution introduced in § 2.5.3.3 :

$$l = -A_i \log \left(\frac{1}{A_i} \int_{\Omega} I(\mathbf{x})^2 H(\phi) d\mathbf{x} \right) - A_o \log \left(\frac{1}{A_o} \int_{\Omega} I(\mathbf{x})^2 H(-\phi) d\mathbf{x} \right) . \quad (\text{B.1})$$

The maximisation of this likelihood can be expressed using the first variation of the functional with respect to ϕ . Introducing a function ψ of the same type of ϕ , it is necessary to solve the following Gâteaux derivative :

$$\begin{aligned} & \left. \frac{\partial l(\phi + \tau\psi)}{\partial \tau} \right|_{\tau \rightarrow 0} \\ = & - \int_{\Omega} \left. \frac{\partial H(\phi + \tau\psi)}{\partial \tau} \right|_{\tau \rightarrow 0} d\mathbf{x} \left(\log \frac{\int_{\Omega} I^2 H(\phi) d\mathbf{x}}{A_i} \right) - A_i \frac{\tau}{\partial \tau} \log \frac{\int_{\Omega} I^2 H(\phi + \tau\psi) d\mathbf{x}}{\int_{\Omega} H(\phi + \tau\psi) d\mathbf{x}} \Big|_{\tau \rightarrow 0} \\ & - \int_{\Omega} \left. \frac{\partial H(-(\phi + \tau\psi))}{\partial \tau} \right|_{\tau \rightarrow 0} d\mathbf{x} \left(\log \frac{\int_{\Omega} I^2 H(-\phi) d\mathbf{x}}{A_o} \right) - A_o \frac{\partial}{\partial \tau} \log \frac{\int_{\Omega} I^2 H(-(\phi + \tau\psi)) d\mathbf{x}}{\int_{\Omega} H(-(\phi + \tau\psi)) d\mathbf{x}} \Big|_{\tau \rightarrow 0} \\ = & - \int_{\Omega} \delta(\phi) \psi d\mathbf{x} \left(\log \frac{\int_{\Omega} I^2 H(\phi) d\mathbf{x}}{A_i} \right) \\ & - A_i \frac{A_i}{\int_{\Omega} I^2 H(\phi) d\mathbf{x}} \left(\frac{\int_{\Omega} I^2 \delta(\phi) \psi d\mathbf{x}}{A_i} - \frac{\int_{\Omega} I^2 H(\phi) d\mathbf{x} \int_{\Omega} \delta(\phi) \psi d\mathbf{x}}{A_i^2} \right) \\ & + \int_{\Omega} \delta(\phi) \psi d\mathbf{x} \left(\log \frac{\int_{\Omega} I^2 H(-\phi) d\mathbf{x}}{A_o} \right) \\ & - A_o \frac{A_o}{\int_{\Omega} I^2 H(-\phi) d\mathbf{x}} \left(- \frac{\int_{\Omega} I^2 \delta(\phi) \psi d\mathbf{x}}{A_o} + \frac{\int_{\Omega} I^2 H(-\phi) d\mathbf{x} \int_{\Omega} \delta(\phi) \psi d\mathbf{x}}{A_o^2} \right) \\ = & - \int_{\Omega} \delta(\phi) \left(\log \frac{\int_{\Omega} I^2 H(\phi) d\mathbf{x}}{A_i} + \frac{I^2 A_i - \int_{\Omega} I^2 H(\phi) d\mathbf{x}}{\int_{\Omega} I^2 H(\phi) d\mathbf{x}} \right. \\ & \left. - \log \frac{\int_{\Omega} I^2 H(-\phi) d\mathbf{x}}{A_o} - \frac{I^2 A_o - \int_{\Omega} I^2 H(-\phi) d\mathbf{x}}{\int_{\Omega} I^2 H(-\phi) d\mathbf{x}} \right) \psi d\mathbf{x} . \quad (\text{B.2}) \end{aligned}$$

This function can be rewritten as the inner product $\langle \cdot, \psi \rangle$. Therefore, maximisation of the likelihood evolves best following the direction :

$$\begin{aligned} \frac{\partial l(\phi)}{\partial \phi} = & -\delta(\phi) \left[\log \left(\frac{\int_{\Omega} I^2 H(\phi) d\mathbf{x}}{A_i} \right) + \frac{I^2 A_i - \int_{\Omega} I^2 H(\phi) d\mathbf{x}}{\int_{\Omega} I^2 H(\phi) d\mathbf{x}} \right. \\ & \left. - \log \left(\frac{\int_{\Omega} I^2 H(-\phi) d\mathbf{x}}{A_o} \right) - \frac{I^2 A_o - \int_{\Omega} I^2 H(-\phi) d\mathbf{x}}{\int_{\Omega} I^2 H(-\phi) d\mathbf{x}} \right]. \end{aligned} \quad (\text{B.3})$$

Noise estimation methods

Noise estimation methods have been proposed in many studies. A recent review [110] has classified them as Block [130], Average or Median [148], Pyramid [132] based methods and so on. The commonly used observation model supposes a piecewise constant image with additive white noise $I(\mathbf{x})$. Thereby, it is possible to estimate the statistics of the noise, for example by the following difference function :

$$d(i, j) = 2I(\mathbf{x}_{i,j}) - I(\mathbf{x}_{i-1,j}) - I(\mathbf{x}_{i,j-1}) ,$$

where $i = 1, 2, \dots, n$, $j = 1, 2, \dots, m$, $\mathbf{x}_{i,j} \in \Omega \subset \mathbb{R}^2$. Thus, d mainly contains information about the noise as well as image discontinuities. The mathematical expectation and the variance of d can be estimated as :

$$\begin{aligned} \mathbb{E}[d(i, j)] &= 2\mathbb{E}[I(\mathbf{x}_{i,j})] - \mathbb{E}[I(\mathbf{x}_{i-1,j})] - \mathbb{E}[I(\mathbf{x}_{i,j-1})] \\ &\simeq 2\mathbb{E}[I(\mathbf{x}_{i,j})] - \mathbb{E}[I(\mathbf{x}_{i,j})] - \mathbb{E}[I(\mathbf{x}_{i,j})] \simeq 0 . \end{aligned}$$

$$\begin{aligned} \mathbf{Var}(d(i, j)) &= 4\mathbf{Var}(I(\mathbf{x}_{i,j})) + \mathbf{Var}(I(\mathbf{x}_{i-1,j})) + \mathbf{Var}(I(\mathbf{x}_{i,j-1})) \\ &\simeq 6\mathbf{Var}(I(\mathbf{x}_{i,j})) = 6\sigma^2 . \end{aligned} \tag{C.1}$$

Meanwhile, the variance of d can be empirically obtained by :

$$\hat{\sigma}_d^2 = \frac{1}{nm-1} \sum_{i,j} (d(i, j) - \bar{d})^2 . \tag{C.2}$$

Combining the above two results, σ can be estimated by :

$$\hat{\sigma} = \frac{\hat{\sigma}_d}{\sqrt{6}} . \tag{C.3}$$

Suppose the additive noise is Gaussian, the median of the absolute deviation [81] can be simply calculated as :

$$\hat{\sigma}_M = \frac{\text{median}(|\mathbf{d} - \text{median}(\mathbf{d})|)}{0.6745} , \tag{C.4}$$

where $\mathbf{d} = (d(i, j))$ is a vector formed by the differences between adjacent samples of the noisy observations. The constant 0.6745 is the approximation of $\Phi^{-1}(3/4)$, where Φ^{-1} is the inverse of the cumulative distribution function for the standard normal distribution. In other words, for a symmetric distribution with zero mean, the population median absolute deviation is the 75th percentile of the distribution.

Figure C.1 shows images degraded by an additive Gaussian noise (the top two rows) and by a Rayleigh noise (the bottom two rows). From left to right, this figure presents the noisy observations at four different noise levels. Using Eq. (C.3) and Eq. (C.4) respectively for these images, we achieve the estimated image noise variances listed in Table C.1. For the images with high SNR, both $\hat{\sigma}$ and $\hat{\sigma}_M$ over estimate the true noise variance ; and for the severely degraded images, the estimations are quite accurate. Also, we notice that $\hat{\sigma}$ is comparatively better than $\hat{\sigma}_M$. This is because of the accuracy of the median absolute deviation method depends highly on the noise model, although the median has been proven to be robust with respect to outliers.

| Noise | House | | | | Lena | | | |
|------------------|-------|-------|-------|-------|-------|-------|-------|-------|
| Gaussian | | | | | | | | |
| σ | 5.00 | 15.00 | 25.00 | 35.00 | 5.00 | 15.00 | 25.00 | 35.00 |
| $\hat{\sigma}$ | 6.46 | 15.95 | 25.64 | 35.47 | 7.44 | 16.87 | 26.37 | 36.17 |
| $\hat{\sigma}_M$ | 8.22 | 16.37 | 25.83 | 35.70 | 11.49 | 18.21 | 27.06 | 36.58 |
| Rayleigh | | | | | | | | |
| σ | 4.60 | 13.84 | 22.81 | 32.03 | 4.63 | 13.86 | 23.03 | 32.74 |
| $\hat{\sigma}$ | 6.16 | 14.86 | 23.82 | 33.21 | 7.13 | 15.90 | 24.74 | 33.80 |
| $\hat{\sigma}_M$ | 8.04 | 15.38 | 24.07 | 33.42 | 11.37 | 17.37 | 25.37 | 34.41 |

Table C.1 – The values of real standard deviations and the estimated ones for the noisy images shown in Fig. C.1.

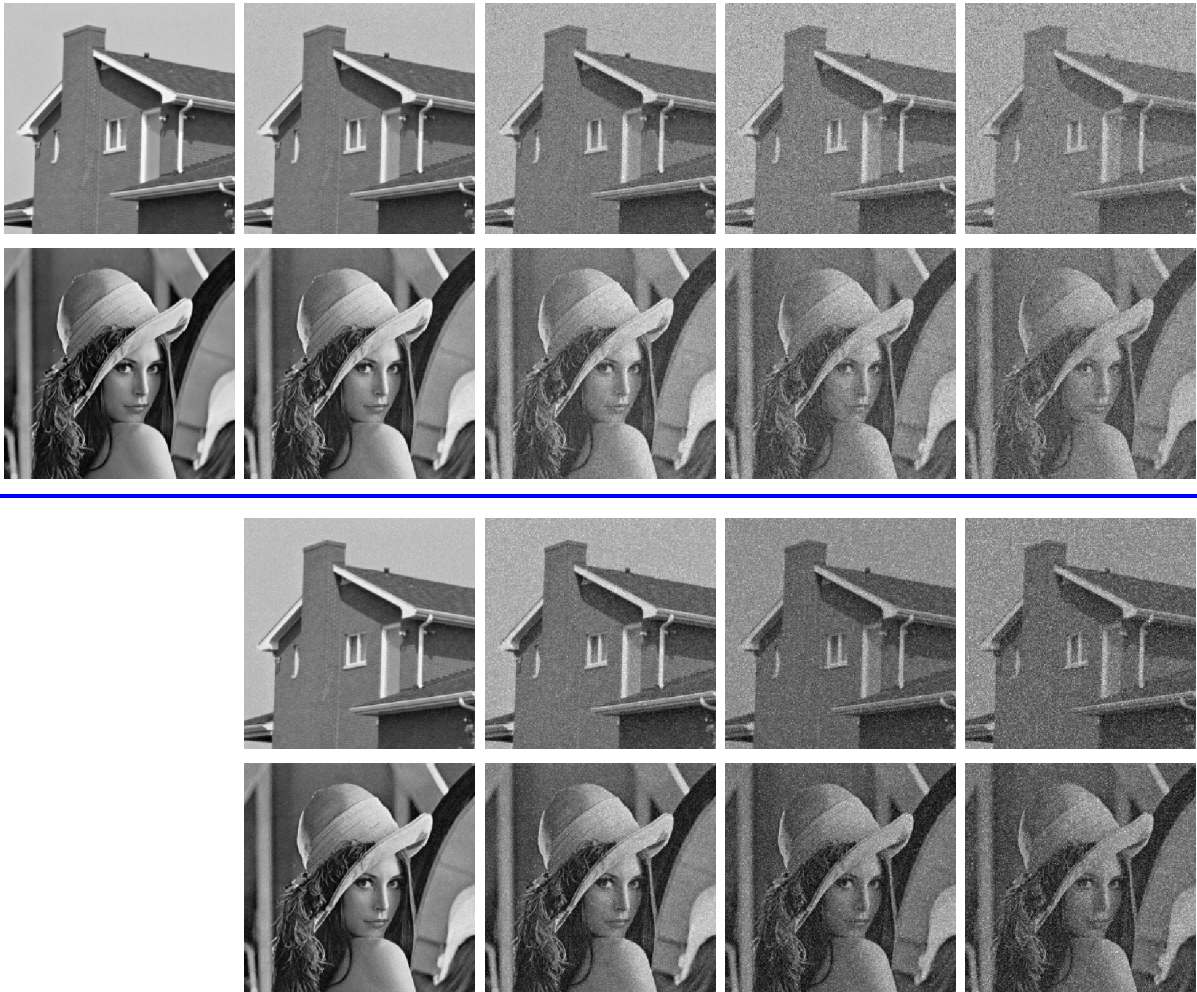


Figure C.1 – Original images and their noisy observations. Top two rows : noise free images and observations at four levels of an additive Gaussian noise with standard derivations $\sigma = \{2, 15, 25, 35\}$; bottom two rows : Rayleigh noise with $\sigma = \{4.63, 13.86, 23.03, 32.74\}$.

Bibliographie

- [1] K. Z. Abd-Elmoniem, A.-B. M. Yousef, and Y. M. Kadah, "Real-time speckle reduction and coherence enhancement in ultrasound imaging via nonlinear anisotropic diffusion," *IEEE Trans. Biomed. Eng.*, vol. 49, no. 9, pp. 997–1014, 2002.
- [2] D. Adalsteinsson and J. Sethian, "A fast level set method for propagating interfaces," *J. Comput. Phys.*, vol. 118, no. 2, pp. 269–277, 1995.
- [3] R. Adams and L. Bischof, "Seeded region growing," *IEEE Trans. Pattern Anal. Mach. Intell.*, vol. 16, no. 6, pp. 641–647, 1994.
- [4] L. Alvarez, F. Guichard, P. Lions, and J. Morel, "Axioms and fundamental equations of image processing," *Arch. for Rational Mechanics*, vol. 123, no. 3, pp. 199–257, 1993.
- [5] L. Ambrosio and V. Tortorelli, "Approximation of functional depending on jumps by elliptic functional via Γ -convergence," *Comm. Pure Appl. Math.*, vol. 43, pp. 999–1036, 1990.
- [6] A. Amini, T. Weymouth, and R. Jain, "Using dynamic programming for solving variational problems in vision," *IEEE Trans. Pattern Anal. Mach. Intell.*, vol. 12, no. 9, pp. 855–867, 1990.
- [7] P. Arbelaez, M. Maire, C. Fowlkes, and J. Malik, "Contour detection and hierarchical image segmentation," *IEEE Trans. Pattern Anal. Mach. Intell.*, vol. 33, no. 5, pp. 898–916, may 2011.
- [8] E. Ashton and K. Parker, "Multiple resolution Bayesian segmentation of ultrasound images," *Ultrasonic Imag.*, vol. 17, no. 2, pp. 291–304, 1995.
- [9] G. Aubert and P. Kornprobst, *Mathematical problems in image processing : partial differential equation and the calculus of variations*. New York : Springer-Verlag, 2002.

- [10] G. Aubert, M. Barlaud, O. D. Faugeras, and S. Jehan-Besson, “Image segmentation using active contours : Calculus of variations or shape gradients ?” *SIAM J. Applied Mathematics*, vol. 63, no. 6, pp. 2128–2154, 2003.
- [11] I. Ayed, S. Li, and I. Ross, “Level set image segmentation with a statistical overlap constraint,” in *Info. Proc. Med. Imag.*, vol. 5636, 2009, pp. 439–455.
- [12] I. B. Ayed, A. Mitiche, and Z. Belhadj, “Multiregion level-set partitioning of synthetic aperture radar images,” *IEEE Trans. Pattern Anal. Mach. Intell.*, vol. 27, no. 5, pp. 793–800, 2005.
- [13] D. C. Barbosa, T. Dietenbeck, J. Schaerer, J. D’hooge, D. Friboulet, and O. Bernard, “B-spline explicit active surfaces : An efficient framework for real-time 3D region-based segmentation,” *IEEE Trans. Image Process.*, vol. 21, no. 1, pp. 241–251, 2012.
- [14] A. Belaid, D. Boukerroui, Y. Maingourd, and J.-F. Lerallut, “Implicit active contours for ultrasound images segmentation driven by phase information and local maximum likelihood,” in *IEEE Int. Symp. Biomed. Imag.*, Chicago, Illinois, Apr. 2011, pp. 630–635.
- [15] ———, “Phase-based level set segmentation of ultrasound images,” *IEEE Trans. Information Tech. Biomed.*, vol. 15, no. 1, pp. 138–147, 2011.
- [16] U. Benz, P. Hofmann, G. Willhauck, I. Lingenfelder, and M. Heynen, “Multi-resolution, object-oriented fuzzy analysis of remote sensing data for GIS-ready information,” *ISPRS J. Photogrammetry and Remote Sensing*, pp. 239–258, 2004.
- [17] C. M. Bishop, *Pattern Recognition and Machine Learning (Information Science and Statistics)*. New York : Springer-Verlag, 2006.
- [18] A. Blake and M. Isard, *Active Contours*. New York : Springer-Verlag, 1998.
- [19] A. Blake and A. Zisserman, *Visual Reconstruction*. Cambridge, MA, USA : MIT Press, 1987.
- [20] J. Bosch, S. Mitchell, B. P. Lelieveldt, F. Nijland, O. Kamp, M. Sonka, and J. H. Reiber, “Automatic segmentation of echocardiographic sequences by active appearance motion models,” *IEEE Trans. Med. Imag.*, vol. 21, no. 11, pp. 1373–1383, 2002.

- [21] D. Boukerroui, J. A. Noble, and M. Brady, "On the choice of band-pass quadrature filters," *J. Math. Imag. Vis.*, vol. 21, no. 1, pp. 53–80, 2004.
- [22] D. Boukerroui, "A local rayleigh model with spatial scale selection for ultrasound image segmentation," in *British Mach. Vis. Conf.*, R. Bowden, J. Collomosse, and K. Mikolajczyk, Eds., Surrey, UK, Sep 2012, pp. 84–84.
- [23] D. Boukerroui, A. Baskurt, A. Noble, and O. Basset, "Segmentation of ultrasound images—multiresolution 2D and 3D algorithm based on global and local statistics," *Pattern Recognit. Lett.*, vol. 24, pp. 779–790, 2003.
- [24] D. Boukerroui, O. Basset, A. Baskurt, and A. Noble, "Segmentation of echocardiographic data. multiresolution 2D and 3D algorithm based on gray level statistics," in *MICCAI*. Cambridge, UK : Springer-Verlag, 1999, pp. 516–524.
- [25] D. Boukerroui, J. A. Noble, and M. Brady, "Velocity estimation in ultrasound images : A block matching approach." in *Info. Proc. Med. Imag.*, ser. Lecture Notes in Computer Science, C. J. Taylor and J. A. Noble, Eds., vol. 2732. Springer, 2003, pp. 586–598.
- [26] X. Bresson, S. Esedoglu, P. Vandergheynst, J. Thiran, and S. Osher, "Fast global minimization of the active contour/Snake model," *J. Math. Imag. Vis.*, vol. 28, no. 2, pp. 151–167, 2007.
- [27] X. Bresson and T. F. Chan, "Non-local unsupervised variational image segmentation models," UCLA C.A.M. Report, Tech. Rep. 08-67, 2008.
- [28] X. Bresson, P. Vandergheynst, and J.-P. Thiran, "A variational model for object segmentation using boundary information and statistical shape prior driver by the Mumford-Shah functional," *Int. J. Comput. Vis.*, vol. 28, no. 2, pp. 145–162, 2006.
- [29] C. R. Brice and C. L. Fennema, "Scene analysis using regions," *Artificial Intelligence*, vol. 1, no. 3-4, pp. 205–226, 1970.
- [30] S. Bridal, J. Correas, A. Saied, and P. Laugier, "Milestones on the road to higher resolution, quantitative, and functional ultrasonic imaging," *Proceedings of the IEEE*, vol. 91, no. 10, pp. 1543–1561, 2003.

- [31] T. Brox and D. Cremers, “On the statistical interpretation of the piecewise smooth Mumford-Shah functional,” in *Int. Conf. on Scale Space and Variational Methods in Comput. Vis. (SSVM)*, ser. Lect. Note Comput. Sci, vol. 4485. Springer, May 2007, pp. 203–213.
- [32] ———, “On local region models and a statistical interpretation of the piecewise smooth Mumford-Shah functional,” *Int. J. Comput. Vis.*, vol. 84, no. 2, pp. 184–193, 2009.
- [33] E. Brusseau, C. L. de Korte, F. Mastik, J. Schaar, and A. F. W. van der Steen, “Fully automatic luminal contour segmentation in intracoronary ultrasound imaging—a statistical approach,” *IEEE Trans. Med. Imag.*, vol. 23, no. 5, pp. 554–566, 2004.
- [34] A. Buades and B. Coll, “A non-local algorithm for image denoising,” in *IEEE Int. Conf. Comput. Vis. Pattern Recognit.*, vol. 2, 2005, pp. 60–65.
- [35] C. B. Burckhardt, “Speckle in ultrasound B-mode scans,” *IEEE Trans. Sonics and Ultra.*, vol. 25, no. 1, Jan. 1978.
- [36] J. Canny, “A computational approach to edge detection,” *IEEE Trans. Pattern Anal. Mach. Intell.*, vol. 8, no. 6, pp. 679–698, 1986.
- [37] V. Caselles, F. Catté, T. Coll, and F. Dibos, “A geometric model for active contours in image processing,” *Numerische Mathematik*, vol. 66, no. 1, pp. 1–31, 1993.
- [38] V. Caselles, R. Kimmel, and G. Sapiro, “Geodesic active contours,” *Int. J. Comput. Vis.*, vol. 22, no. 1, pp. 61–79, 1997.
- [39] V. Chalana, D. Linker, D. Haynor, and Y. Kim, “A multiple active contour model for cardiac boundary detection on echocardiographic sequences,” *IEEE Trans. Med. Imag.*, vol. 15, no. 3, pp. 290–298, 1996.
- [40] T. Chan and L. Vese, “Active contours without edges,” *IEEE Trans. Image Process.*, vol. 10, no. 2, pp. 266–277, 2001.
- [41] Y. L. Chang and X. Li, “Adaptive image region-growing,” *IEEE Trans. Image Process.*, vol. 3, no. 6, pp. 868–872, 1994.
- [42] Y. Chen, S. Thiruvenkadam, F. Huang, D. Wilson, E. Geiser, and H. Tagare, “On the incorporation of shape priors into geometric active contours,” in *IEEE Workshop*

- on *Variational and Level Set Methods (VLSM'01)*, Washington, USA, 2001, pp. 145–152.
- [43] Y. Cheng, “Mean shift, mode seeking, and clustering,” *IEEE Trans. Pattern Anal. Mach. Intell.*, vol. 17, no. 8, pp. 790–799, 1995.
- [44] C. C. Chu and J. K. Aggarwal, “The integration of image segmentation maps using region and edge information,” *IEEE Trans. Pattern Anal. Mach. Intell.*, vol. 15, no. 12, pp. 1241–1252, Dec. 1993.
- [45] L. Cohen and R. Kimmel, “Global minimum for active contour models : A minimal path approach,” *Int. J. Comput. Vis.*, vol. 24, no. 1, pp. 57–78, 1997.
- [46] L. Cohen, “On active contour models and balloons,” in *CVGIP Image Understanding*, vol. 53, no. 2, 1991, pp. 211–218.
- [47] L. Cohen and I. Cohen, “Finite-element methods for active contour models and balloons for 2D and 3D images,” *IEEE Trans. Pattern Anal. Mach. Intell.*, vol. 15, no. 11, pp. 1131–1147, 1993.
- [48] D. Comaniciu, X. Zhou, and S. Krishnan, “Robust real-time myocardial border tracking for echocardiography : An information fusion approach,” *IEEE Trans. Med. Imag.*, vol. 23, no. 7, pp. 849–860, 2004.
- [49] T. Cootes, C. J. Taylor, D. H. Cooper, and J. Graham, “Active shape models and their training and application,” *Comput. Vis. and Image Understanding*, vol. 61, no. 1, pp. 38–59, 1995.
- [50] T. M. Cover and J. A. Thomas, *Elements of information theory*. New York : John Wiley & Sons Inc., 1991.
- [51] D. Cremers, “Statistical shape knowledge in variational image segmentation,” Ph.D. dissertation, University of Mannheim, Germany, 2002.
- [52] D. Cremers, M. Rousson, and R. Deriche, “Review of statistical approaches to level set segmentation : Integrating color, texture, motion and shape,” *Int. J. Comput. Vis.*, vol. 72, no. 2, pp. 195–215, 2007.

- [53] G. Demarcq, L. Mascarilla, M. Berthier, and P. Courtellemont, "The color monogenic signal : Application to color edge detection and color optical flow," *J. Math. Imag. Vis.*, vol. 40, no. 3, pp. 269–284, Jul. 2011.
- [54] R. Deriche, "Using Canny's criteria to derive a recursively implemented optimal edge detector," *Int. J. Comput. Vis.*, vol. 1, no. 2, pp. 167–187, 1987.
- [55] F. Destrempes and G. Cloutier, "A critical review and uniformized representation of statistical distributions modeling the ultrasound echo envelope," *Ultrasound Med. Biol.*, vol. 36, no. 7, pp. 1037 – 1051, 2010.
- [56] V. Dutt and J. Greenleaf, "Ultrasound echo envelope analysis using a homodyned K -distribution signal model," *Ultrasonic Imag.*, vol. 16, pp. 265–287, 1994.
- [57] ———, "Adaptive speckle reduction filter for log-compressed B-scan images," *IEEE Trans. Med. Imag.*, vol. 16, no. 6, pp. 802–813, 1996.
- [58] V. Dutt, "Statistical analysis of ultrasound echo envelope," Ph.D. dissertation, The Mayo Graduate School, Aug. 1995.
- [59] V. Duval, J.-F. Aujol, and Y. Gousseau, "A bias-variance approach for the nonlocal means," *SIAM J. Imag. Sciences*, vol. 4, no. 2, pp. 760–788, 2011.
- [60] J. H. Elder and S. W. Zucker, "Local scale control for edge detection and blur estimation," *IEEE Trans. Pattern Anal. Mach. Intell.*, vol. 20, no. 7, pp. 699–716, 1998.
- [61] A. Elmoataz, O. Lezoray, and S. Boughleux, "Nonlocal discrete regularization on weighted graphs : A framework for image and manifold processing, preprint," *IEEE Trans. Image Process.*, vol. 17, pp. 1047–1060, 2008.
- [62] T. Eltoft, "Modeling the amplitude statistics of ultrasonic images," *IEEE Trans. Med. Imag.*, vol. 25, no. 2, pp. 229–240, 2008.
- [63] J. Fan and I. Gijbels, *Local Polynomial Modelling and Its Applications*. London : Chapman & Hall, 1996.
- [64] M. Felsberg and G. Sommer, "The monogenic signal," *IEEE Trans. Signal Process.*, vol. 49, no. 12, pp. 3136–3144, Dec. 2001.

- [65] ———, “The monogenic scale-space : A unifying approach to phase-based image processing in scale-space,” *J. Math. Imag. Vis.*, vol. 21, no. 1, pp. 5–26, 2004.
- [66] A. Foi, V. Katkovnik, K. Egiazarian, and J. Astola, “A novel anisotropic local polynomial estimator based on directional multiscale optimizations,” in *Proc. of the 6th IMA Int. Conf. Math. in Signal Process.*, Cirencester, UK, 2004, pp. 79–82.
- [67] D. Freeman and T. Zhang, “Active contours for tracking distributions,” *IEEE Trans. Image Process.*, vol. 10, no. 2, pp. 266–277, 2004.
- [68] W. T. Freeman and E. H. Adelson, “The design and use of steerable filters,” *IEEE Trans. Pattern Anal. Mach. Intell.*, vol. 13, no. 9, pp. 891–906, 1991.
- [69] K. Fu and J. Mui, “A survey on image segmentation,” *Pattern Recognit.*, vol. 13, no. 1, pp. 3–16, 1981.
- [70] K. Fukunaga and L. D. Hostetler, “The estimation of the gradient of a density function, with applications in pattern recognition,” *IEEE Trans. Information Theory*, vol. 21, pp. 32–40, 1975.
- [71] C. D. Garson, B. Li, S. T. Acton, and J. A. Hossack, “Guiding automated left ventricular chamber segmentation in cardiac imaging using the concept of conserved myocardial volume.” *Comput. Med. Imag. Graph.*, vol. 32, no. 4, pp. 321–30, 2008.
- [72] A. Gelas, O. Bernard, D. Friboulet, and R. Prost, “Compactly supported radial basis functions based collocation method for level-set evolution in image segmentation,” *IEEE Trans. Image Process.*, vol. 16, no. 7, pp. 1873–1887, July 2007.
- [73] S. Geman and D. Geman, “Stochastic relaxation, Gibbs distribution, and the Bayesian restoration of images,” *IEEE Trans. Pattern Anal. Mach. Intell.*, vol. 6, no. 6, pp. 721–741, 1984.
- [74] G. Gilboa and S. Osher, “Nonlocal linear image regularization and supervised segmentation,” *SIAM Mul. Model. and Simul.*, vol. 6, pp. 595–630, 2007.
- [75] G. Giraldi, E. Strauss, and A. Oliveira, “A boundary extraction method based on dual-T-snakes and dynamic programming,” in *IEEE Int. Conf. Comput. Vis. Pattern Recognit.*, Hilton Head Island, SC, USA, 2000, pp. 44–49.

- [76] A. Goldenshluger and A. Nemirovski, "Adaptive de-noising of signals satisfying differential inequalities," *IEEE Trans. Inf. Theory*, vol. 43, no. 3, pp. 873–889, 1997.
- [77] L. Gong, S. Pathak, D. Haynor, P. Cho, and Y. Kim, "Parametric shape modeling using deformable superellipses for prostate segmentation," *IEEE Trans. Med. Imag.*, vol. 23, no. 3, pp. 340–349, 2004.
- [78] R. Gonzalez and R. Woods, *Digital image processing*, 3rd ed. Prentice Hall, 2008.
- [79] G. H. Granlund and H. Knutsson, *Signal processing for computer vision*. Kluwer Academic Publisher, 1995.
- [80] J. F. Haddon and J. F. Boyce, "Image segmentation by unifying region and boundary information," *IEEE Trans. Pattern Anal. Mach. Intell.*, vol. 12, no. 10, pp. 929–948, Oct. 1990.
- [81] F. Hampel, "The influence curve and its role in robust estimation," *J. American Statistical Association*, vol. 62, pp. 1179–1186, 1974.
- [82] X. Hao, C. Bruce, C. Pislaru, and J. Greenleaf, "Segmenting high-frequency intracardiac ultrasound images of myocardium into infarcted, ischemic and normal regions," *IEEE Trans. Med. Imag.*, vol. 20, pp. 1373–1383, 2001.
- [83] R. M. Haralick, "Digital step edges from zero-crossings of second directional derivative," *IEEE Trans. Pattern Anal. Mach. Intell.*, vol. 6, no. 1, pp. 58–68, 1984.
- [84] K. Haris, S. N. Efstratiadis, N. Maglaveras, and A. K. Katsaggelos, "Hybrid image segmentation using watersheds and fast region merging," *IEEE Trans. Image Process.*, vol. 7, pp. 1684–1699, 1998.
- [85] J. A. Hartigan and M. A. Wong, "Algorithm AS 136 : A k -means clustering algorithm," *J. the Royal Statistical Society, Series C (Applied Statistics)*, pp. 100–108, 1979.
- [86] K. He, J. Sun, and X. Tang, "Guided image filtering," in *European Conf. Comput. Vis.*, 2010, pp. 1–14.
- [87] A. Hill and C. Taylor, "Model-based image interpretation using genetic algorithms," *Image Vis. Comput.*, vol. 10, no. 5, pp. 295–300, 1992.

- [88] S. Horowitz and T. Pavlidis, "Picture segmentation by a tree traversal algorithm," *J. the Association for Comput. Machinery*, vol. 23, no. 2, pp. 368–388, 1976.
- [89] G. Jacob, J. Noble, C. Behrenbruch, A. Kelion, and A. Banning, "A shape-space-based approach to tracking myocardial borders and quantifying regional left-ventricular function applied in echocardiography," *IEEE Trans. Med. Imag.*, vol. 21, no. 3, pp. 226–238, 2002.
- [90] E. Jakeman and R. Tough, "Generalized K -distribution : A statistical model for weak scattering," *J. Optical Society of America*, vol. 4, pp. 1764–1772, 1987.
- [91] A. C. Jalba, M. H. F. Wilkinson, and J. B. T. M. Roerdink, "CPM : A deformable model for shape recovery and segmentation based on charged particles," *IEEE Trans. Pattern Anal. Mach. Intell.*, vol. 26, no. 10, pp. 1–16, 2004.
- [92] S. Jehan-Besson, M. Barlaud, and G. Aubert, "DREAM2S : deformable regions driven by an Eulerian accurate minimization method," *Int. J. Comput. Vis.*, vol. 53, no. 1, pp. 45–70, 2003.
- [93] J. A. Jensen, "Field : A program for simulating ultrasound systems," in *10th Nordic-Baltic Conf. on Biomed. Imag.*, vol. 34, 1996, pp. 351–353.
- [94] J. A. Jensen and N. B. Svendsen, "Calculation of pressure fields from arbitrarily shaped, apodized, and excited ultrasound transducers," *IEEE Trans. Ultra. Fer. Freq. Control*, vol. 39, pp. 262–267, 1992.
- [95] M. Jung, G. Peyré, and L. D. Cohen, "Nonlocal active contours," *SIAM J. Imag. Sciences*, vol. 5, no. 3, pp. 1022–1054, 2012.
- [96] M. Kass, A. Witkin, and D. Terzopoulos, "Snakes : Active contour models," *Int. J. Comput. Vis.*, vol. 1, no. 4, pp. 321–331, 1988.
- [97] V. Katkovnik, "A new method for varying adaptive bandwidth selection," *IEEE Trans. Singal Process.*, vol. 47, no. 9, pp. 2567–2571, 1999.
- [98] V. Katkovnik, K. Egiazarian, and J. Astola, "Adaptive window size image de-noising based on intersection of confidence intervals (ICI) rule," *J. Math. Imag. Vis.*, vol. 16, no. 3, pp. 223–235, 2002.

- [99] ———, *Local approximation techniques in signal and image processing*. Washington : Int. Society for Optical Eng., 2006.
- [100] V. Katkovnik, A. Foi, K. Egiazarian, and J. Astola, “From local kernel to nonlocal multiple-model image denoising,” *Int. J. Comput. Vis.*, vol. 86, pp. 1–32, 2010.
- [101] C. Kervrann and J. Boulanger, “Optimal spatial adaptation for patch-based image denoising,” *IEEE Trans. Image Process.*, vol. 15, no. 10, pp. 2866–2878, 2006.
- [102] J. Kim, J. Fisher, A. Yezzi, M. Çetin, and A. Willsky, “A nonparametric statistical method for image segmentation using information theory and curve evolution,” *IEEE Trans. Image Process.*, vol. 14, pp. 1486–1502, 2005.
- [103] B. Kimia, A. Tannenbaum, and S. Zucker, “Shapes, shocks, and deformations I : The components of two-dimensional shape and the reaction-diffusion space,” *Int. J. Comput. Vis.*, vol. 15, no. 3, pp. 189–224, 1995.
- [104] R. Kimmel, A. Amir, and A. Bruckstein, “Finding shortest paths on surfaces using level sets propagation,” *IEEE Trans. Pattern Anal. Mach. Intell.*, vol. 17, no. 6, pp. 635–640, 1995.
- [105] R. Kimmel, *Geometric Level Set Methods in Imaging, Vision, and Graphics*. New York : Springer, 2003, ch. Fast edge integration, pp. 59–77.
- [106] S. Kindermann, S. Osher, and P. W. Jones, “Deblurring and denoising of images by nonlocal functionals,” *Multiscale Modeling & Simulation*, vol. 4, no. 4, pp. 1091–1115, 2005.
- [107] S. Konishi, A. L. Yuille, J. M. Coughlan, and S. C. Zhu, “Statistical edge detection : Learning and evaluating edge cues,” *IEEE Trans. Pattern Anal. Mach. Intell.*, vol. 25, pp. 57–74, 2003.
- [108] P. Kovesi, “Image features from phase congruency,” *Videre : J. Computer Vis. Research*, vol. 1, no. 3, pp. 1–26, 1999.
- [109] S. Lankton and A. Tannenbaum, “Localizing region-based active contours,” *IEEE Trans. Image Process.*, vol. 17, no. 11, pp. 2029–2039, 2008.
- [110] M. Lebrun, M. Colom, A. Buades, and J. Morel, “Secrets of image denoising cuisine,” *Acta Numerica*, vol. 21, pp. 475–576, 2012.

- [111] F. Lecellier, J. Fadili, S. Jehan-Besson, G. Aubert, M. Revenu, and E. Saloux, “Region-based active contours with exponential family observations,” *J. Math. Imag. Vis.*, vol. 36, no. 1, pp. 28–45, 2010.
- [112] F. Lecellier, “Les contours actifs basés région avec a priori de bruit, de texture et de forme : Application à l’échocardiographie,” Ph.D. dissertation, Université de Caen, 2009.
- [113] F. Lecellier, S. Jehan-Besson, J. Fadili, G. Aubert, and M. Revenu, “Optimization of divergences within the exponential family for image segmentation,” in *Lect. Note Comput. Sci*, vol. 5567. Berlin-Heidelberg : Springer, 2009, pp. 137–149.
- [114] S. Leung and S. Oshery, “An alternating direction explicit (ADE) scheme for time-dependent evolution equations,” UCLA, Tech. Rep., 2005.
- [115] M. Leventon, W. Grimson, and O. Faugeras, “Statistical shape influence in geodesic active contours,” in *IEEE Int. Conf. Comput. Vis. Pattern Recognit.*, South Carolina, United States, 2000, pp. 1316–1323.
- [116] M. Lew, “Content-based multimedia information retrieval : State of the art and challenges,” *ACM Trans. Multimedia Comput. Commun. Appl*, vol. 2, pp. 1–19, 2006.
- [117] B. Li and S. Acton, “Active contour external force using vector field convolution for image segmentation,” *IEEE Trans. Image Process.*, vol. 16, no. 8, pp. 2096–2106, Aug. 2007.
- [118] C. Li, C. Xu, C. Gui, and M. D. Fox, “Distance regularized level set evolution and its application to image segmentation,” *IEEE Trans. Image Process.*, vol. 19, no. 12, pp. 3243–3254, 2010.
- [119] C. Li, R. Huang, Z. Ding, J. C. Gatenby, and D. N. Metaxas, “A level set method for image segmentation in the presence of intensity inhomogeneities with application to MRI,” *IEEE Trans. Image Process.*, vol. 20, no. 7, pp. 2007–2016, 2011.
- [120] C. Li, C.-Y. Kao, J. C. Gore, and Z. Ding, “Minimization of region-scalable fitting energy for image segmentation,” *IEEE Trans. Image Process.*, vol. 17, no. 10, pp. 1940–1949, 2008.

- [121] C. Li, C. Xu, C. Gui, and M. D. Fox, "Level set evolution without re-initialization : A new variational formulation," *IEEE Int. Conf. Comput. Vis. Pattern Recognit.*, vol. 1, pp. 430–436, 2005.
- [122] S. Z. Li, *Markov random field modeling in computer vision*. London : Springer-Verlag, 1995.
- [123] N. Lin, W. Yu, and J. Duncan, "Combinative multi-scale level set framework for echocardiographic image segmentation," *Med. Image Anal.*, vol. 7, pp. 529–537, 2003.
- [124] T. Lindeberg, *Scale-Space Theory in Computer Vision*. Springer, 1994.
- [125] ———, "Feature detection with automatic scale selection," *Int. J. Comput. Vis.*, vol. 30, no. 2, pp. 79–116, 1998.
- [126] J. B. MacQueen, "Some methods for classification and analysis of multivariate observations," *Proceedings of 5th Berkeley Symposium on Mathematical Statistics and Probability*, pp. 281–297, 1967.
- [127] R. Malladi, J. Sethian, and B. Vemuri, "Shape modeling with front propagation : A level set approach," *IEEE Trans. Pattern Anal. Mach. Intell.*, vol. 17, pp. 158–175, 1995.
- [128] D. Maltoni, D. Maio, A. Jain, and S. Prabhakar, *Handbook of fingerprint recognition*, 2nd ed. Springer, 2009.
- [129] D. Marr and E. Hildreth, "Theory of edge detection," *Proceedings of Royal Society of London.*, vol. B 207, pp. 187–217, 1980.
- [130] G. Mastin, "Adaptive filters for digital image noise smoothing : An evaluation," *Vis., Graph. and Image Process.*, vol. 31, no. 1, pp. 103–121, 1985.
- [131] T. McInerney and D. Terzopoulos, "Topologically adaptable snakes," in *IEEE Int. Conf. Comput. Vis.*, Cambridge, MA, USA, 1995, pp. 840–845.
- [132] P. Meer, J. Jolion, , and A. Rosenfeld, "A fast parallel algorithm for blind estimation of noise variance," *IEEE Trans. Pattern Anal. Mach. Intell.*, vol. 12, no. 2, pp. 216–223, 1990.

- [133] O. Michailovich, Y. Rathi, and A. Tannenbaum, "Image segmentation using active contours driven by the Bhattacharyya gradient flow," *IEEE Trans. Image Process.*, vol. 16, no. 11, pp. 2787–2801, 2007.
- [134] I. Mikié, S. Krucunski, and J. Thomas, "Segmentation and tracking in echocardiographic sequences : active contours guided by optical flow estimates," *IEEE Trans. Med. Imag.*, vol. 17, pp. 272–284, 1998.
- [135] S. C. Mitchell, J. G. Bosch, B. P. F. Lelieveldt, R. J. van der Geest, J. H. C. Reiber, and M. Sonka, "3-D active appearance models : segmentation of cardiac MR and ultrasound images," *IEEE Trans. Med. Imag.*, vol. 21, no. 9, pp. 1167–1178, 2002.
- [136] J. Morel and S. Solimini, *Variational Methods for Image Segmentation*. Boston, MA : Birkhauser, 1994.
- [137] M. C. Morrone and R. A. Owens, "Feature detection from local energy," *Pattern Recognit. Lett.*, vol. 6, no. 5, pp. 303–313, 1987.
- [138] M. Mulet-Parada and J. Noble, "2D+T acoustic boundary detection in echocardiography," *Med. Image Anal.*, vol. 4, no. 1, pp. 21–30, 2000.
- [139] D. Mumford and J. Shan, "Optimal approximations by piecewise smooth functions and associated variational problems," *Communications on Pure and Applied Mathematics*, vol. 42, pp. 577–685, 1989.
- [140] R. Muzzolini, Y. Yang, and R. Person, "A multiresolution texture segmentation approach with application to diagnostic ultrasound images," *IEEE Trans. Med. Imag.*, vol. 12, pp. 108–123, 1993.
- [141] S. Nadarajah, "Statistical distributions of potential interest in ultrasound speckle analysis," *Phys. Med. Biol.*, vol. 52, pp. 213–227, 2007.
- [142] M. Nielsen, L. Florack, and R. Deriche, "Regularization, scale-space, and edge detection filters," *J. Math. Imag. Vis.*, vol. 7, pp. 291–308, 1997.
- [143] W. Niessen, B. Romeny, and M. Viergever, "Geodesic deformable models for medical image analysis," *IEEE Trans. Med. Imag.*, vol. 17, no. 4, pp. 634–641, 1998.

- [144] M. Nillesen, R. Lopata, I. Gerrits, L. Kapusta, J. Thijssen, and C. de Korte, "Modeling envelope statistics of blood and myocardium for segmentation of echocardiographic images," *Ultrasound Med. Biol.*, vol. 34, no. 4, pp. 674–680, 2008.
- [145] A. Noble, "Ultrasound image segmentation and tissue characterization," *Proceedings of the Institution of Mechanical Engineers*, vol. 224, no. 2, pp. 307–316, 2010.
- [146] A. Noble and D. Boukerroui, "Ultrasound image segmentation : A survey," *IEEE Trans. Med. Imag.*, vol. 25, no. 8, pp. 987–1010, 2006.
- [147] R. Ohlander, K. Price, and D. R. Reddy, "Picture segmentation using a recursive region splitting method," *Computer Graph. and Image Process.*, vol. 8, no. 3, pp. 313–333, 1978.
- [148] S. Olsen, "Estimation of noise in images : An evaluation," *GVGIP : Graphical Models and Image Process.*, vol. 55, no. 4, pp. 319–323, 1993.
- [149] C. F. Olson, "Adaptive-scale filtering and feature detection using range data," *IEEE Trans. Pattern Anal. Mach. Intell.*, vol. 22, no. 9, pp. 983–991, 2000.
- [150] S. Osher and N. Paragolis, *Geometric Level Set Methods in Imaging Vision and Graphics*. Springer Verlag, 2003.
- [151] S. Osher and J. A. Sethian, "Fronts propagating with curvature-dependent speed : Algorithms based on Hamilton-Jacobi formulations," *J. Comput. Phys.*, vol. 79, no. 1, pp. 12–49, 1988.
- [152] S. J. Osher and R. P. Fedkiw, *Level Set Methods and Dynamic Implicit Surfaces*, 1st ed. Springer, Oct. 2002.
- [153] N. Pal and S. Pal, "A review on image segmentation techniques," *Pattern Recognit.*, vol. 26, no. 9, pp. 1277–1294, 1993.
- [154] M. Papadogiorgaki, V. Mezaris, Y. S. Chatzizisis, G. D. Giannoglou, and I. Kompatsiaris, "Image analysis techniques for automated ivus contour," *Ultrasound Med. Biol.*, vol. 34, no. 9, pp. 1482–1498, 2008.
- [155] G. Papari and N. Petkov, "Edge and line oriented contour detection : State of the art," *Image Vis. Comput.*, vol. 29, no. 2-3, pp. 79–103, 2011.

- [156] N. Paragios and R. Deriche, "Geodesic active regions and level set methods for supervised texture segmentation," *Int. J. Comput. Vis.*, vol. 46, no. 3, pp. 223–247, 2002.
- [157] —, "A PDE-based level-set approach for detection and tracking of moving objects," in *IEEE Int. Conf. Comput. Vis.*, 1998, pp. 1139–1145.
- [158] N. Paragios, O. Mellina-gottardo, and V. Ramesh, "Gradient vector flow fast geometric active contours," *IEEE Trans. Pattern Anal. Mach. Intell.*, vol. 26, pp. 402–407, 2004.
- [159] S. Pathak, V. Chalana, D. Haynor, and Y. Kim, "Edge-guided boundary delineation in prostate ultrasound images," *IEEE Trans. Med. Imag.*, vol. 19, no. 12, pp. 1211–1219, 2000.
- [160] T. Pavlidis and Y. T. Liow, "Integrating region growing and edge detection," *IEEE Trans. Pattern Anal. Mach. Intell.*, vol. 12, no. 3, pp. 225–233, 1990.
- [161] P. Perona and J. Malik, "Scale-space and edge detection using anisotropic diffusion," *IEEE Trans. Pattern Anal. Mach. Intell.*, vol. 12, pp. 629–639, 1990.
- [162] D. Pham, C. Xu, and J. Prince, "Current methods in medical image segmentation," *Annu. Rev. Biomed. Eng.*, pp. 315–337, 2000.
- [163] J. Piovano and T. Papadopoulo, "Local statistic based region segmentation with automatic scale selection," in *European Conf. Comput. Vis.*, Marseille, France, 2008, pp. 486–499.
- [164] J. Piovano, M. Rousson, and T. Papadopoulo, *Handbook of Medical Imaging*. Berlin : Springer, 2007, vol. 4485, LNCS, ch. Scale space and variational methods in computer vision, pp. 709–720.
- [165] T. Pock, D. Cremers, H. Bischof, and A. Chambolle, "An algorithm for minimizing the Mumford-Shah functional," in *IEEE Int. Conf. Comput. Vis.*, 2009, pp. 1133–1140.
- [166] R. Prager, A. Gee, G. Treece, and L. Berman, "Decompression and speckle detection for ultrasound images using the homodyned K -distribution," *Pattern Recognit. Lett.*, vol. 24, no. 4-5, pp. 705–713, 2003.

- [167] M. Protter, M. Elad, H. Takeda, and P. Milanfar, "Generalizing the non-local-means to super-resolution reconstruction," *IEEE Trans. Image Process.*, vol. 18, no. 1, pp. 36–51, 2009.
- [168] R. Ronfard, "Region-based strategies for active contour models," *Int. J. Comput. Vis.*, vol. 13, no. 2, pp. 229–251, 1994.
- [169] M. Rousson and N. Paragios, "Shape priors for level set representations," in *European Conf. Comput. Vis.* London, UK : Springer-Verlag, 2002, pp. 78–92.
- [170] M. Rousson, T. Brox, and R. Deriche, "Active unsupervised texture segmentation on a diffusion based feature space," INRIA, Tech. Rep. 4695, Jan. 2003.
- [171] M. Rousson and D. Cremers, "Efficient kernel density estimation of shape and intensity priors for level set segmentation," in *MICCAI*, 2005, pp. 757–764.
- [172] M. Rousson and R. Deriche, "A variational framework for active and adaptive segmentation of vector valued images," INRIA, Tech. Rep. 4515, Jul. 2002.
- [173] M. Rousson and N. Paragios, "Prior knowledge, level set representations & visual grouping," *Int. J. Comput. Vis.*, vol. 76, no. 3, pp. 1573–1405, 2007.
- [174] G. Sapiro and A. Tannenbaum, "Affine invariant scale-space," *Int. J. Comput. Vis.*, vol. 11, no. 1, pp. 25–44, 1993.
- [175] A. Sarti, C. Corsi, E. Mazzini, and C. Lamberti, "Maximum likelihood segmentation of ultrasound images with Rayleigh distribution," *IEEE Trans. Ultra. Fer. Freq. Control*, vol. 52, no. 6, pp. 947–960, 2005.
- [176] A. Sarti, K. Mikula, and F. Sgallari, "Nonlinear multiscale analysis of 3D echocardiographic sequences," *IEEE Trans. Med. Imag.*, vol. 18, no. 6, pp. 453–466, 1999.
- [177] J. Sethian, *Level Set Methods and Fast Marching Methods : Evolving Interfaces in Computational Geometry, Fluid Mechanics, Computer Vision, and Materials Science*, 2nd ed. Berkeley : Cambridge University Press, 1999.
- [178] J. Sethian and J. Strain, "Crystal growth and dendritic solidification," *J. Comput. Phys.*, vol. 98, pp. 231–253, 1992.

- [179] P. M. Shankar, "A general statistical model for ultrasonic backscattering from tissues," *IEEE Trans. Ultra. Fer. Freq. Control*, vol. 47, no. 3, pp. 727–736, 2000.
- [180] P. Shankar, J. Reid, H. Ortega, C. Piccoli, and B. Goldberg, "Use of non-Rayleigh statistics for the identification of tumors in ultrasonic B-scans of the breast," *IEEE Trans. Med. Imag.*, vol. 12, no. 4, pp. 687–692, 1993.
- [181] F. Shao, K. Ling, W. Ng, and R. Wu, "Prostate boundary detection from ultrasonographic images," *J. Ultrasound Med.*, vol. 20, no. 6, pp. 605–623, 2003.
- [182] Y. Shi and W. Karl, "A real-time algorithm for the approximation of level-set-based curve evolution," *IEEE Trans. Image Process.*, vol. 17, no. 5, pp. 645–656, 2008.
- [183] B. W. Silverman, *Density Estimation for Statistics and Data Analysis*. Chapman & Hall, 1986.
- [184] B. Song and T. Chan, "A fast algorithm for level set based optimization," *CAM-UCLA*, vol. 68, pp. 02–68, 2002.
- [185] M. Sonka, V. Hlavac, and R. Boyle, *Image Processing, Analysis, and Machine Vision*, 2nd ed. Chapman & Hall, 1998.
- [186] C. Stein, "Estimation of the mean of a multivariate normal distribution," *Annals of statistics*, vol. 9, no. 6, pp. 1135–1151, 1981.
- [187] R. Szeliski, *Computer Vision : Algorithms and Applications*. Springer, 2010.
- [188] Z. Tao, H. Tagare, and J. Beaty, "Evaluation of four probability distribution models for speckle in clinical cardiac ultrasound images," *IEEE Trans. Med. Imag.*, vol. 25, no. 11, pp. 1483–1491, 2006.
- [189] D. Terzopoulos, A. Witkin, and M. Kass, "Constraints on deformable models : recovering 3D shape and nongrid motion," *Artif. Intell.*, vol. 36, no. 1, pp. 91–123, 1988.
- [190] C. Tomasi and R. Manduchi, "Bilateral filtering for gray and color images," in *IEEE Int. Conf. Comput. Vis.*, 1998, pp. 839–846.

- [191] A. Tsai, A. Yezzi, W. Wells, C. Tempany, D. Tucker, A. Fan, W. E. Grimson, and A. Willsky, "A shape-based approach to the segmentation of medical imagery using level sets," *IEEE Trans. Med. Imag.*, vol. 22, no. 2, pp. 137–154, 2003.
- [192] A. Tsai, A. Yezzi, and A. Willsky, "Curve evolution implementation of the Mumford-Shah functional for image segmentation, denoising, interpolation, and magnification," *IEEE Trans. Image Process.*, vol. 10, pp. 1169–1186, 2001.
- [193] L. Vese and T. Chan, "A multiphase level set framework for image segmentation using the Mumford-Shah functional," *Int. J. Comput. Vis.*, vol. 50, no. 3, pp. 271–293, 2002.
- [194] M. Vogt, J. Opretzka, C. Perrey, and H. Ermert, "Ultrasonic microscanning," *Proceedings of the Institution of Mechanical Engineers*, vol. 224, no. 2, pp. 225–240, 2010.
- [195] R. F. Wagner, S. W. Smith, J. M. Sandrik, and H. Lopez, "Statistics of speckle in ultrasound B-scans," *IEEE Trans. Sonics and Ultra.*, vol. 30, no. 3, pp. 156–163, May 1983.
- [196] L. Wang, L. He, A. Mishra, and C. Li, "Active contours driven by local Gaussian distribution fitting energy," *Singal Process.*, vol. 89, pp. 2435–2447, 2009.
- [197] L. Wang, C. Li, Q. Sun, D. Xia, and C.-Y. Kao, "Active contours driven by local and global intensity fitting energy with application to brain MR image segmentation," *Comput. Med. Imag. Graph.*, vol. 33, no. 7, pp. 520–531, 2009.
- [198] J. Weickert, *Anisotropic Diffusion in Image Processing*. B.G. Teubner Stuttgart, 1998.
- [199] J. Weickert, B. Romeny, and M. Viergever, "Efficient and reliable schemes for nonlinear diffusion filtering," *IEEE Trans. Image Process.*, vol. 7, pp. 398–410, 1998.
- [200] W. Wells, E. Grimson, R. Kikinis, and F. A. Jolesz, "Adaptive segmentation of MRI data," *IEEE Trans. Med. Imag.*, vol. 15, no. 4, pp. 429–442, 1996.
- [201] L. Wietzke, O. Fleischmann, and G. Sommer, "2D image analysis by generalized Hilbert transforms," in *Conformal Space, in ECCV, LNCS*. Springer-Verlag, 2008.

- [202] Wikipedia, “Exponential family — wikipedia, the free encyclopedia,” 2012, [Online; accessed 21-December-2012]. [Online]. Available : `\url{http://en.wikipedia.org/w/index.php?title=Exponential_family&oldid=528536153}`
- [203] D. Williams and M. Shah, “A fast algorithm for active contours and curvature estimation,” *CVGIP : Image Understanding*, vol. 55, no. 1, pp. 14–26, 1992.
- [204] A. Witkin, “Scale-space filtering a new approach to multi-scale description,” *IEEE Conf. on Acoustics, Speech, and Signal Process.*, vol. 9, pp. 150–153, 1984.
- [205] B. Wu and Y. Yang, “Local- and global-statistics-based active contour model for image segmentation,” *Mathematical Problems in Eng.*, 2012.
- [206] G. Xiao, J. M. Brady, A. J. Noble, and Y. Zhang, “Contrast enhancement and segmentation of ultrasound images—a statistical method,” *Proc. SPIE 3979, Med. Imag.*, pp. 1116–1125, 2000.
- [207] X. Xie and M. Mirmehdi, “Radial basis function based level set interpolation and evolution for deformable modelling,” *Image Vis. Comput.*, vol. 29, no. 2-3, pp. 167–177, 2011.
- [208] C. Xu and J. Prince, “Snakes, shapes, and gradient vector flow,” *IEEE Trans. Image Process.*, vol. 7, no. 3, pp. 359–369, 1998.
- [209] Q. Yang and D. Boukerroui, “Optimal spatial adaptation for local region-based active contours : An intersection of confidence intervals approach,” in *VISIGRAPP*, Algarve, Portugal, Mar. 2011, pp. 87–93.
- [210] ———, “Ultrasound image segmentation using local statistics with an adaptive scale selection,” in *IEEE Int. Symp. Biomed. Imag.*, Barcelona, Spain, May 2012, pp. 1096–1099.
- [211] R. Yang, M. Mirmehdi, and X. Xie, “A charged active contour based on electrostatics,” in *Advanced Concepts for Intelligent Vision Systems*. Springer-Verlag LNCS 4179, Sep. 2006, pp. 173–184.
- [212] A. Yezzi, S. Kichenassamy, A. Kumar, P. Olver, and A. Tannenbaum, “A geometric snake model for segmentation of medical imagery,” *IEEE Trans. Med. Imag.*, vol. 16, no. 2, pp. 199–209, 1997.

- [213] A. Yezzi, A. Tsai, and A. Willsky, "A fully global approach to image segmentation via coupled curve evolution equations," *J. Visual Communication Image Representation*, vol. 13, no. 1-2, pp. 195–216, 2002.
- [214] R. Yildizoglu, J.-F. Aujol, and N. Papadakis, "Active contours without level sets," in *IEEE Int. Conf. Image Proc.*, Orlando, Florida, USA, Sep. 2012, p. 4.
- [215] J. Yu, J. Tan, and Y. Wang, "Ultrasound speckle reduction by a SUSAN-controlled anisotropic diffusion method," *Pattern Recognit.*, vol. 43, no. 9, pp. 3083–3092, 2010.
- [216] Y. Yu, C. Zhang, Y. Wei, and X. Li, "Active contour method combining local fitting energy and global fitting energy dynamically," *Medical Biometrics : Lecture Notes in Computer Science*, vol. 6165, pp. 163–172, 2010.
- [217] Y. Yu and S. T. Acton, "Speckle reducing anisotropic diffusion," *IEEE Trans. Med. Imag.*, vol. 11, no. 11, pp. 1260–1270, 2002.
- [218] ———, "Edge detection in ultrasound imagery using the instantaneous coefficient of variation," *IEEE Trans. Med. Imag.*, vol. 13, pp. 1640–1655, 2004.
- [219] D. Zhang and G. Lu, "Segmentation of moving objects in image sequence : A review," in *Circuits, Systems and Signal Process*, 2001, pp. 143–183.
- [220] H. Zhao, T. Chan, B. Merriman, and S. Osher, "A variational level set approach to multiphase motion," *J. Comput. Phys.*, vol. 127, pp. 197–195, 1996.
- [221] W. Zhao, R. Chellappa, P. Phillips, and A. Rosenfeld, "Face recognition : A literature survey," *ACM Computing Surveys*, pp. 399–458, 2003.
- [222] S. Zhu and A. Yuille, "Region competition : Unifying snakes, region growing, and Bayes/MDL for multiband image segmentation," *IEEE Trans. Pattern Anal. Mach. Intell.*, vol. 18, no. 9, pp. 884–900, 1996.
- [223] Y. Zhu, X. Papademetris, A. J. Sinusas, and J. S. Duncan, "A coupled deformable model for tracking myocardial borders from real-time echocardiography using an incompressibility constraint," *Med. Image Anal.*, vol. 14, no. 3, 2010.
- [224] D. Ziou and S. Tabbone, "Edge detection techniques : An overview," *Pattern Recognition and Image Analysis*, vol. 8, pp. 537–559, 1998.

- [225] X. Zong, A. Laine, and E. Geiser, "Speckle reduction and contrast enhancement of echocardiograms via multiscale nonlinear processing," *IEEE Trans. Med. Imag.*, vol. 17, no. 4, pp. 532–540, 1998.